Visualization of nanostructure distribution in Al alloy multilayers by small-angle X-ray scattering tomography

Lin Shan

2022

Contents

1. Introduction

1.1. Background

Composites which are comprise of similar/dissimilar materials are used in a variety of fields e.g., using carbon fiber reinforced (or glass fiber, for compensation) resin for reducing the weight of a vehicle; and controlling corrosion and weight in aerospace engineering. For this reason, the properties of the composite and also the consisting materials are studied by many researchers globally. Composites can be categorized by the different forms of material dispersing in the matrix material: Particle dispersed composite material, fiber reinforced composite material and laminated composite materials. In other perspectives, the dispersed material in these forms bond with the matrix with 3–1 dimension.

A metallic alloy itself can be regarded as a composite, since it is composed by different element atoms. This leads to the great potential in the features of a material e.g., mechanical property by designing the arrangement of the atoms. This is identical to controlling all four strengthening mechanisms of a metallic materials: the solid solution strengthening by solute atoms, precipitation strengthening by precipitates (Gerold & Haberkorn, 1966; Foreman, 1967), work hardening by dislocations (Ashby, 1966), and the grain refinement strengthening in a polycrystalline material (Hall, 1951; Petch, 1953). Therefore, for a similar/dissimilar composite made up of metallic alloys—especially for those precipitation hardening alloys—the designation of nanostructural distribution depends on the usage of the composite is significant for both the whole composite and the composing single materials. In order to conduct a full understanding of the nanostructural distribution in the metallic materials, various methods have been developed for observation directly and indirectly: e.g., transmission electron microscopy (TEM) (Miyazaki *et al.,* 1996, 2012), scanning electron microscopy (SEM), and SEM with attachments, i.e., energy dispersive X-ray spectroscopy (EDX) (Liu, 2018) local hardness, and electronic resistance are used in studies (Kim & Hong, 2015).

In this research, we used series of Al–Zn alloys, Al–Mg alloys, and Al–Zn–Mg alloys as composite. Where Al–Zn and Al–Zn–Mg alloy are three-layered composites, and they were two-dimensional laminated composite, or three-layered composite in particular. It is easy to control the solute atoms in the multilayered composite, since the bonding freedom is only one dimension, i.e., one direction, compared to two or three directions for other two types of composites.

In order to conduct a quantitative investigation on the composite of Al–Zn alloys and

Al–Zn–Mg alloys, the small angle X-ray scattering (SAXS) method has been used in this study. SAXS method has been applied with microbeam pencil X-ray as a probe to investigate the nanostructures on a composite locally, with changing the illuminating area. The nanostructural distribution was acquired as a mean value by either the specimen thickness (1D scanning), or the size of a voxel (SAXS applied computed tomography, SAXS-CT) measurement in this study.

  The Al–Mg alloy was a single layered material, since it cannot be detected by the ordinary SAXS measurement. Instead, an anomalous small angle X-ray scattering (ASAXS) method was conducted to investigate the nanostructure.

1.2. Objective alloys

1.2.1. Al–Zn alloys

Al–Zn alloys (Gerold & Merz, 1967; Hennion *et al.,* 1982; Guinier, 1996) are focused the attentions by many researchers for its high solubility of Zn atom in Al matrix, namely 66.5 mol% at eutectic temperature of 655 K (see Werner & Löffler, 1983), which enables to have an efficient investigation about both the kinetics and mechanisms of phase transformation.

The precipitations in Al–Zn starts from the Guinier–Preston zone (G. P. zone) (Guinier, 1938; Preston, 1938) facet to the Al matrix, in the shape of sphere (Merz & Gerold, 1966; Gerold & Merz, 1967; Ramlau & Löffler, 1981; Hennion *et al.,* 1982; Kostorz, 1983) and aligning along the $\langle 100 \rangle$ direction of the matrix (Kostorz, 1983). With G. P. zones coarsen with time, the shape changes into ellipsoid (Simerská & Syneček, 1967; Ramlau & Löffler, 1981; Deguercy *et al.,* 1982). The equatorial planes of the oblate spheroids are found to be formed on the $\{111\}$ plane of the matrix. When the Guinier radius exceeds 5 nm at a temperature between 293–363 K, these ellipsoidal G. P. zones would grow into α'_R (Löffler *et al.,* 1978). The discussion of α'_R phase is omitted in this study, as it is too large compared to the results in this treatise.

1.2.2. Al–Mg alloys

Al–Mg alloy is the main component of 5000 series in Al alloys, which is an alternative material for the automobile industry. It is known that the Mg atoms distribute as a modulated structure first, and when aged at a low temperature, precipitations occur and the precipitates with $L1_2$ structure are observed aligning along the $\langle 100 \rangle$ direction on matrix (Bernole *et al.,* 1973; Deguercy *et al.,* 1973; Sato & Takahashi, 1984). These precipitates are also facetted G. P. zones (Roth & Raynal, 1974, 1975). With aging proceeds, these G. P. zones are known to be transformed into β' phase, and then change into the stable β phase (Osamura & Ogura, 1984). The stable β phase are also noted as Al_3Mg_2 which composed by 38.5–40.3 mol%Mg (Riederer, 1936; Samson, 1965). Similar to the Al–Zn alloy, the G. P. zone is the only objective considered in this study, due to either the detectability, or the detected size. Al–Mg alloy cannot be detected with ordinary small-angle scattering X-ray (SAXS) method, due to the reason that Al locates the next to Mg in the periodic table, and also in the same period. This directly leads to the similarity in the atomic radius and the number of electrons for an atom, which leads to the similarity in electron density and the weakness in the lattice strain.

1.2.3. Al–Zn–Mg alloys

Al–Zn–Mg alloys are widely used for the property of high strength, and the good balancing of workability, weldability, and a receptible strength. Some of them are known as 7000 series of Al alloys (Itoh *et al.,* 1988), which doped with additional elements like Cu and Si. In Al-Zn-Mg alloys, the precipitations are believed to be take place depend on the Zn/Mg atomic ratio. Fig. 1.2.1 shows the equilibrium phase diagram of Al–Zn–Mg at the Al corner by Fink and Willey (1938). According to the atom probe tomography (APT) by Bigot *et al.* (1997), the precursor of T phase ($Mg_3Zn_3Al_2$) has a Zn/Mg of 0.7, and the precursor of η phase ($MgZn_2$) has a Zn/Mg of approximately 1–2 (Bigot *et al.,* 1996; Deschamps *et al.,* 2001; Sha & Cerezo, 2004).

Fig. 1.2.1 Miscibility gap at various temperatures (°C) at the Al corner of Al-Zn-Mg system by Fink and Willey (1938).
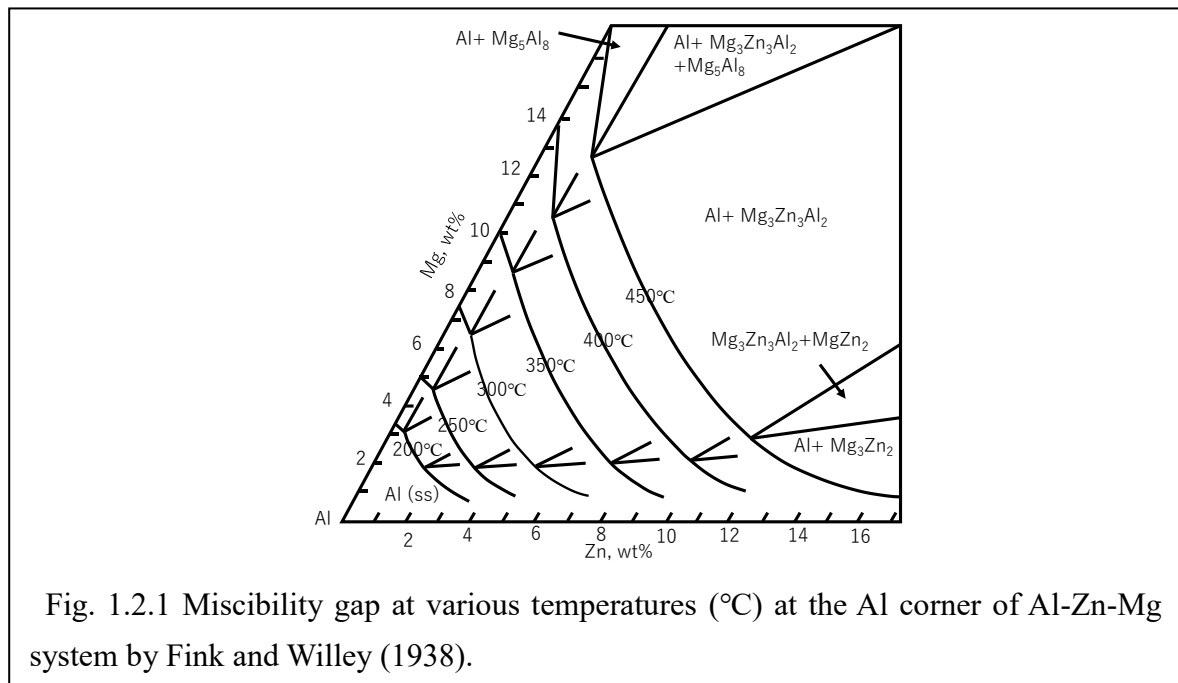
1.2.3.1. Stable phases in Al–Zn–Mg alloys

In the ternary Al–Zn–Mg system, the stable phase of η ($MgZn_2$) (Friauf, 1927) and T ($Mg_3Zn_3Al_2$) (Bergman *et al.,* 1957) is known for co-existing with the solid solution α phase. The transformations in this alloy is extremely complicated, and the transformations for these stable phases are still not clear in these days.

η phase is believed to be the final product with following process (Lorimer & Nicholson, 1966):

$$Solid\ solution\ (\alpha) \rightarrow G.P.zone\ (I,II)$$
$$\rightarrow plate\ shaped\ \eta'\ phase\ (metastable\ MgZn_2) \rightarrow \eta\ phase$$

4
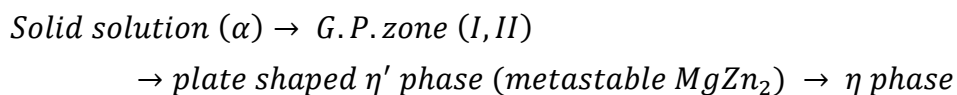
T phase, on the other hand, is the final stable phase from the transformation with this process (Lorimer, 1985):

$$Solid\ solution\ (\alpha) \rightarrow spherical\ G.P.Zone$$
$$\rightarrow plate\ shaped\ \eta'\ phase\ (metastable\ MgZn_2) \rightarrow \eta\ phase$$
$$\rightarrow T\ phase$$
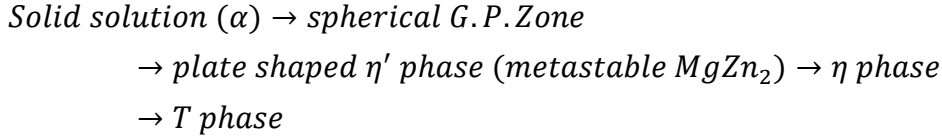
or the series below (Ma & Ouden 1999):

$$Solid\ solution\ (\alpha) \rightarrow G.P.zone \rightarrow T'\ phase\ (metastable\ Mg_3Zn_3Al_2)$$
$$\rightarrow T\ phase$$
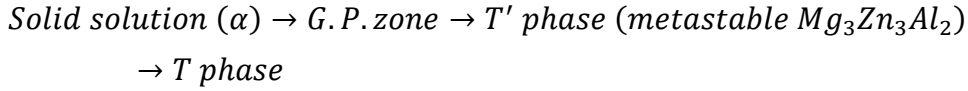
η (MgZn₂) phase is a stable phase in a hexagonal crystal structure with lattice parameters of a = 5.21 Å and c = 8.60 Å (Friauf, 1927). At least 11 different crystallographic orientations related to the matrix was reported (Embury & Nicholson, 1965; Thackery, 1968; Gjønnes & Simensen, 1970; Auger *et al.,* 1974; Ito *et al.,* 1988). There are reported three typical shapes and orientations in these η phases (Gjønnes & Simensen, 1970), which are summarized in Table 1.2.1.

Table 1.2.1 Typical orientation and shape of η phases

Type of η	Orientation relationship	Shape of precipitate
η_1	$(0001)_\eta\ //\ (110)_\alpha,$ $[10\bar{1}0]_\eta\ //\ [001]_\alpha$	Plate parallel to $\{100\}_\alpha$
η_2	$(0001)_\eta\ //\ (1\bar{1}\bar{1})_\alpha,$ $[10\bar{1}0]_\eta\ //\ [110]_\alpha$	Plates parallel to $\{111\}_\alpha$ in grain, hemisphere in grain boundary
η_3	$(0001)_\eta\ //\ (1\bar{1}\bar{1})_\alpha,$ $[\bar{1}2\bar{1}0]_\eta\ //\ [1\bar{1}\bar{1}]_\alpha$	Rods that $[0001]_\eta$ parallel to $\langle100\rangle_\alpha$

T phase (Mg₃Zn₃Al₂) is known as body-centered-cubic (BBC) structure with a lattice parameter a = 14.16 Å (Bergman *et al.,* 1957). Also, it is known that T phase is not a major objective attributing the strength of Al–Mg–Zn alloy.

1.2.3.2. Metastable phase in Al–Zn–Mg alloys

η′ phase is the metastable phase for η phase, and which is responsible for the high strength in 7000 series Al alloy (Park & Ardell, 1983; Lendvai, 1996). It is a hexagonal crystal with parameter a = 4.96 Å, c = 14.02 Å (Auld & Cousland, 1974; Li *et al.,* 1999). It is generally accepted that the η′ phase is a plate shaped precipitate stays on the plane $\{111\}_\alpha$ of matrix, and also be coherent with the matrix on this plane only. η′ phase is

observed in the alloys which have a Zn/Mg ratio of 0.7–2.5 (Brenner *et al.,* 1991; Warren *et al.,* 1992; Li *et al.,* 1999; Maloney *et al.,* 1999; Deschamps *et al.,* 2001)

There are 2 types of G. P. zones, i.e. G. P. zone (I) and G. P. zone (II); were found in the Al–Zn–Mg alloys. G. P. zone (I) is observed dominant when aged at room temperature, and G. P. zone (II) is believed as the precursor of η′ phase (Mukhopadhyay, 1994). TEM observation revealed that G. P. zone (I) is spherical (Mukhopadhyay, 1994; Stiller *et al.,* 1999; Berg *et al.,* 2001), and G. P. zone (II) can either be spherical (Mukhopadhyay, 1994; Stiller *et al.,* 1999) or plate shaped (Berg *et al.,* 2001, Mukhopadhyay & Prasad, 2011).

1.3. Treatise outline

This treatise contains 6 chapters.

Chapter 1 contains the background and short introductions about the features of alloy systems investigated as objective materials, and the reason of using small angle X-ray scattering (SAXS) method with tomographic technology, and the anomalous small-angle X-ray scattering method (ASAXS) in this treatise briefly.

Chapter 2 contains the methods, materials and the experimental set ups related to this treatise. In this chapter, the nature of the small angle X-ray scattering (SAXS) method was introduced with the application to the 1D scanning method and 2D tomographic technique. The nature of the computed tomography (CT) was conducted from multiple dimension into two-dimension, and a detailed explanation for the reconstruction method was explained, particularly for the discrete experimental condition.

Chapter 3 shows the results of 1D SAXS scanning measurements on the Al based binary and ternary three-layered composites: the Al/Al– 14.07mass%Zn/Al multilayer; and the Al–2.45 mass%Mg/Al–10.16 mass%Zn/Al–2.45 mass%Mg multilayer, after conducting series of heat treatments. The scanning SAXS measurement was conducted in vicinity of solute graded interdiffusion area for each composite. The nanostructural distribution was analyzed spatially with unit area of 5 and 10 μm. The local hardness distribution investigated with micro Vickers hardness tests were interpreted successfully by the estimated nanostructural distribution measured individually.

Chapter 4 shows the ASAXS used in Al–Mg alloy. Generally, Mg-rich precipitates are not observable using SAXS method, due to the low contrast in the electron density of Al and Mg atoms. However, by applying the SAXS method with an energy of the incident X-ray adjusted to the absorption edge of Mg, and by absorbing the X-ray only by Mg atom practically, the contrast in the scattered intensity originated from the Mg-rich structure and Mg-poor structure is able to be detected. In this chapter, the conventional parameters of 2D SAXS pattern, relative integrated intensity, and the Guinier radius in different nanostructure was shown.

Chapter 5 explains the absolute reconstruction method for computed tomography, with the applications on the three-layered composites investigated with 1D SAXS scanning method in chapter 3. Both of the tomography composed by the attenuation coefficient and scattered intensity was reconstructed with absolute value. No standard specimen was used for the reconstructions in the absolute attenuation coefficient tomographies. Tomographies composed by solute elements were estimated with EDX data. Also, for the

first time, the absolute SAXS intensity profiles originated from the three-layered metallic composites were successfully reconstructed to the cubes with 20 μm×20 μm×20 μm, using glassy carbon as standard specimen. The tomography of the mean size of the precipitates were estimated subsequently for both binary and ternary composites. The volume fraction tomography was assessed for the binary multilayer.

In chapter 6, important results in each chapter were summarized.

2. Methods

2.1. Theory of Small-Angle X-ray Scattering (SAXS)

Small-Angle X-ray Scattering (SAXS), along with Small-Angle Neutron Scattering (SANS) is a widely used method for metallic materials and non-metallic materials, for a quantitative analysis of a mean information about the electron/neutron density difference, the volume fraction, and the size of scatterers.

Guinier–Preston zone (G. P. zone) was found by A. Guinier (1938) and G. D. Preston (1938) individually in Al-Cu alloy from the phenomenon of hardening effect caused from the prolonging of time, or known as aging effect, which was found in the September of 1906 by Dr. A. Wilm (1911). In the old days, due to the nanometer sized G. P. zone was not convenient to be investigated: it was too small for either of the TEM and SEM; and was also too large for the conventional wide-angle X-ray measurement i.e. XRD. Therefore, SAXS method was used as a powerful tool for investigating nanostructures such as G. P. zone statistically at that time.

These days, with the development in TEM and SEM technology, it is not that difficult to have a detailed investigation on the nanostructure, but from the trade-off relation in the target size and the view size of direct observation, SAXS measurement are still useful for the statistical analysis. It derives the mean size of all electron/neutron density oscillation, like the long period stacking order (LPSO) structure found in the Mg alloys by Kawamura *et al.* (2001) and Abe *et al.* (2002), attracted the interests of many researchers. X-ray is an electromagnetic wave with a certain wavelength, or energy. Therefore, when X-ray meet any metallic and nonmetallic material, it interacts with the charged particles of their atoms, i.e. electrons and protons. In SAXS measurements, the X-ray have to be an incident beam originated from outside of the target material, and since the atomic core which consist of protons is neglectable from its large mass and also the shielding effect from surrounding electrons, the existence of protons is neglectable for analyzing SAXS result. Inelastic scattering is often neglected due to its low intensity in the SAXS measurement.

2.2. Scattered intensity in SAXS

Fig. 2.2.1 A schematic illustration of SAXS measurement
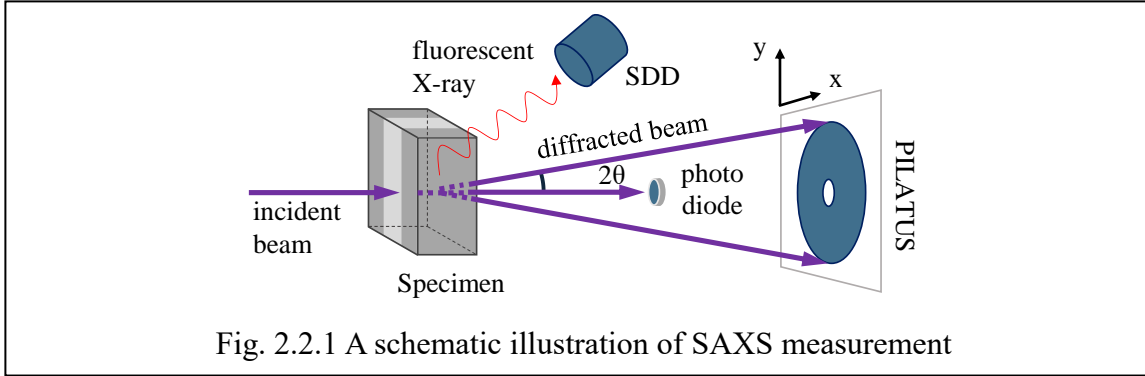
The absolute scattered intensity is often used in the SAXS method to describe the scattered intensity quantitatively. It is often either used with a unit of electron unit (e.u.), or differential cross-section ($cm^{-3} \cdot sr^{-1}$). The electron unit describes how much intensity scattered by an electron, regardless of the influences from the apparatus of experiment; which is easy to use but contains ambiguity. The differential cross-section is composed by SI units (International System of units), which links the intensity with the scattering length of electron, i.e. Thomas scattering length, which is also known as the classic radius of an electron.

Consider a unit cube of scatterers illuminated by an array of incident X-ray with a flux Φ_0, and the scattered intensity was measured for I_{sc} by a detector with an area of $\Delta\Omega$ in solid angle. Then the absolute intensity described by the differential scattered intensity $(d\sigma/d\Omega)$ would be:

$$\left(\frac{d\sigma}{d\Omega}\right) = \left(\frac{\Delta\sigma}{\Delta\Omega}\right) = \frac{I_{sc}}{\Phi_0 \Delta\Omega} = \frac{|E_{rad}|^2 R^2}{|E_{in}|^2}. \tag{2.1}$$

where σ is the absolute scattered intensity measured by the detector by a unit intensity of incident X-ray; E_{in} and E_{rad} is the strength of the incident and radiated electronic field; R is the distance of detector from scattered origin. As an electron is mainly the source of the scattered X-ray, eq. (2.1) would be expressed by the scattering length of an electron, i.e. the Thomson scattering length r_0:

$$\left(\frac{d\sigma}{d\Omega}\right) = \frac{|E_{rad}|^2 R^2}{|E_{in}|^2} = r_0{}^2 P$$

where

$$P = \begin{cases} 1 & synchrotron: vertical\ scattering\ plane \\ \cos^2\psi & synchrotron: horizontal scattering\ plane \\ 0.5(1+\cos^2\psi) & unpolerized\ source \end{cases} \tag{2.2}$$

10

where P is the polarization factor for scanning, ψ is the scattering angle, r_0 also is the classic radius of an electron.

The total cross-section σ_{total} is an alternative unit for the absolute scattered intensity also made up of SI units, which describes the intensity scattered at all solid angles. If integrating the solid angle into 4π with the consideration of the polarization factor P, the scattered intensity σ_{total} would be:

$$\sigma_{total} = \int_0^{4\pi} \left(\frac{d\sigma}{d\Omega}\right) d\Omega = 4\pi \cdot r_0{}^2 \int_0^{2\pi} d\theta \int_0^{\pi} Pd\psi = \frac{8}{3} r_0{}^2 \qquad (2.3)$$

2.2.1. Intraference and interference in SAXS

When a piece of material is illuminated by an array of incident X-ray, all scattered X-ray originated from the illuminated electrons sum up respectively causing superposition, which are detected as the oscillation in intensity. This intensity oscillation is caused by the phase discrepancy originated from the different distance of the respective illuminated electron to the detector, or identically, the distribution of the illuminated electrons.

The discussion on the interference by electrons density is analogous to which by the arrangement of the elementary matters composed by electrons, i.e. atoms and molecules. For a material which is a crystalline material like the most of the metallic materials, these elementary matters are repeated periodically in 3D; this enables us to reconsider the interference caused by electrons as the three-dimensional structure of this period, i.e. crystal lattices and unit cells.

Therefore, for a multiple phase material with multiple atomic arrangements, it is easier to consider the scattered X-ray emitted from each precipitated phase with a uniformed crystal lattice as the interference inside the precipitate, or the "intraference" of the precipitate. When the interference between different precipitates area observed, which implies the averaged distance of the precipitates are in an order of nanometer, and the observed SAXS profile is the superposition of the interference and intraference wave of precipitates.

2.2.1.1. Interference in X-ray and SAXS
2.2.1.1.1. The interference in X-ray

Interference is observed as a superposition of waves like X-ray. It happens when multiple sets of wave like u and v with a same period ω and amplitude A, encounter at a location with a different phase:

$$u = Ae^{-i\omega t}, v = Ae^{-i\omega t + d\varphi} \tag{2.4}$$

$$u + v = A\sum_{n=1}^{2} e^{-i\omega t_n} = Ae^{-i\omega t}(1 + e^{1+d\varphi}) = C'e^{-i\omega t} \tag{2.5}$$

at the encounter point of u and v, a new wave was created with the same period of the two but a different amplitude. As long as X-ray is a magnetic wave with a particular wavelength range, the interference of X-ray is nothing else, other than eq. (2.5).

Imagine two electrons both scatter X-ray and the wave added up as

$$u(\boldsymbol{q}) = -r_0(1 + e^{i\boldsymbol{q}\cdot\boldsymbol{r}}). \tag{2.6}$$

$\boldsymbol{q}$ is the scattering vector, which is the vector difference of the two scattered X-ray. $\boldsymbol{r}$ is the distance of the 2nd electron measured from the 1st electron. The phase discrepancy $d\varphi$ is equivalent to their inner product $\boldsymbol{q} \cdot \boldsymbol{r}$.

Since the intensity is the squared volume of a wave function:

$$I(\boldsymbol{q}) = u(\boldsymbol{q})u^*(\boldsymbol{q}) = -2r_0{}^2(1 + \cos(\boldsymbol{q} \cdot \boldsymbol{r})) \subseteq [-4r_0{}^2 \sim 0]. \quad (2.7)$$

For an atom, electrons are the origin of X-ray scattering. Therefore, for an atom with j electrons, the amplitude detected at $\boldsymbol{q}$ would be substitute eq. (2.6) into the generalized version of eq. (2.5):

$$u_{atom}(\boldsymbol{q}) = -r_0 \sum_j e^{i\boldsymbol{q}\cdot r_j} = -r_0 \int \rho(\boldsymbol{r})e^{i\boldsymbol{q}\cdot r}\mathrm{d}r = -r_0 f^0 \qquad (2.8)$$

$$f^0 = \begin{cases} Z \text{ for } \boldsymbol{q} \to 0 \\ 0 \text{ for } \boldsymbol{q} \to \infty \end{cases} \qquad (2.9)$$

where f^0 is called the form factor of an atom, which implies the relationship of the atom and the amplitude of scattered X-ray without considering the phase change in refraction and absorption, i.e. the $f(\boldsymbol{q}, h\omega) = f^0(\boldsymbol{q}, h\omega) + f'(\boldsymbol{q}, h\omega) + if''(\boldsymbol{q}, h\omega)$; Z is the number of electrons in the atom. The scattered intensity from an atom is various by its electron distribution, or consequently the element.

For crystalline materials, it is easier to consider the scattered X-ray using its unit cell:

$$u_{crystal\ lattice}(\boldsymbol{q}) = \sum_n u_{unitcell}(\boldsymbol{q}) = -r_0 \sum_n e^{i\boldsymbol{q}\cdot R_n} \sum_j f^0(\boldsymbol{q})e^{i\boldsymbol{q}\cdot r_j}. \quad (2.10)$$

The resonant oscillation also occurs in the atoms, for the reason that the process of scattering X-ray by an electron is a forced oscillation. Due to this reason, the resonance frequency (energy) is always observed as the absorption edge in the absorption spectrum, whose value depends on the element of the atom. This resonant scattering is also called anomalous scattering.

2.2.1.1.2. Interference in SAXS

It is easy to demonstrate that within the several degrees of scattered angle, the mean distance of the scatterers is in the order of nanometer. Consider the scattering shown as Fig. 2.2.2, the geometric relationship of the experimental parameters would be:

$$\lambda = 2d \sin \theta \qquad (2.11)$$

where λ is the wave length of incident X-ray, d is the distance of scatterers, 2θ is the scattered angle.

Therefore, within the conventional scattered angle range $2\theta < 5°$ in the SAX

measurement, and using *Kα* characteristic X-ray of Copper with 1.54 Å wave length as incident X-ray, the restriction of d would be $d > 1.77$ nm. This result indicates that the information of an atomic structure with a sub-nano-order would be observed at a scattered angle outside of the SAXS region.

Also, for an atomic structure with a large span, i.e., micrometer sized precipitates, the scattered intensity would fall on a lower angle region of the SAXS region, which usually overlaps with the finite-sized incident X-ray beam, or stopped by the beam-stop which protecting the detector from overcharged by the intensive transmitted X-ray.
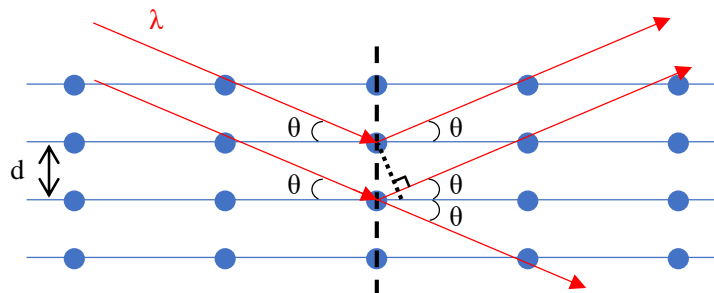
Fig. 2.2.2 A schematic illustration of interference takes place in scatterers with periodically structured

2.2.1.2. Intraference in SAXS
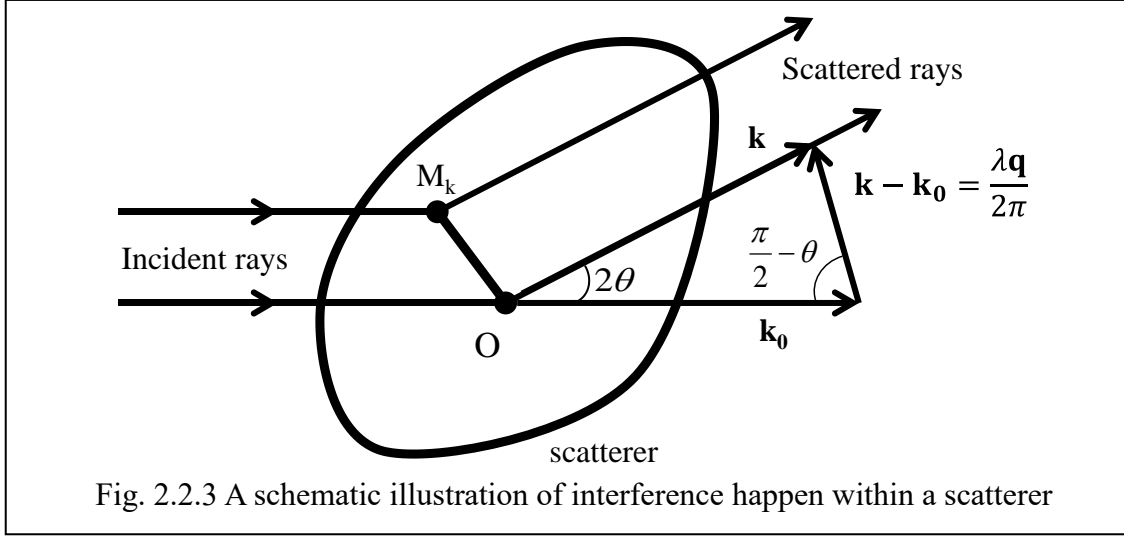
Fig. 2.2.3 A schematic illustration of interference happen within a scatterer

As mentioned in 2.2.1, the "intraference" is simply the interference occurred within a single scatterer like precipitate in an alloy. Now consider the intraference observed in a scatterer as shown in Fig. 2.2.3. Two X-rays illuminate the point **O** and **M$_k$** inside the scatterer, then the interference A_k and the intensity I_k would be:

$$A_k = A_e \rho(\boldsymbol{M_k}) \mathrm{d}v_k \left(1 + e^{i\boldsymbol{q} \cdot \boldsymbol{OM_k}}\right) = A_e \rho(\boldsymbol{M_k}) \mathrm{d}v_k \left(1 + e^{-i\frac{2\pi}{\lambda}(\boldsymbol{k}-\boldsymbol{k_0}) \cdot \boldsymbol{OM_k}}\right) \qquad (2.12)$$

$$I_k = A_k \cdot A_k{}^* = A_e{}^2 \rho^2(\boldsymbol{M_k}) \mathrm{d}v_k{}^2 (1 + \cos(\boldsymbol{q} \cdot \boldsymbol{r}))$$

$$= A_e{}^2 \rho^2(\boldsymbol{M_k}) \mathrm{d}v_k{}^2 \left(1 + e^{-i\frac{2\pi}{\lambda}(\boldsymbol{k}-\boldsymbol{k_0}) \cdot \boldsymbol{OM_k}}\right) = I_e(\boldsymbol{q})\left(1 + F^2(\boldsymbol{q})\right). \quad (2.13)$$

Where $\boldsymbol{k_0}$ and $\boldsymbol{k}$ is the wave vector of the incident and scattered X-ray; $\boldsymbol{q}$ is the scattering vector. Using the relationship of the matter and the wave length of the incident X-ray beam shown as eq. (2.11), and the definition of a wave vector $\boldsymbol{k} = 1/\lambda$, the definition of the scattering vector would be $\boldsymbol{q} = (4\pi/\lambda) \sin\theta$.

$I_e = A_e{}^2$ is the absolute intensity calculated from the absolute amplitude in the scattered X-ray without considering their interference. Eq. (2.13) indicates that $I_e F^2(\boldsymbol{q})$ is the only term needed to be considered.

When the incident X-ray illuminates the whole scatterer, then eq. (2.12) and (2.13) would be:

$$A(\boldsymbol{q}) = \int_i A_i = A_e \int_i \rho(\boldsymbol{M_i}) \mathrm{d}v_i \, e^{i\boldsymbol{q} \cdot \boldsymbol{OM_i}} \qquad (2.14)$$

$$I(\boldsymbol{q}) = A \cdot A^* = A_e{}^2 \int_i \int_j \rho(\boldsymbol{M_j}) \rho(\boldsymbol{M_i}) \cos(\boldsymbol{q} \cdot \boldsymbol{r}) \, \mathrm{d}v_j \mathrm{d}v_i$$

$$= A_e{}^2 \rho^2(\boldsymbol{M_k}) \mathrm{d}v_k e^{-i\frac{2\pi}{\lambda}(\boldsymbol{k}-\boldsymbol{k_0}) \cdot \boldsymbol{OM_k}} = I_e(\boldsymbol{q}) F^2(\boldsymbol{q}). \quad (2.15)$$

F(q) is known as the form factor of the scatterer, which determined by the three-dimensional shape of the scatterer.

For a scatterer with a finite volume, both two of the concerned points has to be inside the scatterer when considering the interference. Therefore, after designating a random point in the scatterer as $\boldsymbol{O}$, how much the probability it would be that the other point $\boldsymbol{M_k}$ locates also inside the scatterer to generate the second array of X-ray for interference. This is defined as probability with a "characteristic function γ_0" (Porod, 1951), or autocorrelation function identically,

$$\gamma_0 = \frac{\overline{V(\boldsymbol{r})}}{V} \qquad (2.16)$$

where V is the volume of the scatterer; $\overline{V(\boldsymbol{r})}$ is a mean value that after the scatterer moved its position by a vector **r**, the volume overlaps with the original, or the volume still stay inside the unmoved scatterer:

$$\overline{V(\boldsymbol{r})} = \frac{1}{4\pi} \int_0^{4\pi} V(\boldsymbol{r}) \mathrm{d}\omega \qquad (2.17)$$

Fig. 2.2.4 A schematic illustration interpreting the relationship of $V(\boldsymbol{r})$, the original scatterer with volume V and vector **r**

16
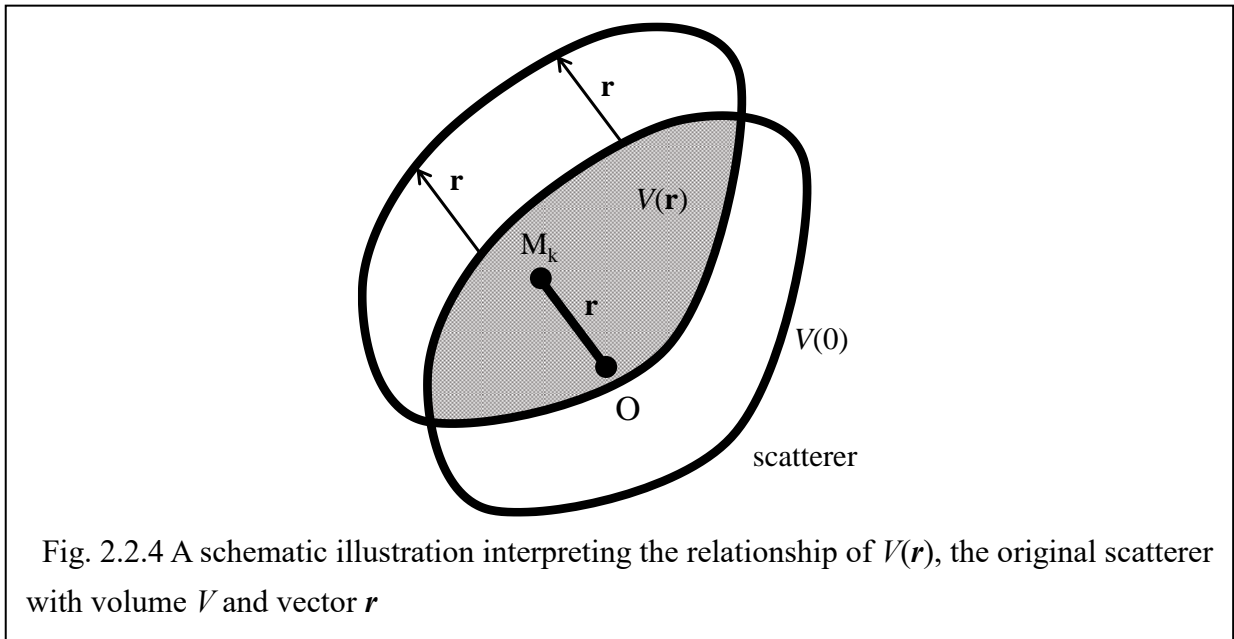
2.2.1.2.1. Scattered intensity profile from a scatterer

For an isotropic scatterer, the intensity on any direction is identical to the mean value of all the direction:

$$F^2(\boldsymbol{q}) = \overline{F^2(\boldsymbol{q})} = \int_i \int_j \rho(M_j)\rho(M_i)\cos(\boldsymbol{q}\cdot\boldsymbol{r})\,\mathrm{d}v_j\mathrm{d}v_i$$

$$= \rho^2 \int_0^\infty \overline{V(r)\cos(\boldsymbol{q}\cdot\boldsymbol{r})}\cdot 4\pi r^2\mathrm{d}r. \tag{2.18}$$

where

$$\overline{\cos(\boldsymbol{q}\cdot\boldsymbol{r})} = \int_0^\pi \cos(qr\cos\varphi)\frac{\sin\varphi}{2}\,\mathrm{d}\varphi$$

$$= -\frac{1}{qr}\int_{qr}^0 \cos u\,\mathrm{d}u = \frac{\sin qr}{qr}. \tag{2.19}$$

Therefore:

$$\overline{F^2(\boldsymbol{q})} = \int_k \int_j \rho(M_j)\rho(M_k)\overline{\cos(\boldsymbol{q}\cdot\boldsymbol{r})}\,\mathrm{d}v_j\mathrm{d}v_k$$

$$= \int_k \int_j \rho(M_j)\rho(M_k)\,\mathrm{d}v_j\mathrm{d}v_k\frac{\sin q|\boldsymbol{M_kM_j}|}{q|\boldsymbol{M_kM_j}|}. \tag{2.20}$$

If considering the centrosymmetry in this isotropic scatterer, then scattered intensity from point M_k can be:

$$\overline{F^2(\boldsymbol{q})} = \int_k \rho^2(M_k)\frac{\sin q|\boldsymbol{OM_k}|}{q|\boldsymbol{OM_k}|}\mathrm{d}v_k \tag{2.21}$$

$$\overline{F^2(\boldsymbol{q})} = \int_k \int_j \rho(M_j)\rho(M_k)\,\mathrm{d}v_j\mathrm{d}v_k\frac{\sin q|\boldsymbol{M_kM_j}|}{q|\boldsymbol{M_kM_j}|}$$

$$= \overline{\rho}^2 V \int_0^\infty \gamma_0(r)\frac{\sin qr}{qr}\cdot 4\pi r^2\mathrm{d}r \tag{2.22}$$

where $\overline{\rho}$ is the averaged density in this scatterer.

When a scatterer is anisotropic, then possible to evaluate the scatterer by taking an average by changing γ_0. Table 2.2.1 shows several examples of the form factors.

Table 2.2.1 Form factors of several kinds of scatterers

sphere with radius R	$F_1(q) = \dfrac{3[sin(qR) - qR\,cos(qR)]}{(qR)^3}$
sphere shell with outer radius R_1, inner radius R_2 (V(R)=4πR³/3)	$F_2(q) = \dfrac{V(R_1)F_1(q,Rq) - V(R_2)F_1(q,R_2)}{V(R_1) - V(R_2)}$
ellipsoid (axis: R, R, εR)	$F_3{}^2(q,R,\varepsilon) = \displaystyle\int_0^{\pi/2} F_1{}^2[q, r(R,\varepsilon,\alpha)]\, sin\,\alpha\, d\alpha$ where $r(R,\varepsilon,\alpha) = R\sqrt{sin^2\,\alpha + \varepsilon^2\,cos^2\,\alpha}$

2.2.1.2.2. The relationship of the volume of a scatterer and the SAXS profile

It is possible to derive volume of the scatterer from eq. (2.22) by inverse Fourier transformation:

$$r\gamma_0(r) = \frac{2}{\pi}\int_0^\infty \frac{q\,\overline{F^2(q)}}{4\pi\bar\rho^2 V}\sin qr\, dq$$

$$\gamma_0(r) = \frac{1}{2\pi^2\bar\rho^2 V}\int_0^\infty q^2\overline{F^2(q)}\frac{\sin qr}{qr}dq \qquad (2.23)$$

If $r = 0$, then

$$\gamma_0(0) = \frac{\overline{V(0)}}{V} = 1$$

$$(23) = \gamma_0(0) = 1 = \frac{1}{2\pi^2\bar\rho^2 V}\int_0^\infty q^2\overline{F^2(q)}dq$$

$$\int_0^\infty q^2\overline{F^2(q)}dq = 2\pi^2\bar\rho^2 V. \qquad (2.24)$$

Eq. (2.23) shows the integrated value of $q^2 I dq$ is a value accordance with the volume of scatterer V (or volume fraction, if the volume of specimen is known) and squared mean value of electron density $\bar\rho^2$. Integrated intensity is usually represented with a letter Q.

2.2.1.2.3. The relationship of the radius of a scatterer and the SAXS profile

In section 2.2.1.1.1, the form factor f^0 linked the scattered wave and an atom; but in the case of SAXS, the elementary matter for the interference is a volume fraction, rather than an atom. Therefore, a new form factor may be introduced as f_j, which links the scattered wave from a volume element dv_j on position M_j. Then:

$$A_j = A_e f_j e^{-i\frac{2\pi}{\lambda}(k-k_0)\cdot OM_j}$$

$$f_j = \rho dv_j \tag{2.25}$$

And recall eq. (2.20) with the application of Tylor series,

$$\overline{F^2(q)} = \int_k \int_j \rho(M_j)\rho(M_k)\, dv_j dv_k \frac{\sin q|M_k M_j|}{q|M_k M_j|} = \sum_j \sum_k f_k f_j \frac{\sin q|OM_k|}{q|OM_k|}$$

$$= \left(\sum_k f_k\right)^2 \left(1 - \frac{q^2}{3}\frac{\sum_k f_k|OM_k|^2}{\sum_k f_k} + \cdots\cdots\right). \tag{2.26}$$

In the physics of Rigid Body, radius of gyration is defined with the moment of inertia

$$I_{moment\ of\ inertia} = \sum_i m_i r_i^2 \tag{2.27}$$

$$R_g = \frac{I}{\sum_i m_i} = \frac{\sum_i m_i r_i^2}{\sum_i m_i} \tag{2.28}$$

where $I_{moment\ of\ inertia}$ is moment of inertia, m_i the mass at point i, r_i the distance from the center to the point i.

It is obvious that the second item in (2.28) is similar to the second term in (2.26). Therefore, the radius of gyration could be derived from the famous Guinier plot of plotting of $\ln(I) - q^2$ and the radius of gyration, or also called Guinier radius which would be:

$$R_g = \frac{\sum_k f_k r_k^2}{\sum_k f_k}. \tag{2.29}$$

Some of the relationship of R_g and the geometric parameters are shown in Table 2.2.2.

Table 2.2.2 Several relationships of R_g and scatterers

Shape of scatterer	Parameter of Shape	Relationship
Sphere	Radius R	$R_g{}^2 = (3/5)R^2$
Cylinder	Radius r, Length L	$R_g{}^2 = (r^2/2) + (L^2/12)$
Ellipsoid	Length of Semi-major axis a, a, va	$R_g{}^2 = a^2(2 + v^2)/5$
Thin disc	Radius R	$R_g{}^2 = R^2/2$
Thin bar	Length L	$R_g{}^2 = L^2/12$
Rectangular Cuboid	$2a$, $2b$, $2c$	$R_g{}^2 = (a^2 + b^2 + c^2)/3$

2.2.1.2.4. Consideration with fluctuation of electron density

Electrons are known as the origin of scattering in X-ray, but as mentioned in the section 2.2.1.2.3, for SAXS measurement, the elementary matter is not an atom, but the elementary volume. Therefore, it is necessary to have another look at the origin of the SAXS intensity, by focusing on the electrons in the elementary volume, i.e. electron density and its oscillation (Guinier & Fournet, 1955; Brumberger, 1965).

Let

$$\rho(\boldsymbol{x}) = \bar{\rho} + \Delta\rho(\boldsymbol{x}) \tag{2.30}$$

where $\bar{\rho}$ designates the average electron density of the material, then

$$\int \Delta\rho(\boldsymbol{x})\mathrm{d}\boldsymbol{x} = 0. \tag{2.31}$$

If recall the expression of scattered intensity of (2.13) and (2.15),

$$I(\boldsymbol{q}) = I_e(\boldsymbol{q}) \int_V \int_V [\bar{\rho} + \Delta\rho(\boldsymbol{x_k})][\bar{\rho} + \Delta\rho(\boldsymbol{x_j})]e^{-i\boldsymbol{q}\cdot(\boldsymbol{x_k}-\boldsymbol{x_j})}\,\mathrm{d}\boldsymbol{x_k}\mathrm{d}\boldsymbol{x_j} \tag{2.32}$$

so eq. (2.16) is what needed to be focused on.

Guinier and Fournet (1955) discussed eq. (2.32) by the four terms of $\bar{\rho}^2$, $\bar{\rho}\Delta\rho(\boldsymbol{x_k})$, $\bar{\rho}\Delta\rho(\boldsymbol{x_j})$ and $\Delta\rho(\boldsymbol{x_k})\Delta\rho(\boldsymbol{x_j})$ respectively:

First term $\bar{\rho}^2$:

$$I_1(\boldsymbol{q}) = I_e(q)\bar{\rho}^2 \int_V \int_V e^{-i\boldsymbol{q}\cdot(\boldsymbol{x}_k-\boldsymbol{x}_j)} \, \mathrm{d}\boldsymbol{x}_k \mathrm{d}\boldsymbol{x}_j \tag{2.33}$$

(2.33) is practically Zero for all observable angles (Guinier & Fournet, 1955).

Second and third term $\bar{\rho}\Delta\rho(\boldsymbol{x}_k)$, $\bar{\rho}\Delta\rho(\boldsymbol{x}_j)$:

$$I_2(\boldsymbol{q}) + I_3(\boldsymbol{q}) = 2\mathrm{Re}\left\{I_e(q)\bar{\rho}\int_V \Delta\rho(\boldsymbol{x}_k)\mathrm{d}\boldsymbol{x}_k \int_V e^{-i\boldsymbol{q}\cdot(\boldsymbol{x}_k-\boldsymbol{x}_j)} \, \mathrm{d}\boldsymbol{x}_j\right\} \tag{2.34}$$

or

$$I_2(\boldsymbol{q}) + I_3(\boldsymbol{q}) = 2I_e(q)\mathrm{Re}\left\{\int_V \Delta\rho(\boldsymbol{x}_k)e^{-i\boldsymbol{q}\cdot\boldsymbol{x}_k}\mathrm{d}\boldsymbol{x}_k \int_V \bar{\rho}e^{i\boldsymbol{q}\cdot\boldsymbol{x}_j} \, \mathrm{d}\boldsymbol{x}_j\right\} \tag{2.35}$$

(2.34) and (2.35) are negligible compared as fourth term (Guinier & Fournet, 1955)

Fourth term $\Delta\rho(\boldsymbol{x}_k)\Delta\rho(\boldsymbol{x}_j)$:

$$I_4(\boldsymbol{q}) = I_e(q)\int_V \int_V \Delta\rho(\boldsymbol{x}_k)\Delta\rho(\boldsymbol{x}_j)e^{-i\boldsymbol{q}\cdot(\boldsymbol{x}_k-\boldsymbol{x}_j)} \, \mathrm{d}\boldsymbol{x}_k\mathrm{d}\boldsymbol{x}_j. \tag{2.36}$$

Let set $\boldsymbol{x}_j = \boldsymbol{x}_k + \boldsymbol{r}$, then

$$I_4(\boldsymbol{q}) = I_e(q)\int_V \int_V \Delta\rho(\boldsymbol{x}_k)\Delta\rho(\boldsymbol{x}_k + \boldsymbol{r})e^{-i\boldsymbol{q}\cdot\boldsymbol{r}} \, \mathrm{d}\boldsymbol{x}_k\mathrm{d}\boldsymbol{r}. \tag{2.37}$$

If consider $\boldsymbol{x}_k$ first:

$$\int_V \Delta\rho(\boldsymbol{x})\Delta\rho(\boldsymbol{x} + \boldsymbol{r})\mathrm{d}\boldsymbol{x} \tag{2.38}$$

then

$$\int_V \Delta\rho(\boldsymbol{x})\Delta\rho(\boldsymbol{x})\mathrm{d}\boldsymbol{x} = \int_V \Delta\rho^2(\boldsymbol{x})\mathrm{d}\boldsymbol{x} = \overline{\Delta\rho^2}V. \tag{2.39}$$

If define a function $\gamma(\boldsymbol{r})$ by Debye and Bueche (1949):

$$\int_V \Delta\rho(\boldsymbol{x})\Delta\rho(\boldsymbol{x} + \boldsymbol{r})\mathrm{d}\boldsymbol{x} = \overline{\Delta\rho^2}V\gamma(\boldsymbol{r}) \tag{2.40}$$

then

$$I_4(\boldsymbol{q}) = I_e(q)\overline{\Delta\rho^2}V \int_V \gamma(\boldsymbol{r})e^{-i\boldsymbol{q}\cdot\boldsymbol{r}}\mathrm{d}\boldsymbol{r} \tag{2.41}$$

Therefore, consequently:

$$I(\boldsymbol{q}) = I_4(\boldsymbol{q}) = I_e(q)\overline{\Delta\rho^2}V \int_0^\infty \gamma(r)\frac{\sin qr}{qr}4\pi r^2 dr. \tag{2.42}$$

21

This implies that the measured intensity in SAXS is practically originated from the difference in the local electron density and the squared mean electron density, i.e., $\overline{\Delta\rho^2}$ of precipitates and the matrix in a metallic alloy.

2.3. Enhancement and control of contrast in SAXS analysis

2.3.1. Standardization of scattered intensity in SAXS method

The absolute scattered intensity emitted from a single electron I_e could be expressed as below (Guinier & Fournet, 1955):

$$I_e = A_e{}^2(\boldsymbol{q}) = r_0{}^2 I_0 p^{-2} P \tag{2.43}$$

where r_0 is the classic radius of an electron, I_0 is the absolute intensity of the incident X-ray beam, p is the camera length, P is the polarization factor mentioned in the section 2.2, which is 1 when the detector is vertical to the polarization direction of the incident X-ray like the experiments in this treatise.

The absolute intensity is an intensive parameter introduced as differential scattered intensity in the section 2.2, so the detected intensity $I_{sc} \propto I_e$ has to be divided with the solid angle of one detector element $\Delta\Omega$:

$$\left(\frac{d\sigma}{d\Omega}\right) = \left(\frac{\Delta\sigma}{\Delta\Omega}\right) = \frac{I_{sc}}{\Delta\Omega}. \tag{2.44}$$

Therefore, the absolute value of scattered intensity, i.e. differential scattered intensity (or the total scattered intensity mentioned in the section 2.2) of SAXS is now derivable.

2.3.2. Calibration method in quantitative nanostructure analysis by scanning microbeam SAXS method

2.3.2.1. Calibration with different detectors

Practically, a calibration is often needed for the measured X-ray intensities, due to the difference in linearity of input-output response in different detectors. This inconsistency occurs when different types of detectors like SDD and ion chamber are used together, or even take places when using the same type of detectors but different in the sensitivity, e.g. using ion chambers with different sizes.

Ideally, when two different detectors which have a same linearity in responding, the output data converted from a common input data is expected to be the same. E.g., if two detectors measuring the incident and the transmitted X-ray as I_0 and I_1 respectively, and if there is nothing exists between these two detectors, then the transmittance T should be one and $I_0 = I_1$. Then, a specimen was put in between these two detectors and penetrated by the X-ray, then the transmittance would be:

$$T_{ideal}^s = \frac{I_1{}^s}{I_0{}^s}. \tag{2.45}$$

Practically, the response of the two detectors are not the same, i.e. $T_{real} \neq 1$, $I_0 \neq I_1$,

then the linearity of detectors have to be calibrated. When a specimen is measured, the output transmittance of this system would be:

$$T_{real}^{s} = \frac{I_1{}^{s}/I_1}{I_0{}^{s}/I_0}.$$

(2.46)

When the output value is needed for a precise value, then the influence from the dark current which occurs when connected to electricity $I_0{}^{dark}$ and $I_1{}^{dark}$, have to be eliminated from the outputted data for each detector. This influence can be measured by checking the output intensity without exposing X-ray, and then eq. (2.46) would be:

$$T_{real}^{s} = \frac{\left(I_1{}^{s} - I_1{}^{dark}\right)/\left(I_1 - I_1{}^{dark}\right)}{\left(I_0{}^{s} - I_0{}^{dark}\right)/\left(I_0 - I_0{}^{dark}\right)}.$$

(2.47)

Therefore, the calibration for different detectors is completed.

2.3.2.2. Scattering intensity separation from other intensity

For a measurement detected ideally, the measured intensity can be expressed with a function below (Hendricks, 1972; Osamura & Okuda, 1983):

$$A \cdot \left[\frac{E(\mathbf{q})}{E_0(\mathbf{q})} \right] = tTJ_{coh}(\mathbf{q}) + tTJ_{fl}(\mathbf{q}) + TJ_{B.G.}(\mathbf{q})$$

(2.48)

where A is a constant links the relative and absolute intensity; $E(\mathbf{q})$ is the measured relative intensity at a scattering vector $\mathbf{q}$; $E_0(\mathbf{q})$ is the relative intensity measured with standard specimen. Both $E(\mathbf{q})$ and $E_0(\mathbf{q})$ have to be adjusted with the same intensity of incident X-ray; t is the thickness of the specimen X-ray has passed; T is the transmittance of the measurement; $J_{coh}(\mathbf{q})$ is the scattered intensity profile; $J_{fl}(\mathbf{q})$ is the fluorescent X-ray emitted from the atom in the specimen; $J_{B.G.}(\mathbf{q})$ is the parasitic scattering intensity from the experimental apparatus, as well as synchrotron facility.

T is derivable with the incident/transmitted X-ray, and t is available when the component of the specimen that X-ray passed through is known. Variable t can be estimated form the attenuation coefficient μ_{alloy} using the exponential law (Hubbell, 1982):

$$-dI = I\mu_{alloy}dx$$
$$I_1 = I_0 e^{-\mu_{alloy}t}$$

(2.49)

where dI is the decrement in X-ray after going through a specimen with a thickness dx. The attenuation coefficient of the material μ_{alloy} is estimated with the mass absorption coefficient μ_{alloy}/ρ_{alloy} of the material by dividing the material's density ρ_{alloy}. The mass absorption coefficient of the material is known as the summation of which of the

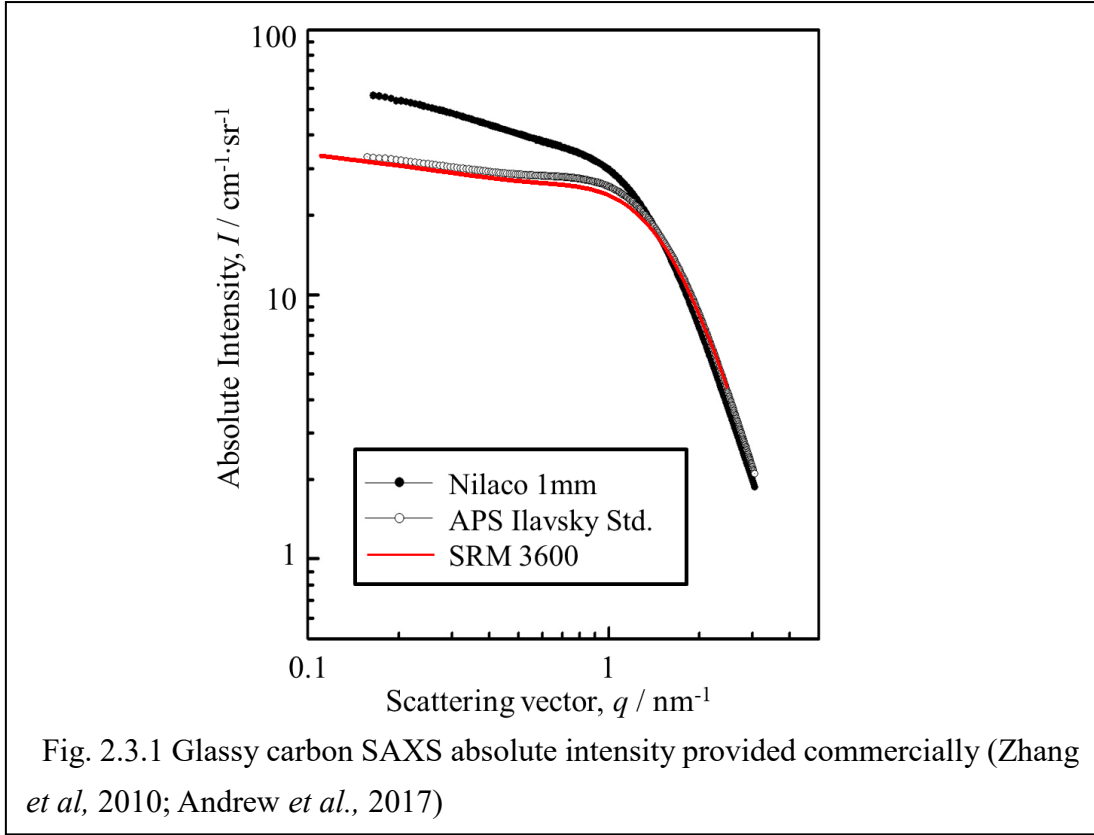comprising element j, and the mass fraction ω_j as below:

$$\left(\frac{\mu}{\rho}\right) = \sum_{j=1}^{n} \omega_j \left(\frac{\mu}{\rho}\right)_j. \tag{2.50}$$

When both the component elements ω_j and the local thickness t fluctuates at the same time—like the in this treatise—it is impossible to determine both of the information simultaneously. Therefore, the investigation by SEM-EDX 1D line scanning/2D mapping was performed on the specimens, and the solute concentration distributions were the determined for each SAXS specimen using master curves.

$(\mu/\rho)_j$ can be found in other researcher's work summarized in e.g. NIST (National Institute of Standards and Technology) database, ρ of the local material with can be estimated with the unit cell of the material and the atomic weight, atomic fraction for each element. With all data above, the thickness of specimen t was acquired locally.

$J_{B.G.}(\mathbf{q})$ was confirmed by measuring SAXS profile with X-ray exposed without specimen. $J_{fl}(\mathbf{q})$ was considered constant for all angles, for no directivity observed in the fluorescent X-ray. $J_{fl}(\mathbf{q})$ was estimated by checking the deviation from the ideal profile of the porod's rule, i.e. $I(\mathbf{q}) \propto \mathbf{q}^{-4}$ (Guinier & Fournet, 1955; Brumberger, 1956), and the measured 1D SAXS profile in the porod's area.

2.3.2.3. Calibration of absolute scattered intensity

Fig. 2.3.1 Glassy carbon SAXS absolute intensity provided commercially (Zhang *et al*, 2010; Andrew *et al.,* 2017)

From eq. (2.15) (2.43) (2.44):

$$\left(\frac{\mathrm{d}\sigma}{\mathrm{d}\Omega}\right) = \frac{I_{sc}}{\Delta\Omega} = I_e F^2(q) = A_e^{\,2}(q)F^2(q) = \mathrm{r_0}^2 I_0 p^{-2} P F^2(q) \qquad (2.51)$$

it is apparent that the relative and absolute intensity is proportional when the scattered intensity is regulated with solid angle $\Delta\Omega$, with a coefficient composed by r_0, I_0, p and P. Each of them is either a constant, or a fixed value that can be measured. Therefore, using standard specimens with known SAXS profiles are widely used for conducting the coefficient of relative and absolute intensity.

Glassy carbon is a common specimen provided commercially for SAXS measurement in these years. Fig. 2.3.1 shows the relationship of several SAXS profile by glassy carbon made differently: (a) SRM 3600, provided by NIST (Andrew *et al.,* 2017) (b) standard specimen provided by Dr. Jan Ilavsky from Advanced Photon Source (APS), Argonne National Laboratory (Zhang *et al*, 2010) (c) production by The Nilaco Corporation. SRM 3600 was supplied by NIST for the validity in standardization usage, so this can be the first-hand material for standardization. Here should be noted that the 1 mm thickness of SRM 3600 has to be considered while the calibrating into absolute intensity, and the unit

is cm^{-1}·sr^{-1}, not cm^{-3}·sr^{-1}.

2.4. Visualization of inner structure by scanning/tomographic SAXS

In order to conduct a spatial investigation on the multilayered composites about local nanostructural distribution, the SAXS method with the application of 1D scanning, and 2D tomographic measurement using microbeam X-ray was performed.

The schematic illustration of 1D scanning measurement is shown in Fig. 2.4.1 left. In this experiment, the local nanostructural distribution was investigated by the 2D SAXS profile illuminated locally by microbeam X-ray. After a SAXS measurement was finished in particular location on specimen, the specimen was moved along x direction for specific distance, and another SAXS measurement was conducted on a different area of specimen. This process was repeated as a scanning process, and the moving spotted area traverse the whole specimen on the x direction, which is also the normal direction (ND) of the rolled multilayered composite.

The schematic illustration of 2D tomographic measurement is shown in Fig. 2.4.1. right. In this experiment, in addition to the translation movement on x-direction mentioned for 1D scanning, a rotation movement by steps were conducted on the specimen repeatedly. In order to illuminate all area on a specific cross-section of specimen at every few angles, the full rotation movement was performed on each translated step on x-direction. The specimen was also scanned edge to edge to cover all the area in the cross-section of specimen.
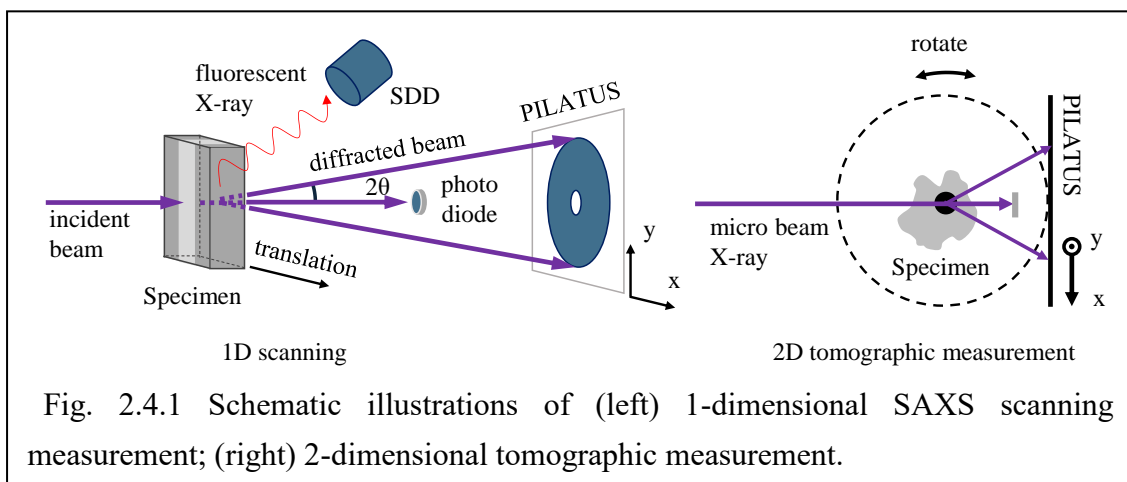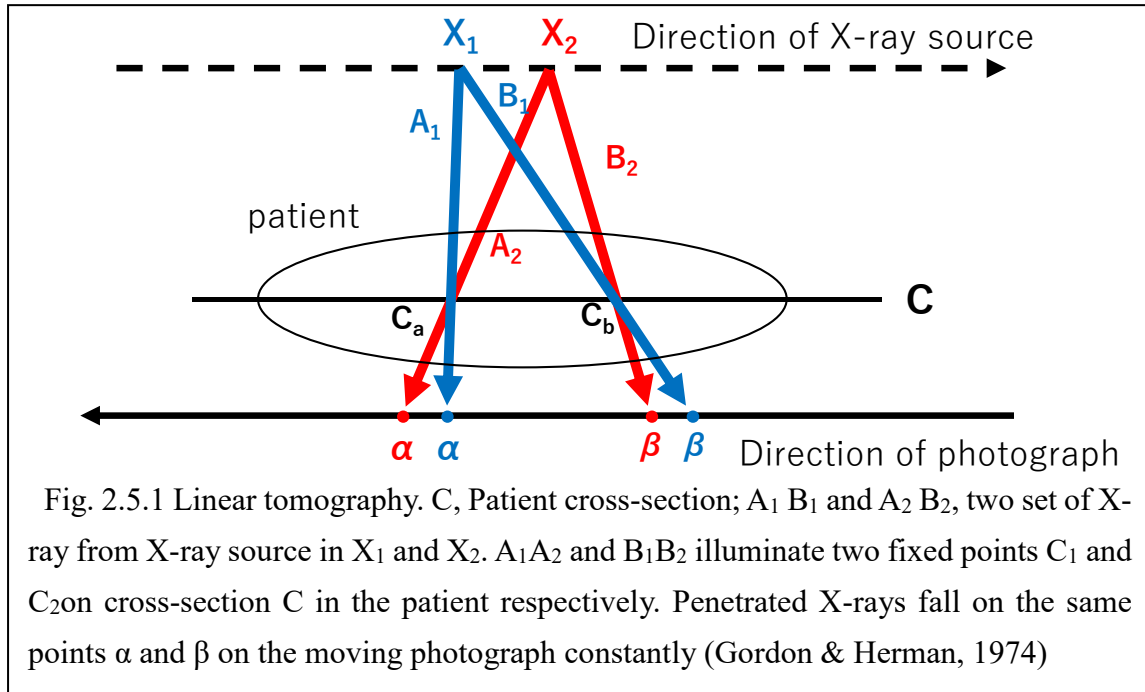

Fig. 2.4.1 Schematic illustrations of (left) 1-dimensional SAXS scanning measurement; (right) 2-dimensional tomographic measurement.

2.5. Computed Tomography

2.5.1. Computed tomography with summation method

Fig. 2.5.1 Linear tomography. C, Patient cross-section; $A_1 B_1$ and $A_2 B_2$, two set of X-ray from X-ray source in X_1 and X_2. A_1A_2 and B_1B_2 illuminate two fixed points C_1 and C_2 on cross-section C in the patient respectively. Penetrated X-rays fall on the same points α and β on the moving photograph constantly (Gordon & Herman, 1974)

Tomography has been applicated in the field of clinics since 1920s according to French patents (see Kieffer, 1938), which has always been a method to investigate the structure inside the sample object nondestructively. Fig. 2.5.1 shows a schematic illustration of a method called linear tomography, which has been used in the early age of tomographic measurement. X_1 is an X-ray source and which stays above the measure target i.e. the patient all the time, emitting X-ray which covers the patient consistently. P is the photograph film placed under the patient for detecting the transmitted X-ray from the patient. When the X-ray source stays at X_1, then the two arrays of X-ray penetrating the patient by A_1 and B_1 respectively, and falls on α and β after absorbed by the patient on either of their path. Then, move the X-ray source to the X_2 and the photograph film to the left parallelly at the specific speed. With this operation, the absolute position on the photograph film of α and β was kept collecting the transmitted intensity of A_1 and B_1 to A_2 and B_2 intentionally. From Fig. 2.5.1 it is apparent that the light path A_1A_2 and B_1B_2 kept spotting two fixed point C_a and C_b on the cross-section C inside the patient, and these special points are unique for each absolute location on the photograph film. This emphasizes the absorption coefficient on C_a and C_b, also diminish the effect from other part of the patient by pilling up the information randomly.

The algorithm of the linear tomography, or the reconstruction for cross-section C is

simply the summation of the penetrated X-ray which absorbed by the patient from each direction, with a specific rotation center (C_a, C_b etc.) for each position on the photograph. The resulted tomography is considerably blur due to the noise effect from other unwanted cross-sections. Also, this linear tomographic is known for the spurious contours causing unsharp edge and artifacts subjected to the incident angle when fall on photograph (Kieffer, 1939; Reichman, 1972).

In order to sharpen the contour of the specimen, the incident X-ray was adjusted close to be normal to the photograph film, and the distance of the light path was kept constant by using a pencil X-ray source and a detector as a set, moving together to scan 1-dimensionally from different angles of the target cross-section, shown in Fig. 2.5.2. This technique was introduced by Kuhl and Edwards (1963) with a name of transverse section scanning. This technique already contains the process of "back projection" first named by Crowther *et al.* (1970B).

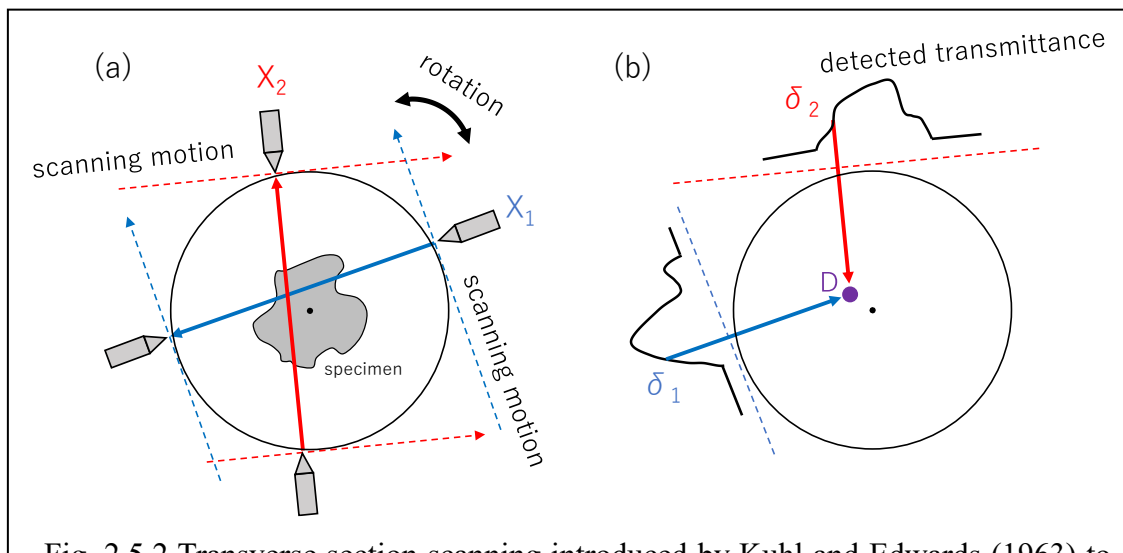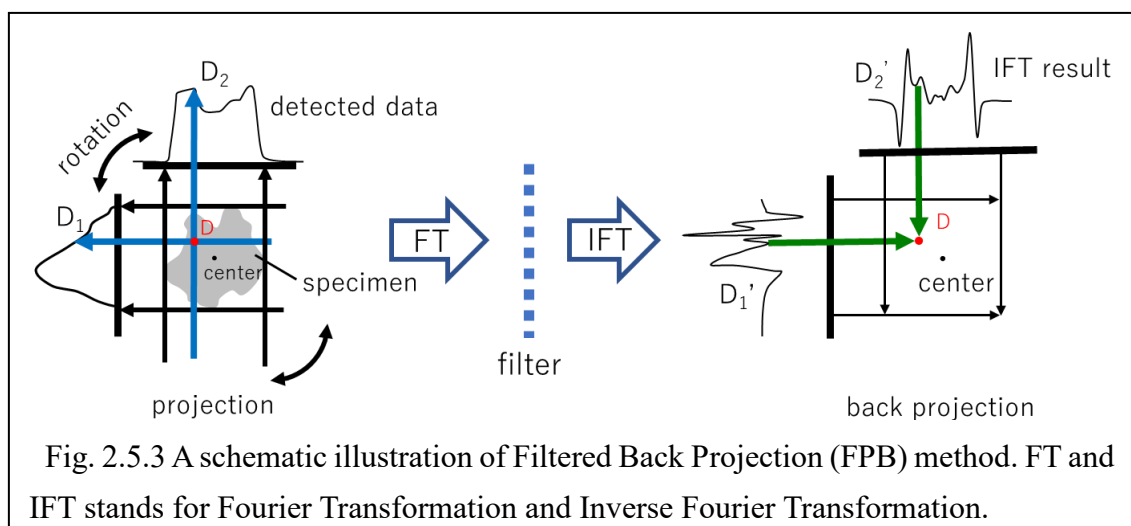Fig. 2.5.2 Transverse section scanning introduced by Kuhl and Edwards (1963) to avoid the problems in the linear tomography. 1D scanning performs on a target cross-section of the specimen from different angles and then sum up the results. This is relatively close to CT in commercial use today, but the algorithm is still summation only. Transmittance on point D is calculated as the summation of δ_1 and δ_2.

2.5.2. Computed tomography with reconstruction process

The Filtered Back Projection (FBP) is a method of reconstruction still widely used today in many fields of research. This method was developed for the solution of problem of the blurring around the sharp edge often observed in the attenuation coefficient tomography, both in the linear tomography and the transverse section scanning tomography. The procedure is shown in Fig. 2.5.3. The process is to insert a filter in the "frequency domain" as signal processing ("frequency domain" is identical to "reciprocal space", which is more familiar in the field of materials science), before back projecting to each pixel in the real domain. There are multiple filters known to use, e.g., Ramp filter, Hanning filter, Hamming filter, Butterworth filter, Ramachandran-Lakshminarayanan filter. Each filter has its advantage and disadvantage, and please refer to textbooks about image processing (Gonzalez & Woods, 2002), as it is about the appearance of an image and which is out of the focus of this treatise.

Another reconstruction process is called the Convolution Back Projection (CBP) method (see Desai & Jenkins, 1992), which is mathematically identical to FPB method, but instead of inserting the filter in the reciprocal space, it put in the real space. This multiplication has to be converted into the operation of convolution, due to the characteristic of Fourier transformation. This CBP method is reported to be more accurate (Nakano, T. *et al*., 2020) compared to FBP method.

Fig. 2.5.3 A schematic illustration of Filtered Back Projection (FPB) method. FT and IFT stands for Fourier Transformation and Inverse Fourier Transformation.

2.6. Quantitative Computed tomography

2.6.1. Detailed process of Computed Tomography (Radon transform)
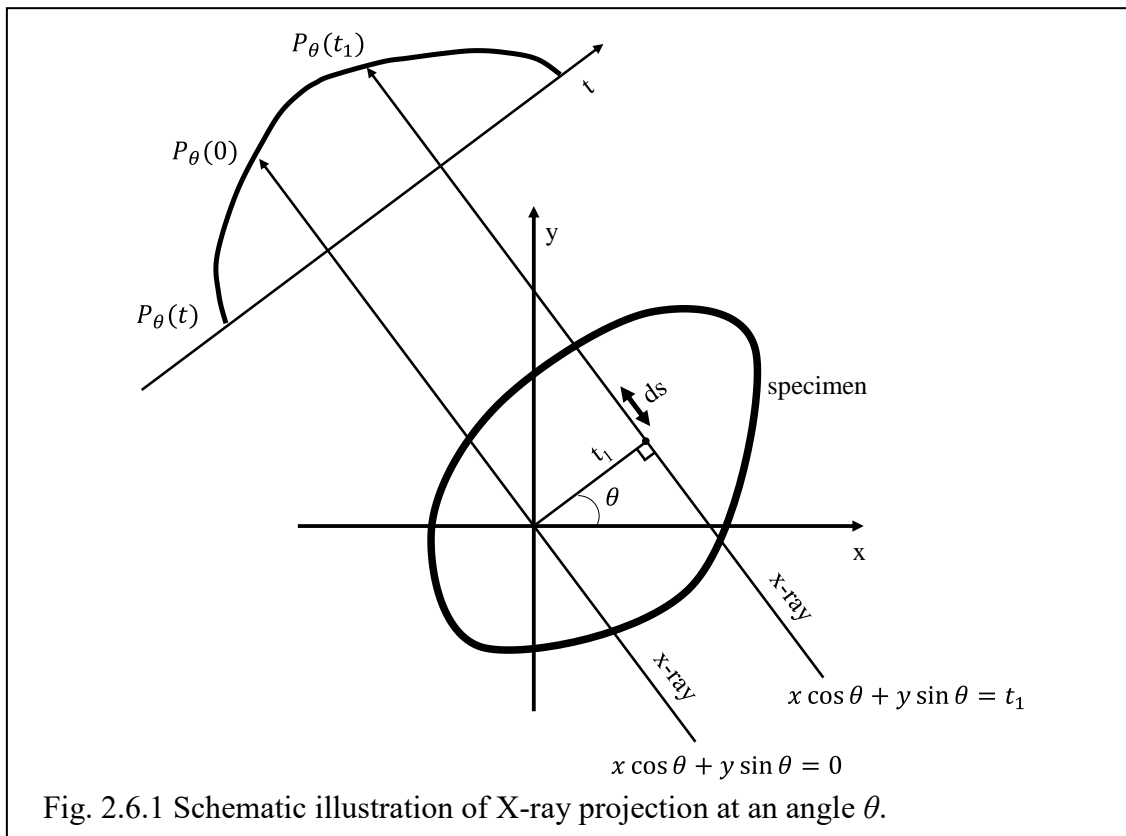
Fig. 2.6.1 shows the measuring process in a tomography experiment. When an X-ray array projects at an angle θ and with a distance from a fixed rotation point with t_1, then the projected attenuation coefficient measured is $P_\theta(t_1)$. This is a function of variable t, and every t can be expressed with x and y, which is the two axis of a fixed Cartesian coordinate system:

$$t = x \cos \theta + y \sin \theta. \tag{2.52}$$

Every $P_\theta(t)$ is a summation result of the small pixels with values of the mean attenuation coefficient for an element area $dxdy$ illuminated by X-ray perpendicular to the angle θ. Therefore, the distribution of projected values can be linked with the attenuation coefficient distribution of the specimen $f(x, y)$ with the following formula:

$$P_\theta(t) = \int_{(\theta,t)line} f(x,y)ds = \int_{-\infty}^{\infty} \int_{-\infty}^{\infty} f(x,y)\delta(x \cos \theta + y \sin \theta - t)dxdy. \tag{2.53}$$

This formula is known as Radon transform of the function $f(x, y)$. Eq. (2.53) is operational with any t at any fixed θ.

Fig. 2.6.1 Schematic illustration of X-ray projection at an angle θ.

2.6.2. The Fourier Slice Theorem and multiple dimensional Fourier transformation

Fig. 2.6.2 A schematic illustration showing 2D Fourier transformation with different coordinate systems. The fixed system is x-y system; The rotated system is t-s system at an angle θ.
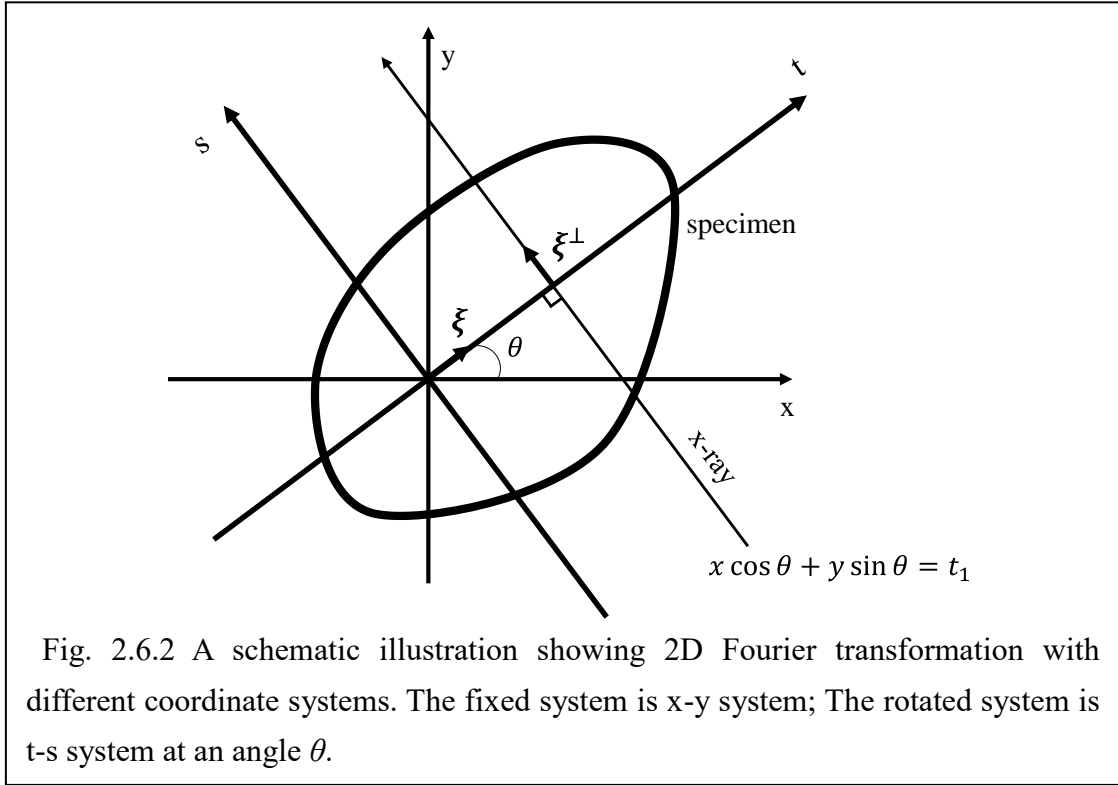
As shown in Fig. 2.6.2, by changing the base vector x and y to the t and s axis rotated at an angle θ, Radon transformation eq. (2.53) can be easier to be understood (see Dean, 1983):

$$\begin{pmatrix} x \\ y \end{pmatrix} = \begin{pmatrix} \cos\theta & -\sin\theta \\ \sin\theta & \cos\theta \end{pmatrix} \begin{pmatrix} t \\ s \end{pmatrix} \tag{2.54}$$

$$P_\theta(t) = \int_{(\theta,t)line} f(x,y)\mathrm{d}s$$

$$= \int_{-\infty}^{\infty} f(t\cos\theta - s\sin\theta, t\sin\theta + s\cos\theta)\mathrm{d}s \tag{2.55}$$

let $\boldsymbol{x} = (x,y)$, and the unit vector $\boldsymbol{\xi}$ and $\boldsymbol{\xi}^\perp$ for the t and s axis. Then

$$\begin{cases} \boldsymbol{\xi}(\cos\theta, \sin\theta) \\ \boldsymbol{\xi}^\perp(-\sin\theta, \cos\theta). \\ \boldsymbol{x} = t\boldsymbol{\xi} + s\boldsymbol{\xi}^\perp \end{cases} \tag{2.56}$$

All the pixels in the specimen which projected by a single array of X-ray can be converted as $\int \delta(t - \boldsymbol{\xi} \cdot \boldsymbol{x})\,\mathrm{d}x\mathrm{d}y$. Eq. (2.55) would be:

$$P_\theta(t) = \int_{(\theta,t)line} f(x,y)\mathrm{d}s = \iint_{\mathbb{R}^2} f(\boldsymbol{x})\delta(t - \boldsymbol{\xi} \cdot \boldsymbol{x})\mathrm{d}x\mathrm{d}y$$

$$= \int f(\boldsymbol{x})\delta(t - \boldsymbol{\xi} \cdot \boldsymbol{x})\mathrm{d}\boldsymbol{x} \tag{2.57}$$

where $\delta(x)$ is the Dirac delta function.

The Fourier transformation in the n dimension can be express as

$$F_n(\boldsymbol{x}) = \mathcal{F}_n[f(\boldsymbol{x})] = \int f(\boldsymbol{x})e^{-2\pi \boldsymbol{w} \cdot \boldsymbol{x}i}\mathrm{d}\boldsymbol{x} \tag{2.58}$$

where the period of $\boldsymbol{w}$ is 1, not 2π as in materials science conventionally.

$$\mathcal{F}_n[f(\boldsymbol{x})] = \int_{-\infty}^{\infty} \mathrm{d}p \int \mathrm{d}\boldsymbol{x} f(\boldsymbol{x}) e^{-2\pi pi}\delta(p - \boldsymbol{w} \cdot \boldsymbol{x}) \tag{2.59}$$

let $\boldsymbol{w} = t\boldsymbol{\xi}$, $p = ts$ ($t \in \mathbb{R}$, $\boldsymbol{\xi}$ is the unit vector in $\mathbb{R}^n$), then if note $\mathcal{R}$ as the operator of Radon transformation,

$$\mathcal{F}_n[f(\boldsymbol{x})] = |t| \int_{-\infty}^{\infty} \mathrm{d}s \int \mathrm{d}\boldsymbol{x} f(\boldsymbol{x})e^{-2\pi tsi}\delta(ts - t\boldsymbol{\xi} \cdot \boldsymbol{x})$$

$$= \int_{-\infty}^{\infty} \mathrm{d}s\, e^{-2\pi sti} \int \mathrm{d}\boldsymbol{x} f(\boldsymbol{x})\, \delta(t - \boldsymbol{\xi} \cdot \boldsymbol{x})$$

$$= \int_{-\infty}^{\infty} \mathcal{R}[f(t,\boldsymbol{\xi})]e^{-2\pi tsi}\mathrm{d}s. \tag{2.60}$$
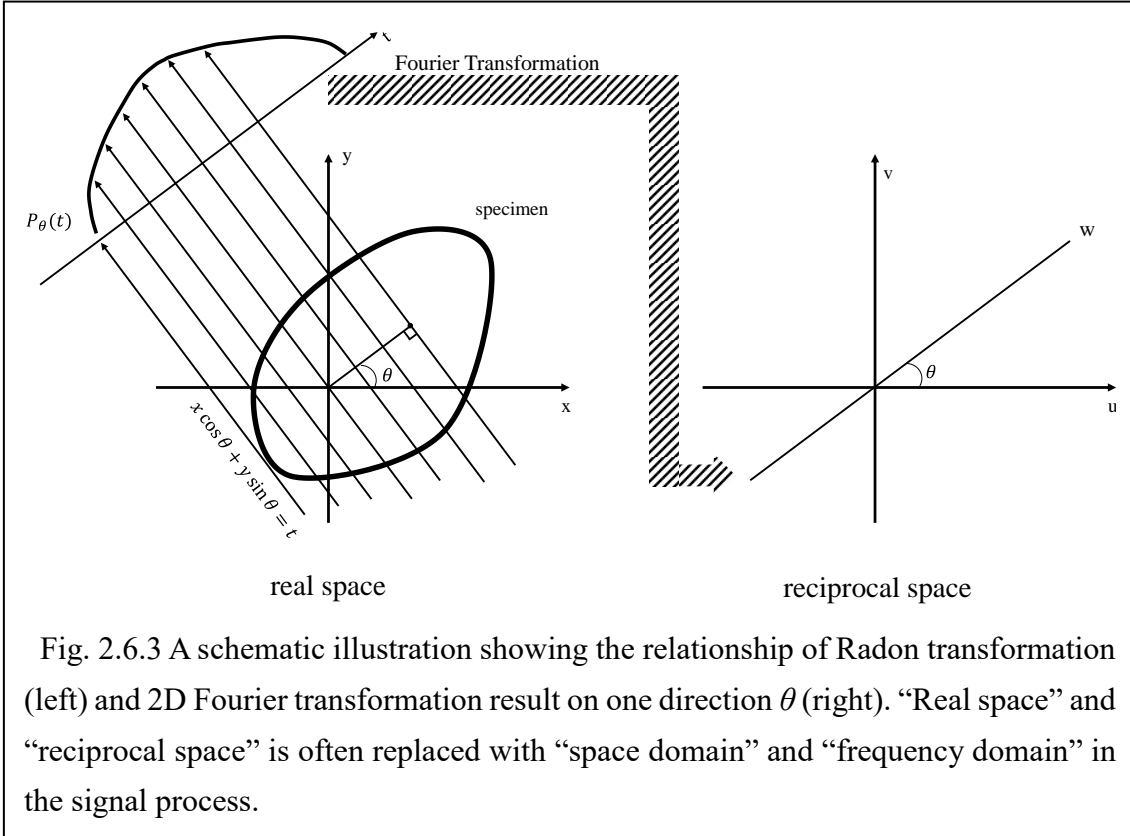
In other words,

$$\mathcal{F}_n[f(\boldsymbol{x})] = \mathcal{F}_1\big[\mathcal{R}[f(t,\boldsymbol{\xi})]\big]. \tag{2.61}$$

This indicates that the Fourier Transformation in the multiple dimension can be considered as the 1D Fourier transformation of a Radon transformation on one radial direction. Eq. (2.61) leads to the famous Projection-Slice Theorem in 2 dimensions:

$$\mathcal{F}_2[f(\boldsymbol{x})] = \mathcal{F}_1\big[\mathcal{R}_\theta[f(\boldsymbol{x})]\big] \tag{2.62}$$

Fig. 2.6.3 shows the nature of eq. (2.62), which is applicated in reconstruction method in Computed Tomography.

Fig. 2.6.3 A schematic illustration showing the relationship of Radon transformation (left) and 2D Fourier transformation result on one direction θ (right). "Real space" and "reciprocal space" is often replaced with "space domain" and "frequency domain" in the signal process.

2.6.3. The idea of filter in back-projection and FBP method

2.6.3.1. "Filter" in back-projection process

After the projected distribution was measured, the operation of a back-projection is the next and the final step in the tomographic process. Because the Fourier transformed result of Radon transformation can be regarded as the 2D transformed result of an object $f(x, y)$, as shown in eq. (2.62), the object function in 2D can be converted with a 2D inverse Fourier transformation:

$$f(\boldsymbol{x}) = \mathcal{F}_2^{-1}\left[\mathcal{F}_1[\mathcal{R}_\theta[f(\boldsymbol{x})]]\right]. \tag{2.63}$$

For simplicity, if only consider the 2D inverse Fourier transformation:

$$f(x, y) = \int_{-\infty}^{\infty}\int_{-\infty}^{\infty} F(u, v)e^{i2\pi(ux+vy)}\mathrm{d}u\mathrm{d}v \tag{2.64}$$

where (u, v) is a point in the reciprocal space (see Fig. 2.6.3)

$$\begin{cases} u = w\cos\theta \\ v = w\sin\theta \end{cases}. \tag{2.65}$$

In order to get close to the Radon transformation, the coordinate system from the

Cartesian coordinate system may change into the Polar coordinate system:

$$\mathrm{d}u\mathrm{d}v = w\mathrm{d}w\mathrm{d}\theta \tag{2.66}$$

then

$$f(x,y) = \int_0^{2\pi} \int_0^{\infty} F(w,\theta)e^{i2\pi w(x\cos\theta + y\sin\theta)}w\mathrm{d}w\mathrm{d}\theta \tag{2.67}$$

from the property of

$$F(w, \theta + 180°) = F(-w, \theta) \tag{2.68}$$

expression in eq. (2.67) can be converted into

$$f(x,y) = \int_0^{\pi} \left[\int_{-\infty}^{\infty} F(w,\theta)|w|e^{i2\pi wt}\mathrm{d}w \right] \mathrm{d}\theta \tag{2.69}$$

where $t = x\cos\theta + y\sin\theta = (2.52)$.

If to consider the projection distribution at the same angel θ, then eq. (2.69) in the 2D Fourier transformation can be changed into

$$f(x,y) = \int_0^{\pi} \left[\int_{-\infty}^{\infty} S_\theta(w)|w|e^{i2\pi wt}\mathrm{d}w \right] \mathrm{d}\theta$$

$$= \int_0^{\pi} Q_\theta(x\cos\theta + y\sin\theta)\mathrm{d}\theta \tag{2.70}$$

where

$$Q_\theta(t) = \int_{-\infty}^{\infty} S_\theta(w)|w|e^{i2\pi wt}\mathrm{d}w. \tag{2.71}$$

And $S_\theta(w)$ is the 1D Fourier transformation of the object along a straight line at an angle θ, i.e., the line w in the reciprocal space in Fig. 2.6.3, corresponding to the with line with t in the real space. This implies that eq. (2.70) is the Fourier Slice Theorem in 2D for one direction, or eq. (2.62) for one direction.

Since $S_\theta(w)$ is a function that θ is fixed, and w is identical to $\boldsymbol{w} = t\boldsymbol{\xi}$ in eq. (2.59) and (2.60),

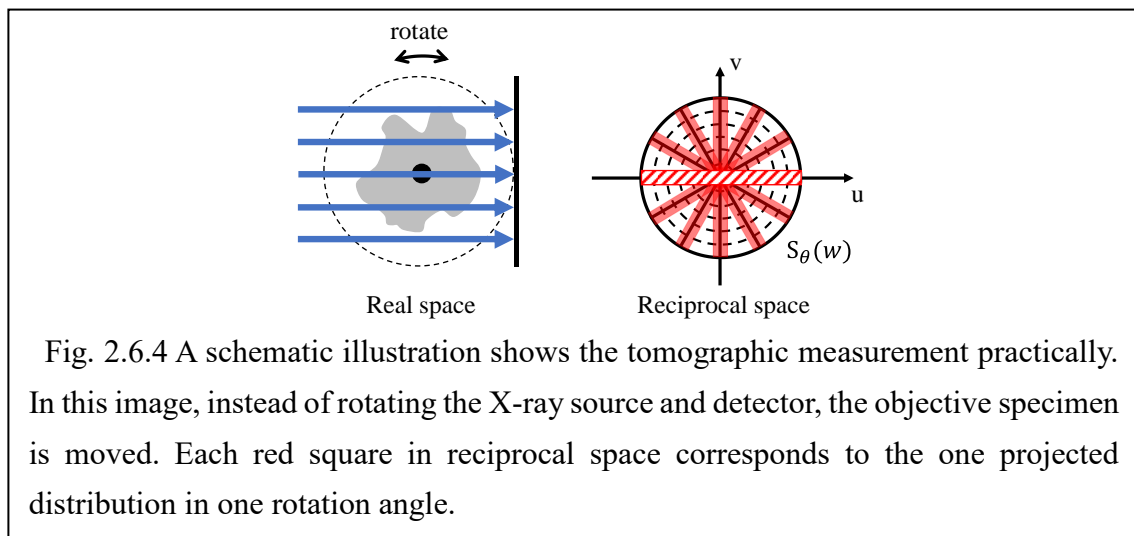$$S_\theta(w) = \mathcal{F}_1[\mathcal{R}_\theta[f(\boldsymbol{x})]] \tag{2.72}$$

Therefore, the back-projection process in eq. (2.70) consequently can be expressed as:

$$f(x,y) = \int_0^{\pi} \int_{-\infty}^{\infty} S_\theta(w)|w|e^{i2\pi\omega t}\mathrm{d}w\,\mathrm{d}\theta$$

$$= \mathcal{F}_2^{-1}[\mathcal{F}_1[\mathcal{R}_\theta[f(\boldsymbol{x})]] \cdot |w|] \tag{2.73}$$

Compared to eq. (2.62), there is an additional variable $|w|$ exists in the back-projected process in eq. (2.73). This can be regarded as a weighting factor, or the "filter". From this reason, $Q_\theta(t)$ was called a "filtered projection".

35

2.6.3.2. The necessity of a filter in the practical discrete system and the Filtered Back-Projection method

In the operation of computed tomography measurement, the resolution in the rotation angle and the pixel size of the reconstructed image is finite, particularly in this treatise. Therefore, when the projected distribution was converted into sinusoidal waves by a Fourier transformation, there are some restriction exist due to the discreteness, and which are needed to be considered carefully.

Fig. 2.6.4 A schematic illustration shows the tomographic measurement practically. In this image, instead of rotating the X-ray source and detector, the objective specimen is moved. Each red square in reciprocal space corresponds to the one projected distribution in one rotation angle.

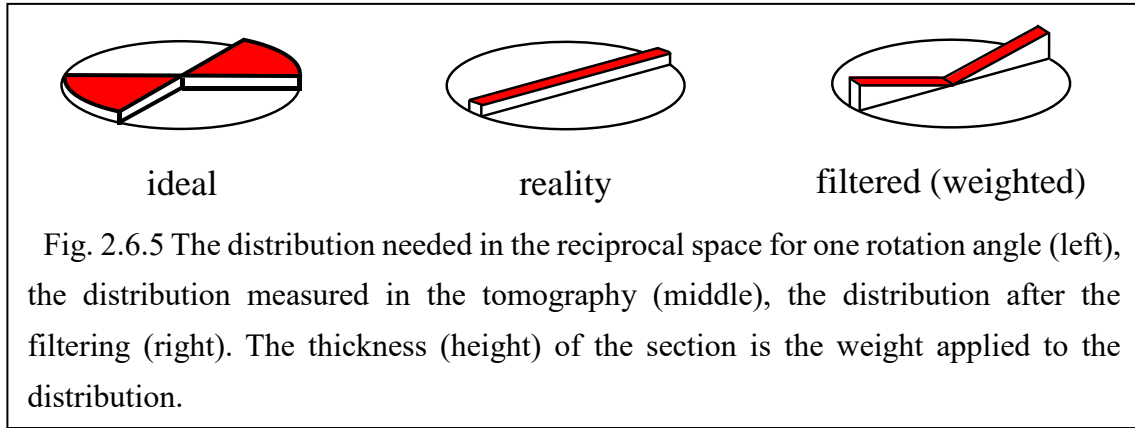### 2.6.3.2.1. The influence of Finite rotation step angles in the reciprocal space

Fig. 2.6.4 shows a schematic illustration of an example of tomography operated practically. It is obvious that the size of the rotation angle and the distance of different X-rays are both finite. This leads to the plots covering the reciprocal space is sparse in the high frequency domain, and also surplus in the low frequency domain at the same time. Therefore, the issue is how to treat this star-shaped plots into an evenly-distributed circle. Because every position in the reciprocal space represents a sinusoidal wave in the real space, every point in the reciprocal space has to be covered ideally. From this reason, a treatment on the measured reciprocal data is needed, and this data processing is usually conducted with weighting on reciprocal data, or also called the "filtering".

For a tomographic measurement with $M+1$ times of projections over an angle of 180°, i.e. with an angular step of 180°/M, then the weighting on each projection data, or the filter would be

$$\frac{2\pi|w|}{M}.$$
(2.74)

This is simply a coefficient multiplied with $|w|$ that needed in back-projection in the previous section 2.6.3.1, which can be regarded as a process to increase the "thickness" in each red shaded plot in the reciprocal space in shown as Fig. 2.6.4 respective to the frequency in each point in the reciprocal space. This is a compromise solution and different from what is needed, as shown in Fig. 2.6.5.

| ideal | reality | filtered (weighted) |

Fig. 2.6.5 The distribution needed in the reciprocal space for one rotation angle (left), the distribution measured in the tomography (middle), the distribution after the filtering (right). The thickness (height) of the section is the weight applied to the distribution.

Filters like Ramp filter mentioned in the section 2.6.2 is to manipulate the form of $|w|$. Hence, the Filtered Back-Projection is to simply switch the term $|w|$ with a filter in the eq. (2.71):

$$(71) = Q_\theta(t) = \int_{-\infty}^{\infty} S_\theta(w)|w|e^{i2\pi wt}dw$$

$$\approx \int_{-\infty}^{\infty} S_\theta(w) \cdot filter(|w|) \cdot e^{i2\pi wt}dw. \qquad (2.75)$$

2.6.3.2.2. The influence of Finite translation step size in the reciprocal space

For a distribution of discrete data with a finite spatial interval of τ, the highest frequency for Fourier transformation worthy of discussion is known as Nyquist rate which is $1/2\tau$ (Nyquist, H. 1928), indicating that the half period of the sinusoidal wave in the Fourier transformation cannot be shorter than the size of the spatial interval, or the size of a pixel in this treatise. Therefore, in the reciprocal space, the maximum radius of the circle would be $1/2\tau$ and the discussion is proceeded within this circle area.

Let w is the frequency on a direction in the Fourier transformation as eq. (2.59), and let W the maximum of w. The it would be as shown in Fig. 2.6.6:
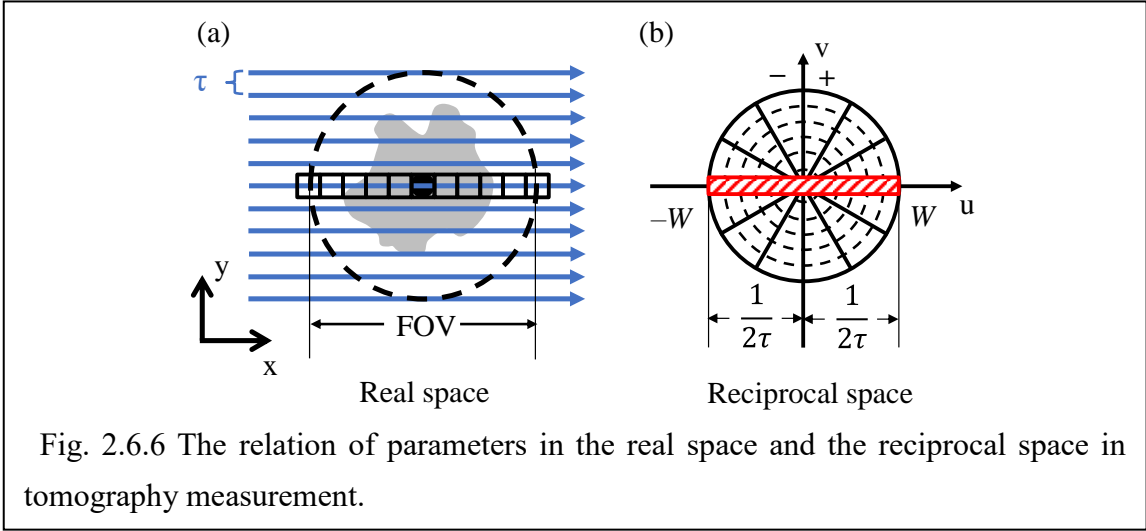
$$w_{max} = W = \frac{1}{2\tau} \qquad (2.76)$$

Fig. 2.6.6 The relation of parameters in the real space and the reciprocal space in tomography measurement.

the projected distribution is

$$P_\theta(m\tau) = \mathcal{R}_\theta[f(\boldsymbol{x})], \ \ m \in \left[-\frac{N}{2}, -\frac{N}{2}+1, \cdots, 0, \cdots \frac{N}{2}-1, \frac{N}{2}\right] \quad (2.77)$$

for a field of view (FOV) $= N\tau$ where a pixel by size $\tau \times \tau$ (N is a large number). m in here can be regarded as the coordinate of a point in the real space. Then the interval in the reciprocal space, or the frequency resolution in 1D discrete Fourier transformation (DFT):

$$\mathrm{d}w = w_{min} = \frac{1}{FOV} = \frac{1}{N\tau} = \frac{2W}{N} \quad (2.78)$$

Institute eq. (2.77) into (2.72):

$$S_\theta(w) = \mathcal{F}_1[P_\theta(m\tau)] \approx S\left(m\frac{2W}{N}\right)$$

$$= \frac{1}{2W} \sum_{k=-N/2}^{N/2} P_\theta\left(\frac{k}{2W}\right) e^{-j2\pi(mk/N)} \quad (2.79)$$

Instituting eq. (2.79) into (2.71),

$$Q_\theta(t) \approx \left(\frac{2W}{N}\right) \sum_{m=-N/2}^{N/2} S_\theta\left(m\frac{2W}{N}\right)\left|m\frac{2W}{N}\right| e^{-j2\pi m(2W/N)t}$$

$$Q_\theta(n\tau) = \left(\frac{2W}{N}\right) \sum_{m=-N/2}^{N/2} S_\theta\left(m\frac{2W}{N}\right)\left|m\frac{2W}{N}\right| e^{-j2\pi(mn/N)} \quad (2.80)$$

where t as shown in Fig. 2.6.1, which is the distance from projection line to rotation center, at a rotation angle θ.

Therefore, in the FPB method, if filters like Hamming filter is applicated on the reciprocal space, then eq. (2.71) is altered multiplied with the function of Hamming filter $H(w)$:

$$Q_\theta(n\tau) = \left(\frac{2W}{N}\right) \sum_{m=-N/2}^{N/2} S_\theta\left(m\frac{2W}{N}\right) \cdot \left|m\frac{2W}{N}\right| H\left(m\frac{2W}{N}\right) e^{-j2\pi(mn/N)} \qquad (2.81)$$

Comparing eq. (2.80) with the continuous $Q_\theta(t)$ in eq. (2.71), it is apparent that in the discrete system, the filter $\left|m\frac{2W}{N}\right|$ has to be operated on the projected distribution in the real space. The precision is higher when the discrete projection is close to the continuous one, i.e., $m\frac{2W}{N}$ is close to 0, or N is large, and m & τ is small. In other words, FBP is accurate when a small specimen is conducted with a high-resolution tomographic measurement, for both translational and angular movement. An obvious example showing the deviation between applying a filter to the continuous and the discrete system is that the exclusion of the "DC gain" in the continuous Fourier transformation system, which is mandatory in the discrete Fourier transformation system.

2.6.4. Convolution Back Projection method

Eq. (2.75) can be converted with the circular convolution denoted with ($\circ$), form the property of Fourier transformation

$$Q_\theta(n\tau) = \int_{-\infty}^{\infty} S_\theta(w) \cdot filter(|w|) \cdot e^{i2\pi wt} \mathrm{d}w$$

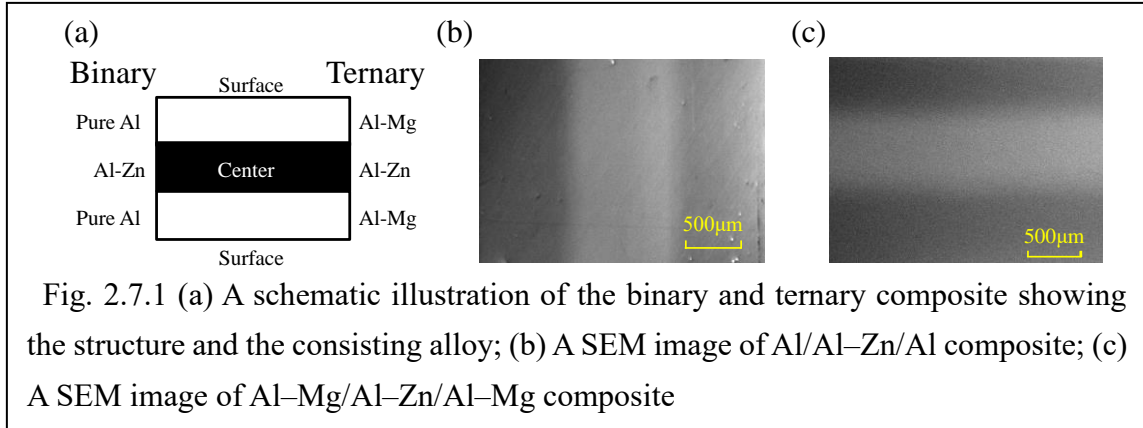$$\approx \tau P_\theta(n\tau) \circ \phi(k\tau) \qquad (2.82)$$

where $k, n \in [-N/2, -N/2 + 1, \cdots, 0, \cdots N/2 - 1, N/2]$, and $\phi(k\tau)$ is the inversed discrete Fourier transformation (IDFT) of the discrete function

$$\phi(k\tau) = \mathcal{F}^{-1}[filter(|w|)] \qquad (2.83)$$

Consequently, eq. (2.82) and (2.83) is what to be used, when a filter is applied on the Radon transformed distribution, especially when the measurement is coarse and discrete.

2.7. Specimen preparation

2.7.1. Al base specimen

Fig. 2.7.1 (a) A schematic illustration of the binary and ternary composite showing the structure and the consisting alloy; (b) A SEM image of Al/Al–Zn/Al composite; (c) A SEM image of Al–Mg/Al–Zn/Al–Mg composite

Two types of Al-based three-layered sandwich composite were studied in the 1D scanning microbeam SAXS measurement and tomographic measurement. Al/Al–Zn/Al multilayer is composed by the Al–Zn binary alloy, and Al–Mg/Al–Zn/Al–Mg multilayer is composed by Al–Zn–Mg ternary alloy. Table 2.7.1 and 2.7.2 shows the detailed chemical composition of each single layer in these composites. As shown in Fig. 2.7.1, a single layer Al–Zn located in the center of the composite, sandwiched by two layers of either pure Al or Al–Mg alloy. All the layers have a uniformed thickness. The production process is described as following:

Table 2.7.1 Chemical Compositions of single layer sheets in Al/Al–Zn/Al multi-layered composites

(mass%)

layers	Si	Fe	Cu	Mg	Zn	Ti	Al
Al	0.003	0.003	0.006	0.000	0.001	0.000	bal.
Al–Zn	0.005	0.003	0.005	0.000	14.07	–	bal.

Table 2.7.2 Chemical Compositions of single layer sheets in Al–Mg/Al–Zn/Al–Mg multi-layered composites

(mass%)

layers	Si	Fe	Cu	Mg	Zn	Ti	Al
Al–Mg	0.016	0.014	0.005	2.45	0.001	0.01	bal.
Al–Zn	0.014	0.017	0.005	0.00	10.16	0.01	bal.

2.7.1.1. Binary alloy composite

Al and Al–Zn alloy ingots were homogenized at 773 K and 723 K for 14.4 ks and air cooled. Then, both ingots were hot rolled into 2.5 mm at 673 K and followed by a cold rolling for a thickness of 2.0 mm. Finally, the cladding process was applied using hot rolling at 573 K, until the thickness reached 3 mm in total (approximately 1 mm for each layer). Before the cladding process, the attaching surfaces were polished by wire brushing to remove the oxides. Some of the composites were also performed a series of additional rolling process for reducing the thickness: a cold rolling was performed first and the thickness reduced into 1 mm thick, followed by a tempering for 3.6 ks and then air quenched. Finishing was conducted by a cold rolling until the thickness reached 0.5 mm. The 0.5 mm thick composite was used for 2D tomographic measurement for reducing the measuring duration.

2.7.1.2. Single layered binary specimen

A homogeneous Al–Mg alloy sheet with 12.9 mass% Mg were used as single layered specimens.

2.7.1.3. Ternary alloy composite

Before cladding, each layer was heated to 723 K for 14.4 ks for homogenization and then cooled with air. Hot rolling at a temperature of 673 K was conducted, reducing sheet thickness from 46 mm to 2.5 mm, followed by a cold rolling and the thickness reduced to 2 mm. After polishing the surface via wire buffing to remove the oxides, the three single layered metal sheets were combined and hot rolled into composites at 573 K, with a reduction in the thickness from 6 mm to 3 mm. Interdiffusion treatment was carried out at 673 K for 3.6 ks, then the composites were cooled in a furnace. A cold rolling as a final treatment was performed to reduce the thickness into 2 mm.

2.7.2. Heat Treatment

2.7.2.1. Heat treatment on Al–Zn binary composite

To conduct a detailed survey on the inhomogeneous distributions of the comprising elements in the composite, additional diffusion treatment was conducted to proceed the interdiffusion with a salt bath followed by an iced water quenching. After this heat treatment, the specimen was cut along the cross-section for 1 mm thickness.

The solid solution temperature of 773 K for binary composite was chosen within the range that is used by proceeding works (Osamura *et al.,* 1985; Okuda & Osamura, 1985), and it was confirmed that the vacancies were did not consumed too much during quenching process for binary alloy (Gerold & Merz, 1967), which affect the precipitation in the following process. This treatment was kept for 300 s in a vertical furnace, followed by a free fall into a cup of iced water for a distance of approximately 100 mm as fast water quenching. The air between the furnace and the iced water was kept at a room temperature. An artificial aging treatment was also performed in an oil bath for precipitation. Because Zn has a relatively high vapor pressure, the thickness of the specimen was reduced from 1 mm to 0.2 mm by a mechanical polishing on the roll direction (RD) direction, to remove surface layer and eliminate the possible Zn depleted area in specimen. Table 2.7.3 shows the multiple series of heat treatments conducted on the composites. Fig. 2.7.2 (a) and (b) shows the distribution of Zn concentration along the interdiffusion direction by Energy-dispersive X-ray spectroscopy (EDX).
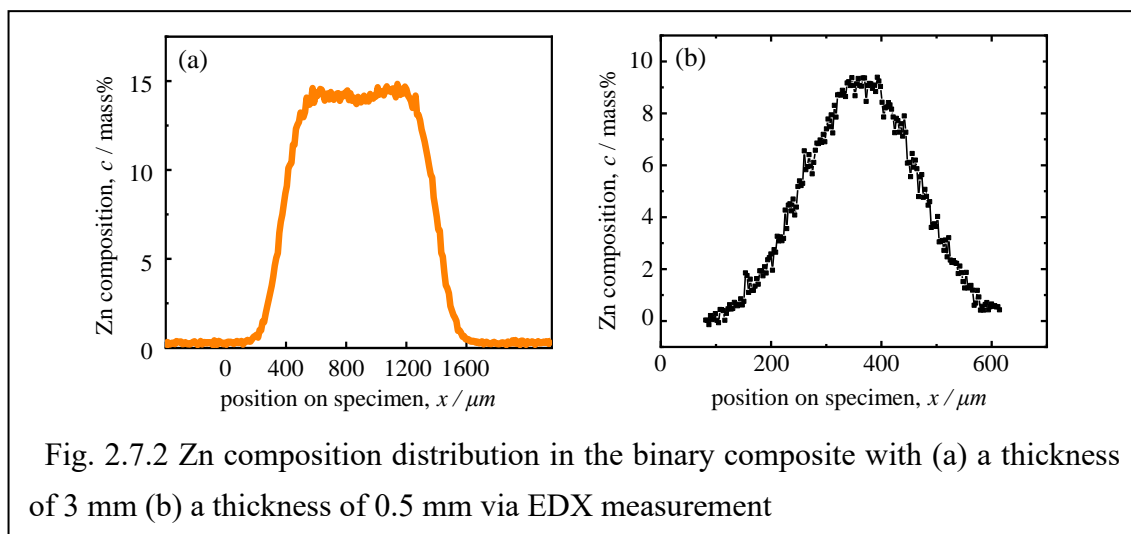

Fig. 2.7.2 Zn composition distribution in the binary composite with (a) a thickness of 3 mm (b) a thickness of 0.5 mm via EDX measurement

Table 2.7.3 Specimens and the heat treatment

Specimen	Diffusion Treatment	Solution Treatment and Aging
Al/Al–Zn/Al	773 K × 14.4 ks ➔ W.Q.	573 K × 300 s ➔ 313 K × 14.4ks ➔ W.Q.
Al/Al–Zn/Al	773 K × 14.4 ks ➔ W.Q.	598 K × 300 s ➔ 313 K × 14.4ks ➔ W.Q.
Al/Al–Zn/Al	773 K × 14.4 ks ➔ W.Q.	623 K × 300 s ➔ 313 K × 14.4ks ➔ W.Q.

2.7.2.2. Heat treatment on Al–Mg binary alloy

The specimens used in the ASAXS measurement are the Al–12.9 mass%Mg alloy. These alloys were put into a salt bath for a solid solution treatment for homogenization followed by an iced quenching, and then aged artificially in an oil bath. The detailed information of the heat treatment process is shown in the Table 2.7.4

Table 2.7.4 Specimens and the heat treatment

Specimen	Solution Treatment	Artificial Aging Treatment
Al–Mg	732 K × 3.6 ks ➔ W.Q.	313 k × 605 ks ➔ W.Q.
Al–Mg	773 K × 3.6 ks ➔ W.Q.	313 k × 1210 ks ➔ W.Q.

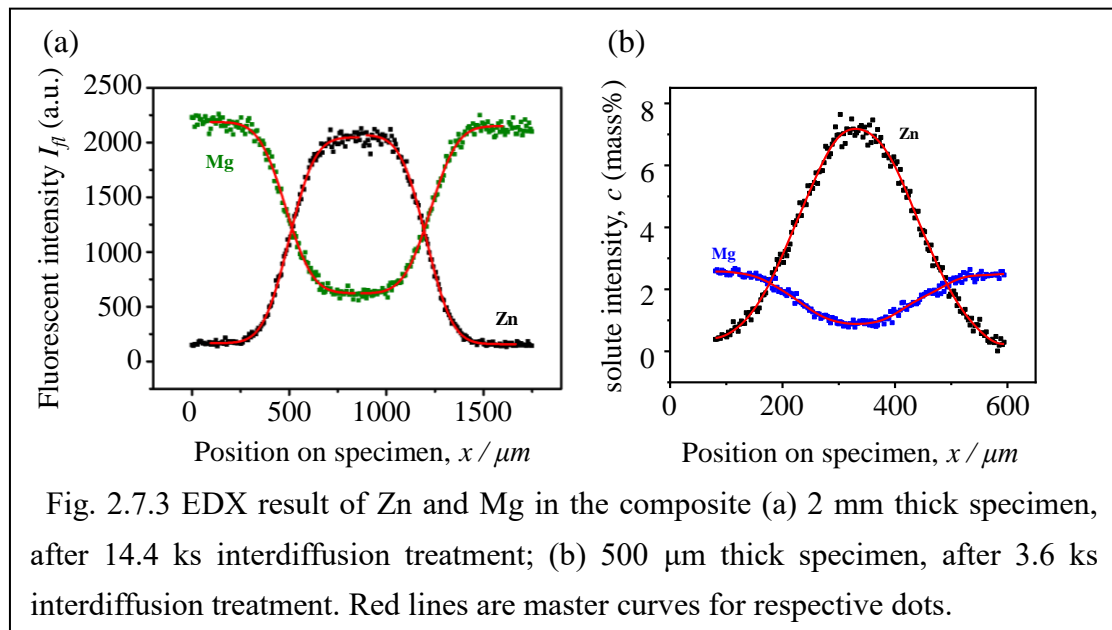### 2.7.2.3. Heat treatment on Al–Zn–Mg ternary composite

In order to control the width of the interdiffusion layers developed from the interfaces, interdiffusion processes were conducted by annealing the composites at a temperature of 793 K for 14.4 ks or 3.6 ks in a salt bath, then quenched into the iced water. Fig. 2.7.3 (a) and (b) shows the EDX result for Zn and Mg. Due to the low Mg concentration, fluorescent X-ray distribution was used to determine the solute distributions in the 2 mm thick composite, which used in the 1D SAXS scanning measurement shown as Fig. 2.7.3 (a). The EDX measurements were performed after annealing the ternary composite for 14.4 ks. The result shows that the solute concentrations, which represented by the fluorescent X-rays intensities, can be described by error functions. The interdiffusion layer thickness, determined based on the slope at the inflection point, have a value of approximately 2.5×10^2 μm and 4.8×10^2 μm for the 14.4 ks and 57.6 ks annealing respectively. From this result, the interdiffusion layer with a thickness of 8.9×10 μm was calculated to be formed during the cladding process before interdiffusion treatment. Specimens were aged at 393 K in a silicon oil bath for 300 s, 10.8 ks, and 345.6 ks, followed by iced water quenching.

For the tomography specimen with a thickness of 500 μm, the as-received ternary composite and Al–6.8 mol%Zn alloy were used as standard specimens to identify the absolute composition distribution. Same with 2 mm ternary composite, EDX measurement was conducted after the interdiffusion treatment in this specimen. The interdiffusion treatment was performed a shorter duration of 3.6 ks at 793 K in the salt bath. Fig. 2.7.3 (b) shows the EDX result of the concentration distribution. The maximum amount of Zn is lower than the 10.16 mass% for Zn, which implies that two interdiffusion layers have encountered and fused into a single layer with a thickness 500 μm approximately. The master curves for both elements were determined by filtered with a minimum 10 point-FFT filter as red lines.

Table 2.7.5 shows the multiple series of heat treatments conducted on the composites.

Table 2.7.5 Specimens and the heat treatment

Specimen	Interdiffusion Treatment	Solution Treatment and Aging
Al–Mg/Al–Zn/Al–Mg	793 K × 14.4 ks ➔ W.Q.	393 K × 300 s ➔ W.Q.
Al–Mg/Al–Zn/Al–Mg	793 K × 14.4 ks ➔ W.Q.	393 K × 10.8 ks ➔ W.Q.
Al–Mg/Al–Zn/Al–Mg	793 K × 14.4 ks ➔ W.Q.	393 K × 345.6 ks ➔ W.Q.
Al–Mg/Al–Zn/Al–Mg	793 K × 3.6 ks ➔ W.Q.	393 K × 1.2 ks ➔ W.Q.

Fig. 2.7.3 EDX result of Zn and Mg in the composite (a) 2 mm thick specimen, after 14.4 ks interdiffusion treatment; (b) 500 μm thick specimen, after 3.6 ks interdiffusion treatment. Red lines are master curves for respective dots.

2.8. Experimental set up

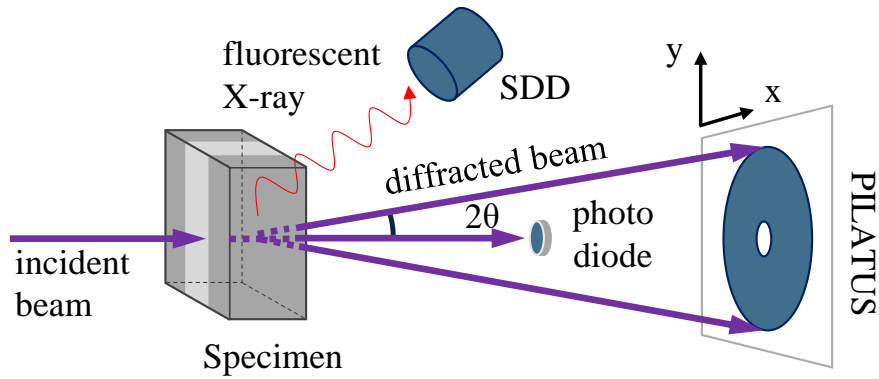## 2.8.1. Experimental set up for 1D microbeam SAXS scanning

Fig. 2.8.1 A schematic illustration of the SAXS measurement apparatus

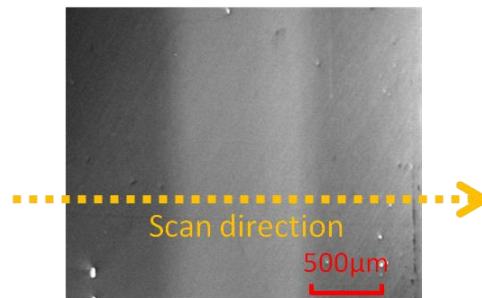Fig. 2.8.2 A photo of experiment apparatus in the experimental Hutch of BL40XU
in SPring-8

Fig. 2.8.3 A SEM image of the Al/Al–Zn/Al multilayered specimen and an
illustration of scanning process by microbeam X-ray

The quantitative analyses using scanning microbeam SAXS method was conducted on the multilayered composites. SAXS measurements were conducted at BL40XU (Inoue *et al.,* 2001) in Super Photon ring-8 GeV (SPring-8) in Hyogo prefecture, Japan. A high flux pencil beam X-ray with 5 µm in diameter and 15 keV in energy was used as incident beam. Beam was shaped with double pin hole system, with 5 or 10 µm in diameter for the first defining pin hole. The Scanning process was conducted by changing the irradiation position of the X-ray on a specimen by 5 µm or 10 µm after every measurement in the interdiffusion direction. The scattered X-ray intensity within a small angle was detected using a Pilatus 100K device from Dectris Ltd., which has a detection area of 8.38 mm × 33.5 mm, with a pixel size of 172 µm × 172 µm. The incident and transmitted X-ray was measured by the ion chamber and photo diode, respectively. In addition, Zn-*K* radiation was detected at the transmitted X-ray side using a silicon drift detector (SDD) simultaneously, shown in Fig. 2.8.1–2.8.3.

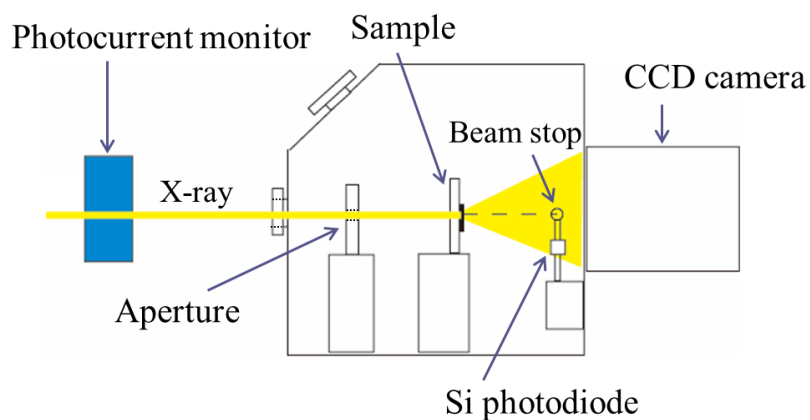## 2.8.2. Experimental set up for ASAXS measurement

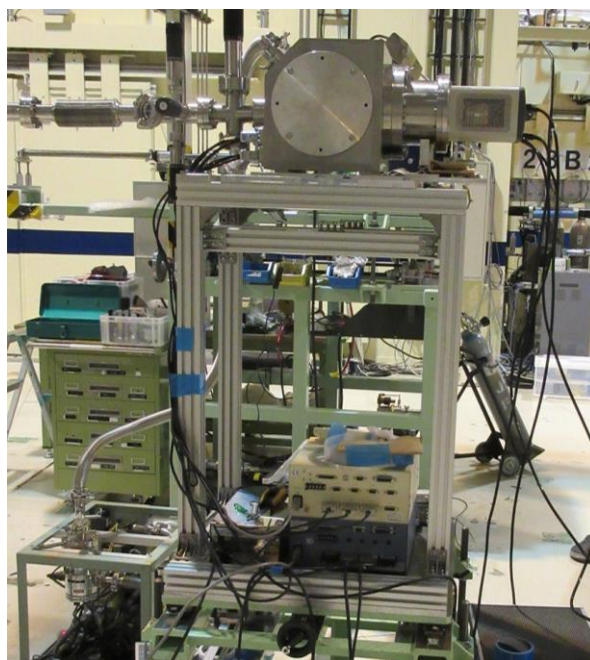Fig. 2.8.4 A schematic illustration of experimental apparatus used in ASAXS measurement.

Fig. 2.8.5 A photo of experiment apparatus in the experimental Hutch of BL27SU in SPring-8

The ASAXS measurements were conducted in BL27SU at SPring-8. The energy of the incident X-ray was adjusted to 1302 eV, compared to the absorption edge of $K\alpha$ in Mg which is 1305 eV. Fig. 2.8.4 shows a schematic illustration of experimental apparatus used in the ASAXS measurement. The inciden/transmitted X-ray was detected by a photoncurrent monitor, and a Si photodiode. The 2D SAXS intensity was measured by a CCD camera made for soft X-ray scattering intensity capturing: Back-thinned CCD Full-

47

Frame transfer CCD CCD42-40; couplinged with straight fibers in 1:1; and couplinged additionaly with tapered fiber in 2:1, which coated by sintillator material P43 (Gd_2O_2S:Tb) for 10 μm thickness. The apparatus was made by HAMAMATSU PHOTONICS K.K.

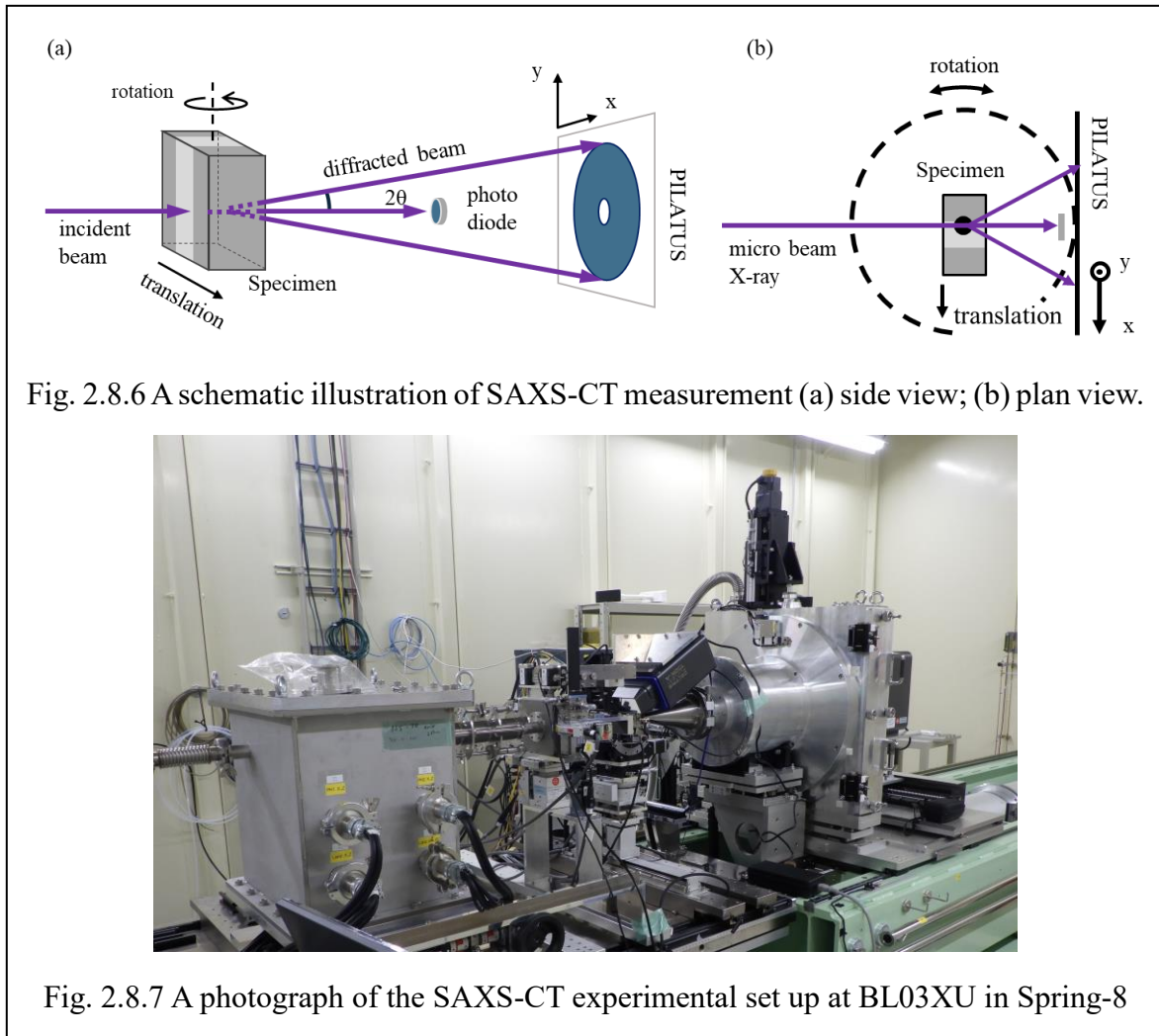### 2.8.3. Experimental set up of SAXS application in tomographic measurement

Fig. 2.8.6 A schematic illustration of SAXS-CT measurement (a) side view; (b) plan view.

Fig. 2.8.7 A photograph of the SAXS-CT experimental set up at BL03XU in Spring-8

Fig. 2.8.6 and 2.8.7 shows the schematic illustration and a photograph of the experimental set up in the tomographic measurement applied with SAXS method. The measurement was conducted with the operation of translation and rotation. The translation was performed the same manner with 1D scanning measurement in the section 2.8.1. The rotation operation was conducted on each scanning spot with a step of 3° in the rotation angle range of 0–180°. The tomographic measurements were conducted at both BL40XU (Inoue *et al.,* 2001) and BL03XU at Spring-8 (Masunaga *et al.,* 2011).

3. Nanostructure analysis of multilayered composites by Scanning microbeam SAXS

3.1. Simultaneous measurement of Fluorescent X-ray in microbeam scanning SAXS

3.1.1. Determining the distribution of local component in Al–Zn binary composite

EDX was applied before the SAXS measurement with an Electron Probe Micro Analyzer (EPMA) to evaluate the Zn concentration distribution of the specimens. In the Al–Zn binary composite, the interdiffusion layer was confirmed approximately 400 μm wide, as shown in the section 2.8.2.1 and Fig. 3.1.1 (a). With Zn fluorescent intensity was collected in microbeam scanning SAXS measurement (Fig. 3.1.1 (a) thin line), the Zn composition was determined by comparing the intensity distribution result from EDX (Fig. 3.1.1 (a) thick line).

During the aging at 313 K, G. P. zones forms initially under a common metastable miscibility gap as shown in Fig. 3.1.1 (b), whose volume fraction $V_f(c)$ and the average size $R(c)$ strongly depend on the composition c.
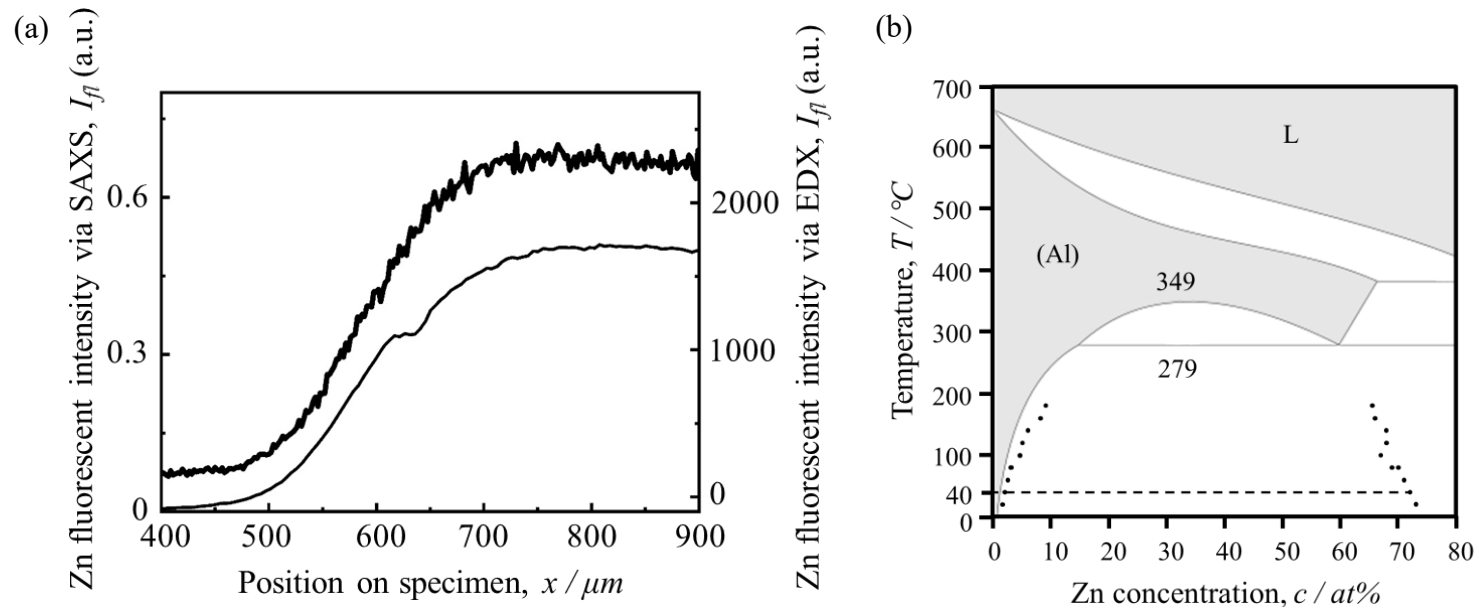
Fig. 3.1.1 (a) Thin line: the measured Zn fluorescent intensity by the microbeam SAXS scanning measurement. Thick line: EDX result of Zn fluorescent intensity; (b) Al–Zn binary phase diagram with metastable miscibility gap (black dots). Dashed line indicates the unstable phase separation at 313 K (see Löffler, 1995)

50

3.1.2. Determining the distribution of local component in Al–Zn–Mg ternary composite

Al and Mg is low in fluorescent X-ray energy, which is 1.43894 keV & 1.21154 keV respectively (Hubbell, 1982; Hubbell & Seltzer, 1996). This indicates that neither of the intensities is measurable in air. Zn, however, the absorption edge in vicinity of the K shell having an energy of 9.65860 keV. This feature of Zn making which the only solute for the ternary composite Al–Mg/Al–Zn/Al–Mg to be identified in air. and can be used as a tracer for identifying the local composition in the SAXS scanning measurement.

In the binary alloy Al–Zn with the distribution of Zn atoms, the local composition distribution of both Al and Zn is uniquely determined. But for a ternary alloy, the composite distribution is unknown without an additional information e.g. the relationship of the distribution of Mg and Zn (or Al and Zn) atoms.

After the mentioned in the section 2.8.2.2, a pair of master curves for the composition distribution of Zn and Mg were determined by using curves defined by error functions fit on the acquired fluorescent intensity distribution by EDX measurement. The composition distribution of resulted master curves for Zn and Mn was mapped on a calculated equilibrium Al–Mg–Zn ternary phase diagram via the CALculation of PHAse Diagrams (CALPHAD) method (Kaufman, & Bernstein, 1970) displayed as Fig. 3.1.2.
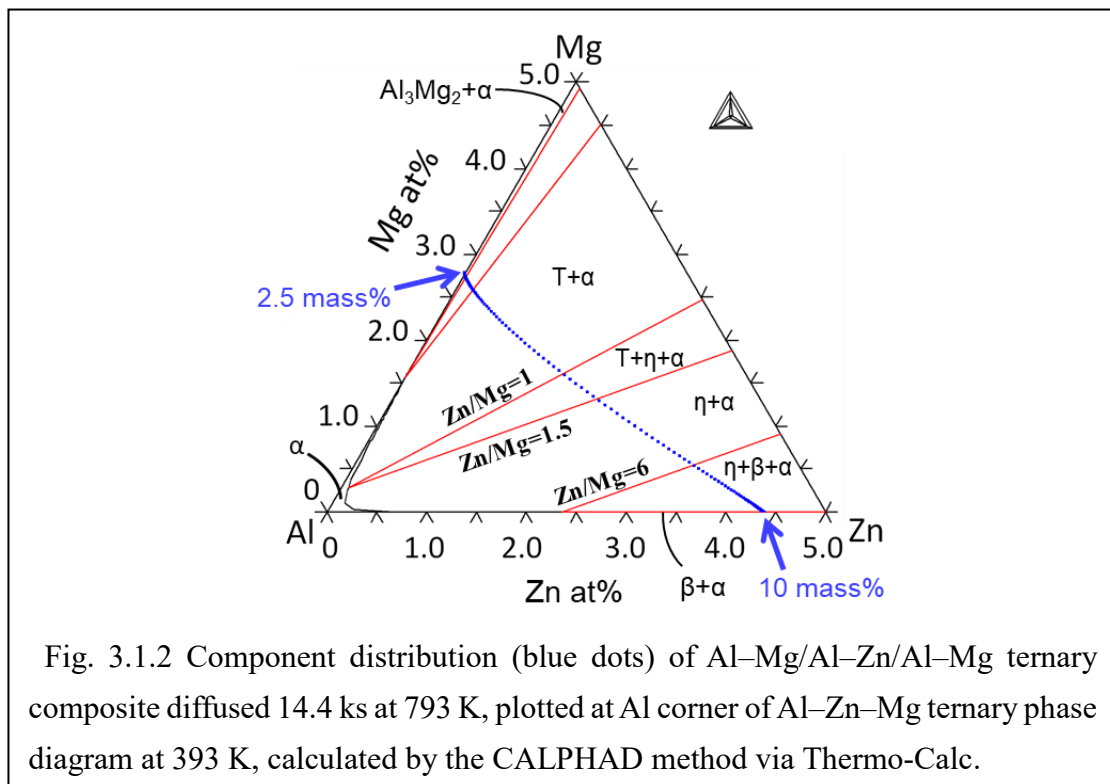

Fig. 3.1.2 Component distribution (blue dots) of Al–Mg/Al–Zn/Al–Mg ternary composite diffused 14.4 ks at 793 K, plotted at Al corner of Al–Zn–Mg ternary phase diagram at 393 K, calculated by the CALPHAD method via Thermo-Calc.

3.2. 2D SAXS profiles in Al–Zn binary composite

Fig. 3.2.1 SAXS patterns at different positions of Al/Al–Zn/Al binary composite after solid treatment at 598 K
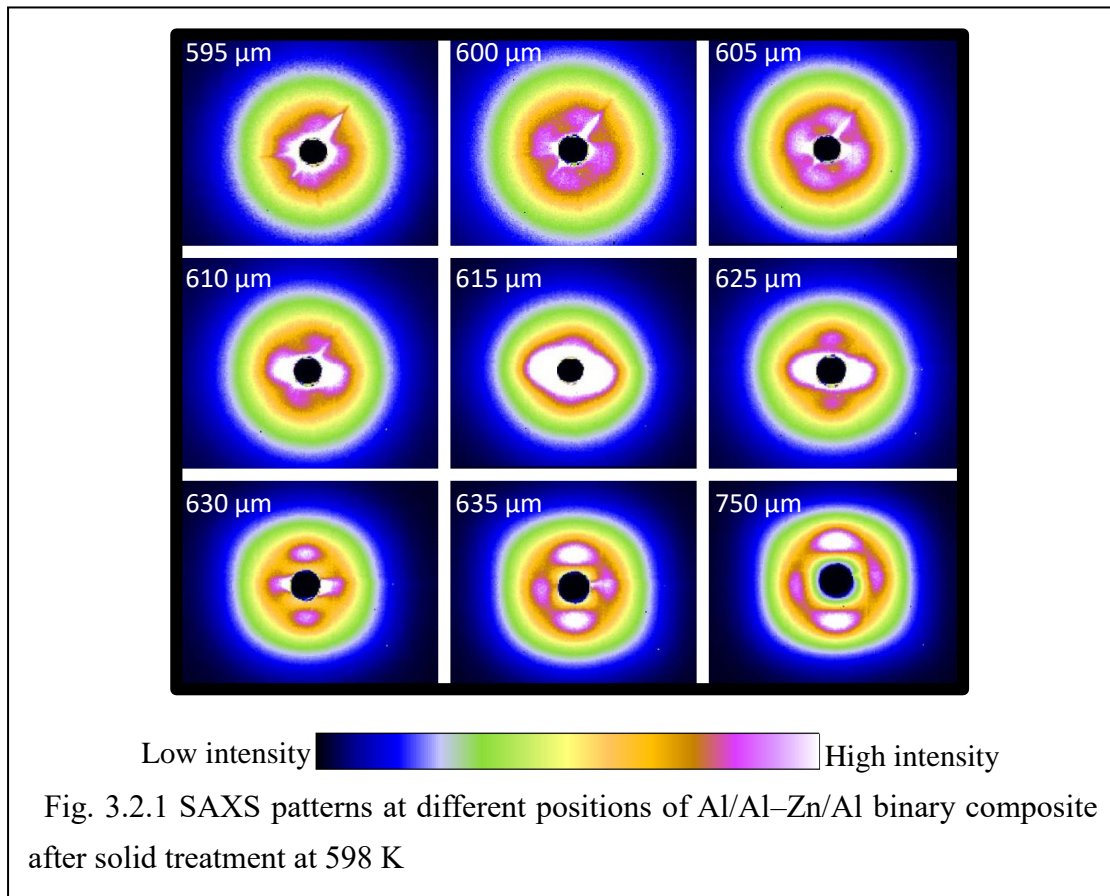
Fig. 3.2.1 shows a series of 2D SAXS profiles scattered from an interdiffusion layer of the 598 K solution treated Al/Al–Zn/Al composite. With position proceeds, Zn density increases in these images. It is known that the spherical G. P. zones initially precipitates in the Al–Zn alloys around this composition (Gerold, 1961; Hennion, *et al.*, 1982). This can be confirmed in the resulted 2D pattern before and after 610–625 μm on specimen, which are analogous to the scattered patterns induced by the spherical G. P. zones (Hennion *et al.,* 1982). In the position of 605–630 μm, apart from the intense 2-folded symmetric pattern in the center, the directions of the 4-folded symmetric patterns from spherical G. P. zones alter with the position of specimen, indicating that the interfering directions of G. P. zones area changed by moving the spotting position on the specimen. This implies that the direction of the matrix alters in these positions. In other words, in the scanning position of 605–630 μm, two different grains are measured.

In the same area of 605–630 μm position, an intense ellipsoidal 2-folded symmetric pattern in the center can be observed. This ellipsoidal pattern observed only in the interface position of the Al/Al–Zn interdiffusion area, and the elongation direction is the

same as the interdiffusion direction. With all above, it is natural to consider the scatterer of the ellipsoidal scattered patterns as Al oxides which are sandwiched by the Al alloys which can be oxidized easily in air.

3.3. Precipitate parameters from SAXS in Al–Zn binary composite
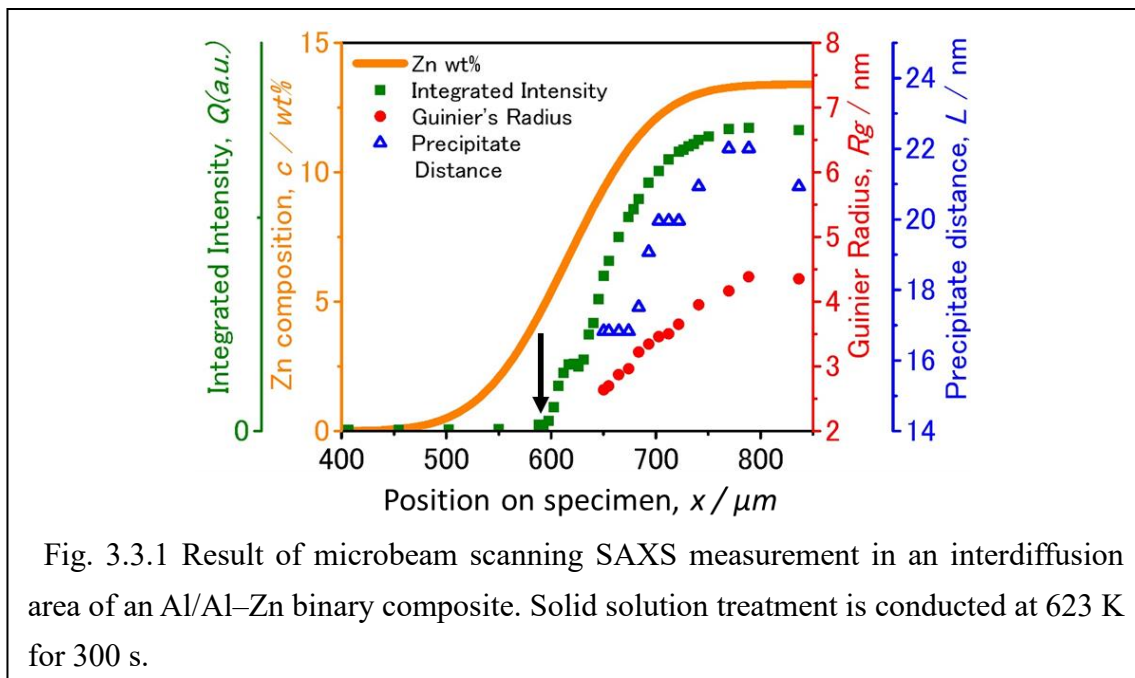

Fig. 3.3.1 Result of microbeam scanning SAXS measurement in an interdiffusion area of an Al/Al–Zn binary composite. Solid solution treatment is conducted at 623 K for 300 s.

Fig. 3.3.1 shows the result of the SAXS scanning measurement. These plots are calculated based on the radial averaged profile of 2D SAXS profiles. The integrated intensity Q in relative unit, Guinier radius R_g, and if the interference between precipitates was observed, the mean precipitation distance L was calculated from the SAXS profiles (Guinier & Fournet, 1955). The integrated intensity Q was calibrated with specimen thickness in each spotted local area calculated with the transmittance and the concentration of Zn. From the specimen location that the integrated intensity Q start to be obvious, G. P. zones was detected at 5.17 mass% in Zn. This value is slightly higher compared to 4.71 mass% reported by Popović et al (1992). The distribution of nanostructures is different from the classical nucleation theory, in which the critical radius decreases with an increment in concentration. However, this result is consistent with the report by Osamura *et al.* (1985), which demonstrated the deviation from nucleation theory with considering the difference in the speed of grain growth.

Letcher and Schmidt (1966) showed that the radius distribution of non-interacting assemblies made by spherical particles can be evaluated using functions below:

53

$$\rho(r) = \frac{1}{\pi^3 \delta^2 r^2} \int_0^{\infty} dq [q^4 F^2(q) - C] \alpha(qr)$$
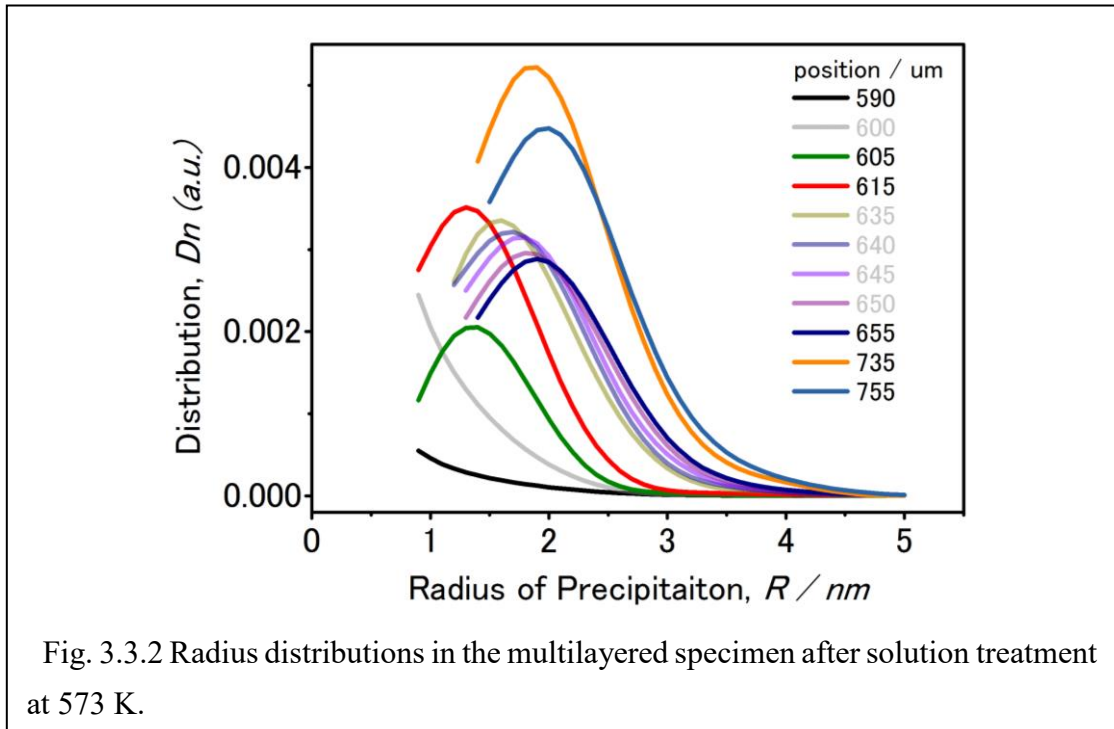
where

$$\alpha(qr) = \left[\cos qr \left(1 - \frac{8}{q^2 r^2} \right) - \frac{4 \sin(qr)}{qr} \left(1 - \frac{2}{q^2 r^2} \right) \right],$$

$$C = \lim_{q \to \infty} q^4 F^2(q) . \tag{3.1}$$

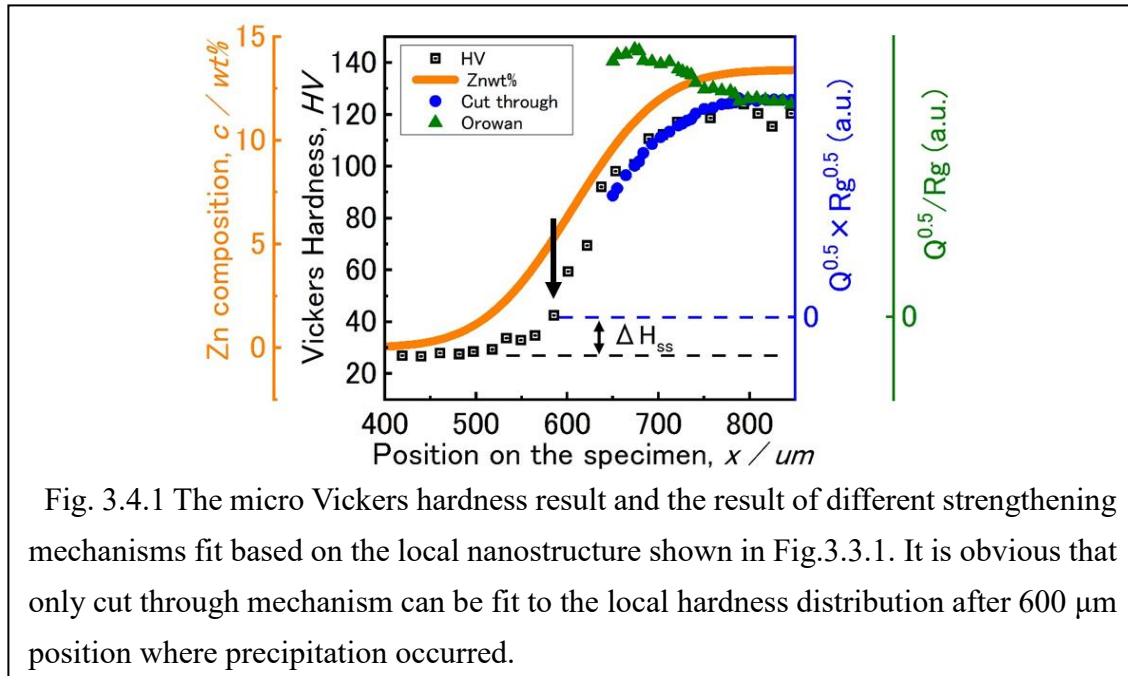$F(q)$ is the scattered wave function; δ is the difference in the electron density of the sphere and the matrix; r is the radius of the sphere; q is the length of the scattering vector. Fig. 3.3.2 shows the size distribution of each point on the specimen solution treated at 573 K. With the increment in Zn concentration, the change in the size distribution in Fig. 3.3.2 can be summarized into two parts:

1. Peak positions on the distribution curves shift into the large radius direction with lowering the summit.

2. Distributions keep the same shape, but the amplitude increase.

This property was also found in the 623 K solution treated specimen.

Fig. 3.3.2 Radius distributions in the multilayered specimen after solution treatment at 573 K.

3.4. Relationship between local structure and local hardness in Al–Zn binary composite

Fig. 3.4.1 The micro Vickers hardness result and the result of different strengthening mechanisms fit based on the local nanostructure shown in Fig.3.3.1. It is obvious that only cut through mechanism can be fit to the local hardness distribution after 600 μm position where precipitation occurred.

The local hardness distribution was measured with Vickers tests on the Al–Zn binary composite, as shown in Fig. 3.4.1 for an interdiffusion area Al/Al–Zn. The relative integrated intensity Q in Fig. 3.3.1 indicates that there is no precipitate found in the position x < 600 μm on specimen, but the local hardness distribution H_V in Fig. 3.4.1 shows a slight increase with the increment in Zn concentration. This can be attributed to the solid solution strengthening.

For the position x > 600 μm on the specimen, the relative integrated intensity Q in Fig. 3.3.1 increases appreciably, which indicates the increment in the volume fraction of precipitates. Therefore, the hardness detected for position x > 600 μm can be regarded as the summation of the solid strengthening and precipitation strengthening effect. Also as mentioned in the 3.1.1, phase separation shares a common miscibility gap indicating the hardness which induced by solid solution is constant when G. P. zones are precipitated, with a value of H_V right before precipitation occurs. This value is noted as ΔH_{ss} in the figure, corresponding to the solid solution strengthening by the Zn atoms at the solubility limit.

It is well-known that the precipitation strengthening mechanism (Gerold, 1979) shifts from a cut-through mechanism to an Orowan mechanism depending on the stress required for deformation. This can be determined respectively by using

55

$$\tau \approx 3\mu|\varepsilon|^{\frac{2}{3}}\sqrt{\frac{RV_f}{b}} \propto \sqrt{RV_f} \tag{3.2}$$

$$\tau = \frac{0.8}{bR}\sqrt{\frac{3V_f}{2\pi}} \propto \frac{1}{R}\sqrt{V_f} \tag{3.3}$$

where τ is the critical resolved shear stress (CRSS), ε the lattice constant difference between the precipitate and the matrix, μ the shear modulus, R and V_f the average radius and the volume fraction of precipitate respectively. According to eq. (2.24) in the section 2.2.1.2.2:

$$V_f = \frac{Q}{2\pi^2\Delta\rho^2} \tag{3.4}$$

indicating $Q \propto V_f$. Q is the integrated intensity, $\Delta\rho$ the electron density difference between the G. P. zones and matrix. Considering that the SAXS measurement has been conducted on the specimen in every 5 μm, this can be rewritten as a function of the position on the specimen $Q(x) \propto V_f(x)$ within the concerning area with a uniformed electron density difference.

Guinier radius R_g is also evaluated as a function of position on specimen $R_g(x)$. In every SAXS measurement, the detected $R_g(x)$ is an averaged value of all illuminated precipitates. V_f and R in eq. (3.2) and (3.3) can be replaced with $Q(x)$ and $R_g(x)$ within the precipitation area. Fig. 3.4.1 shows the local hardness estimated with nanostructure result in Fig. 3.3.1 and eq. (3.2) and (3.3) for either of the strengthening mechanism. The estimated strength distribution which follows the Orowan mechanism showed a significant deviation from the measured Vickers hardness distribution, whereas the one follows the cut-through mechanism showed an agreement with the experimental local hardness distribution. This indicates that the Al/Al–Zn interdiffusion area of the multilayered composite is strengthened with the cut-through mechanism, and it is still underaged.

In a conventional investigation, V_f is constant and τ alters with the changing in R. In this experiment, however, the solute composition is changed when moving the measuring position. For this Al–Zn composite, the whole concerning area on specimen—which is identical to the precipitation area—shares a common phase transformation. This made it plausible for to use the same value of μ, b, ε for eq. (3.2) and (3.3) for all nanostructure, regardless of the fluctuation in the volume fraction and the mean radius.

3.5. 2D SAXS profile in Al–Zn–Mg ternary composite

2D SAXS patterns in the Al–Mg/Al–Zn/Al–Zn composites were almost isotropic, as shown in Fig. 3.5.1 (a). Therefore, the nanostructural distribution was estimated mainly after taking an average on azimuthal direction. Porod's law (Guinier & Fournet, 1955; Brumberger, 1956) was confirmed in the radial averaged SAXS profile shown as Fig. 3.5.1. (b), indicating the precipitates have sharp edges (Guinier & Fournet, 1955; Glatter & Kratky, 1982). No efficient intensity was observed in either of the edge areas of specimen, where Mg is the main solute in the Al alloy.

Fig. 3.5.1 (a) An example of 2D SAXS pattern; (b) the radial averaged SAXS profile plotted with scattering vector.
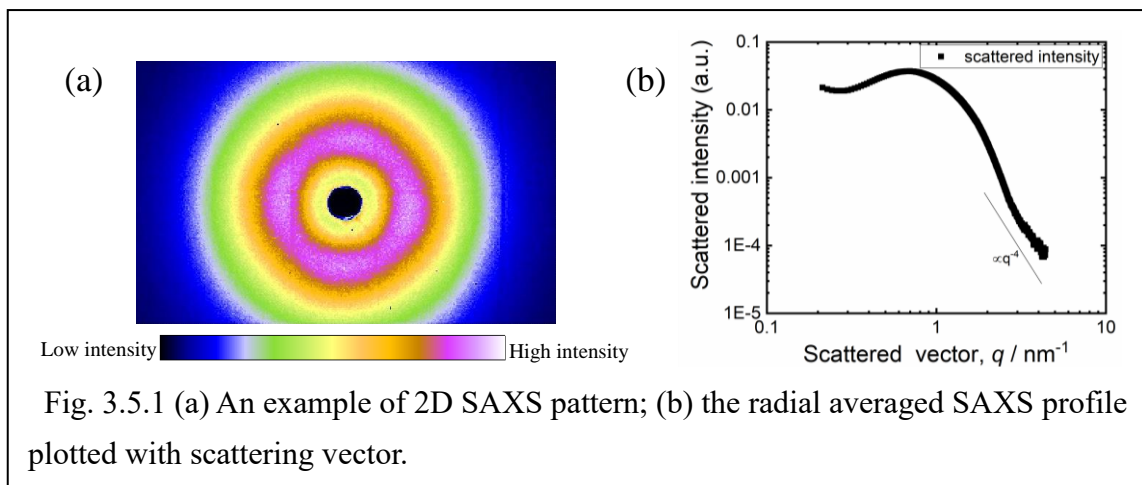
3.6. Component distribution and precipitates in Al–Zn–Mg ternary composite

Fig. 3.6.1 shows the stable Al–Zn–Mg ternary phase diagram at 393 K, calculated by the CALPHAD method, with the concentration distribution of multilayered Al–Mg/Al–Zn/Al–Mg composite, both have shown in the section 3.1.2 as Fig. 3.1.2. As mentioned in the section 1.2.3, this phase diagram, or the composite, or in detail, the interdiffusion layers of the composite can be divided into several regions based on the atomic ratio of Zn/Mg which divides the phase separation. According to Fig. 3.6.1, the μ phase precipitates as a stable precipitate when Zn/Mg > 1; the T phase does not exist when Zn/Mg > 1.5; and when Zn/Mg > 6, the stable precipitate of β phase appears. The miscibility line between two phase transformation of $\eta + \beta + \alpha$ and $\beta + \alpha$ is not observable quantitatively in this phase diagram.

As mentioned in the section 3.1.2, throughout the ternary composite, local composition distribution plotted with blue dots, transverse different stable phase triangles and tie-lines. This indicates that unlike the case of the binary alloy composite, that the whole precipitated area shares a common tie-line, different phase separations may occur in this

ternary composite, respect to the local position and its local Zn/Mg ratio. This leads to the difference in all the types of the precipitated nanostructure; the electron density difference of the precipitates and the matrix; the volume fraction of each precipitates; the mean size of each precipitates due to the solute composition in the local area, or the position on the specimen.
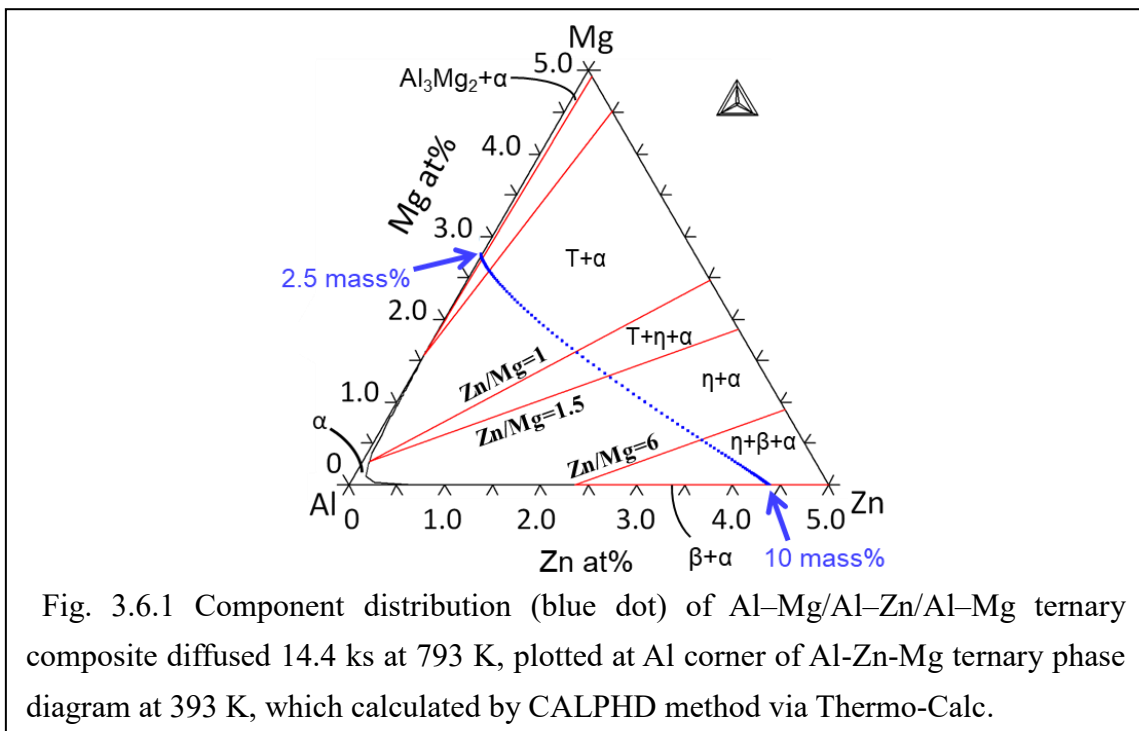

Fig. 3.6.1 Component distribution (blue dot) of Al–Mg/Al–Zn/Al–Mg ternary composite diffused 14.4 ks at 793 K, plotted at Al corner of Al-Zn-Mg ternary phase diagram at 393 K, which calculated by CALPHD method via Thermo-Calc.

3.7. Precipitation parameters obtained from SAXS in Al–Zn–Mg ternary composite

Two composites were measured for microbeam SAXS scanning measurement after underwent the aging process for 300 s and 10.8 ks. Fig. 3.7.1 shows the SAXS result of the interdiffusion area in the composites, which is the relative integrated intensity Q; Guinier radius R_g; and the mean distance of precipitates L for either of the composites using the same method for the binary alloy. Q, R_g, and L all roughly increased with the Zn concentration in the composite aged for 300 s. However, for the composite underwent an aged for 10.8 ks, Q decreased with the increment in the Zn concentration from approximately 700 μm position on specimen. Other two parameters showed the same tendency with the structure with a shorter ageing time.

The relative scattered intensity $I(q)$ and Q are affected by both of the $\Delta\rho$ and the anisotropy of the precipitates (section 2.2.1.2.1 and 2.2.1.2.4). Anisotropy can be evaluated qualitatively from 2D SAXS patterns to check if the scatterers are exceedingly anisotropic. As shown in Fig. 3.5.1. (a), the detected 2D SAXS patterns were isotropic in both of the composites. This implies that the precipitates are in the spherical shape. Therefore, anisotropy was ignored in this discussion.
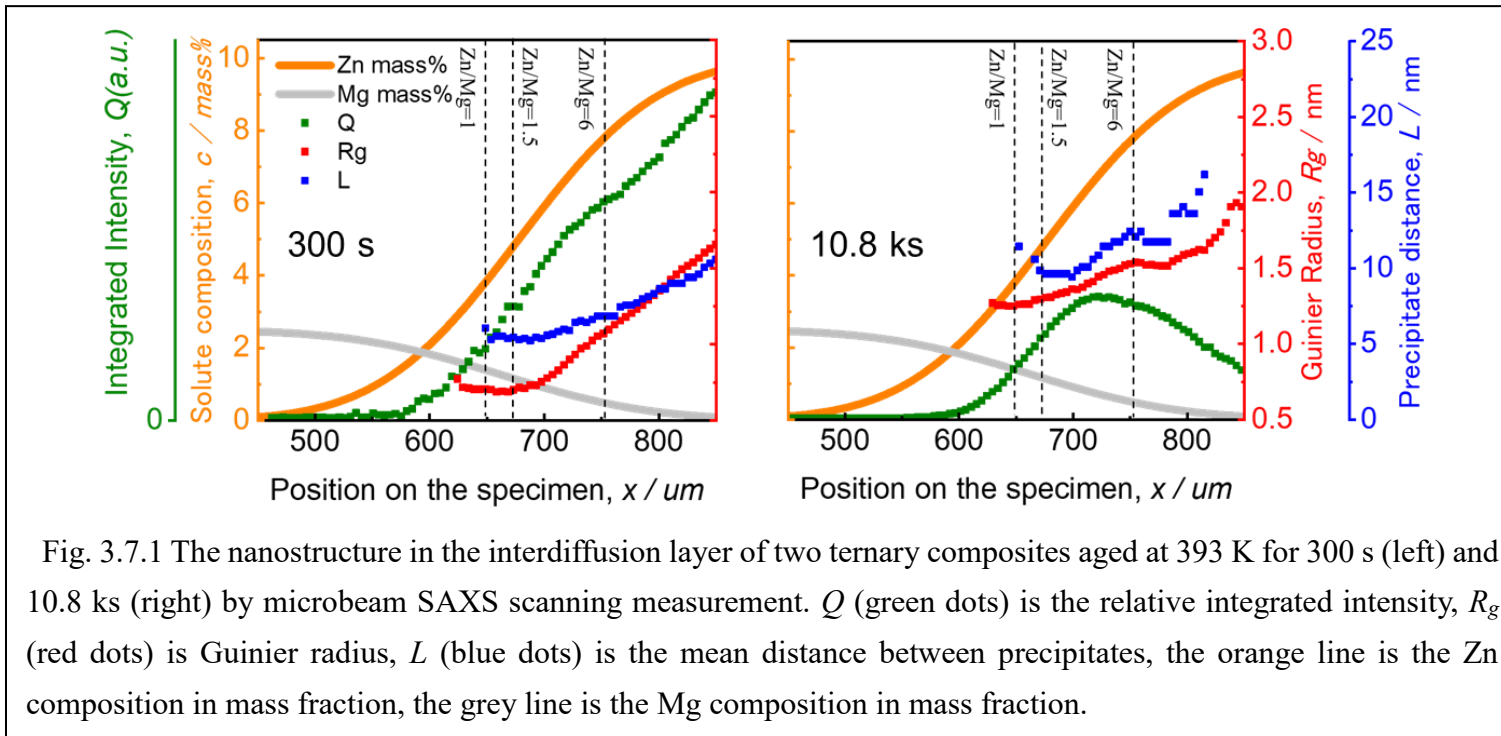
Fig. 3.7.1 The nanostructure in the interdiffusion layer of two ternary composites aged at 393 K for 300 s (left) and 10.8 ks (right) by microbeam SAXS scanning measurement. Q (green dots) is the relative integrated intensity, R_g (red dots) is Guinier radius, L (blue dots) is the mean distance between precipitates, the orange line is the Zn composition in mass fraction, the grey line is the Mg composition in mass fraction.

The difference in electron density between the precipitates and matrix $\Delta\rho$ affects $I(q)$ and Q with a squared form (section 2.2.1.2.4). Therefore, in the position where multiple types of precipitates coexist, $\Delta\rho$ was estimated as the average value for all precipitates in the Fig. 3.7.1. Al_3Mg_2 was not observed from SAXS measurement, due to the reason that in the periodic table, Al and Mg locates in the same period and even next to each other, $\Delta\rho$ is negligible for detection. This can be confirmed from that no appreciable SAXS intensity was observed in the edge region of specimen that corresponding to the Al–Mg alloy mentioned in the section 3.5. The measured precipitates are therefore only T, η, and β for the stable phase and the corresponding metastable precursors. Therefore, the concerned area corresponding to the position after 570 μm in Fig. 3.7.1.

Fig. 3.7.2 The volume fraction (monochromatic dots) and the electron density difference (colored dots) on the ternary composite aged at 393 K for 300 s (solid dots) and 10.8 ks (hollow dots).
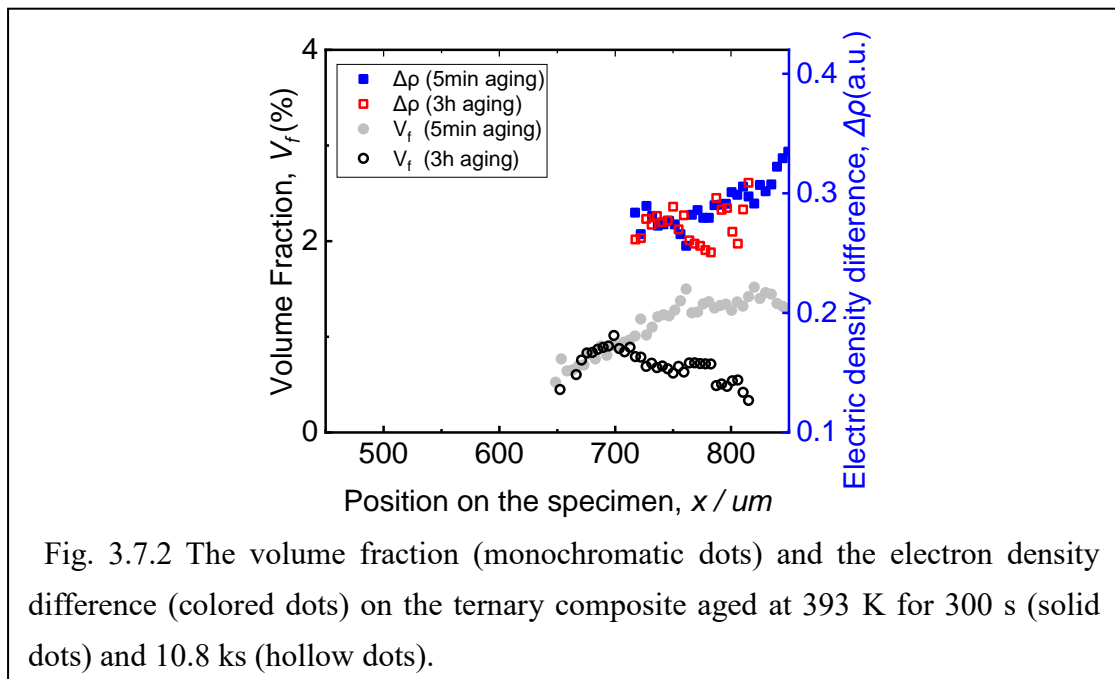
Fig. 3.7.2 shows the volume fraction V_f and $\Delta\rho$ calculated from SAXS parameters in Fig. 3.7.1 and eq. (3.4) in section 3.4. V_f slightly showed an increment between 650 μm and 700 μm, and decreased after 700 μm on the specimen. Adachi et al. (1999) showed a similar tendency while traversing the same stable phase area of $\alpha + T + \eta/\alpha + \eta$ and $\alpha + T$ aged at 393K for 108 ks, but they did not provide an adequate result. The $\Delta\rho$ plots also showed a decrement into 89% at a maximum, between the nanostructure of specimen which aged for 300 s and 10.8 ks at the position of 782 μm. This value is close to the difference of which between G. P. zone/α and η'/α reported by Adachi et al. (1999) as 84 %. In addition, the result of $\Delta\rho$ and the Zn concentration distribution in the 300 s aged specimen approximately showed a linear relationship. This can be explained

based on the G. P. zone miscibility gap calculated by Adachi et al. (1999). $\Delta\rho$ was not calculated before in the position of 700 μm on the specimen, due to the insufficient data in Q.

3.8. Relationship between local nanostructure and local hardness: Al-Zn-Mg ternary composite

Fig. 3.8.1 shows the Vickers hardness distribution H_V detected on the composites locally underwent the aging of 300 s and 10.8 ks. The H_V distribution with a different aging time both showed a same tendency. From a position approximately 620 μm on the specimen, H_V increase with Zn/Mg ratio from 56 HV; between the position 700 μm and 800 μm, both showed the peak hardness with 111 HV (300 s) and 104 HV (10.8 ks) and started to decrease with increasing Zn/Mg. The local hardness increased with the annealing time between 520 μm and 720 μm, and decreased after 720 μm on the specimen. The hardness at 720 μm is both 95 HV for the composites.

Fig. 3.8.1 Local hardness distribution in the 300 s and 10.8 ks aged ternary composite, in the interdiffusion area. The Mg distribution curve is omitted.
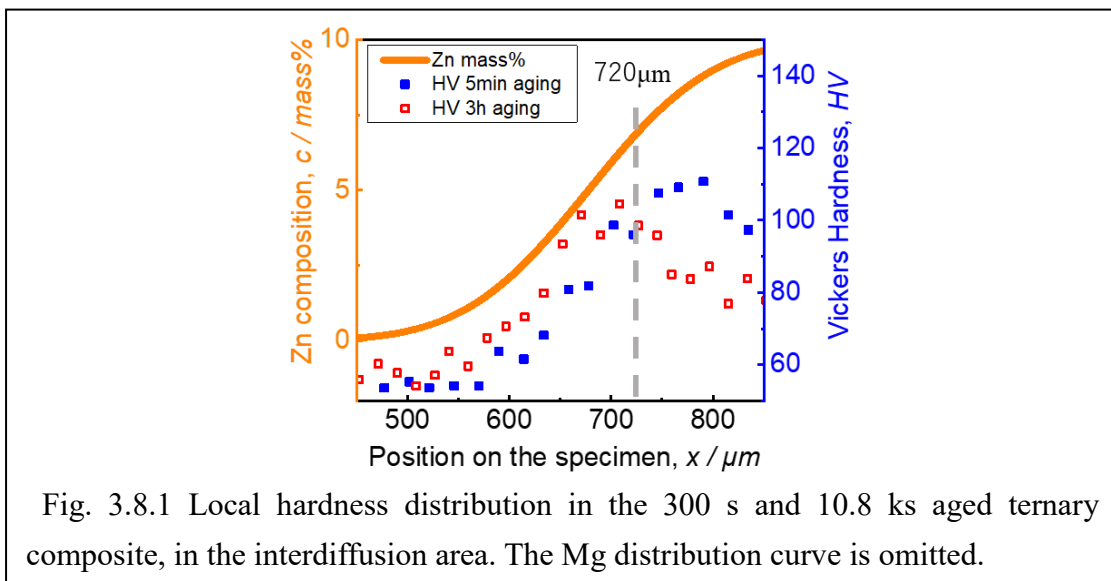
Fig. 3.8.2 shows the relationship between the detected local hardness distributions and the estimated hardness with nanostructural distributions shown as Fig. 3.7.1, using different strengthening mechanisms like section 3.4 for the binary composite. The plots of $V_f^{0.5} R_g^{0.5}$ and $1/L$ corresponding to the cut-through mechanism and the Orowan mechanism in (3.2) and (3.3) respectively. Estimated hardness distributions were multiplied by a common constant for each strengthen mechanism in 300 s and 10.8 ks aged specimens like in section 3.4. The plot of $V_f^{0.5}/R_g^{0.5}$ was similar to that of $1/L$, indicating the validity of V_f. L was converted into (3.3) by volume fraction V_f and R_g

treated as the mean radius of isotropic scatterers. A common coherent strain for the cut-through mechanism and a common shear modulus for the Orowan mechanism are assumed for all of the plots. Before 570 μm on the specimen, the local hardness did not change from 56 HV. In this area, the value in Q is practically 0, indicating the composition of Zn is extremely low, and Al–Mg alloy with a low Mg concentration is known that can only be strengthened by either the solid solution or the work hardening (Adachi *et al.,* 1999). Moreover, this composite is free from work hardening. This information indicates that the strength increment from the solid solution in this material is low. Therefore, the effect of the fluctuation of solid solution was ignored, and the hardness of 54 HV was determined as the solid solution strengthening effect in this composite.

For the 300 s aged specimen, the estimated plots following cut-through mechanism can only be adjusted in the area within 650–790 μm; the estimated plots following the Orowan mechanism can be adjusted in the area beyond 766 μm. Therefore, the detected local hardness H_V within the area 766–790 μm can be explained by using either of the mechanisms.

For the 10.8 ks aged specimen, both of the mechanisms area able to be fitted roughly to the entire detected local hardness H_V distribution, and in the area 708–834 μm, the estimated plots by the mechanisms is trivial in difference.

It can be concluded that for the 300 s aged composite, nanostructure before 766μm is underaged and which after 790 μm is overaged. For the 10.8 ks aged composite, the structure after 720 μm is overaged.
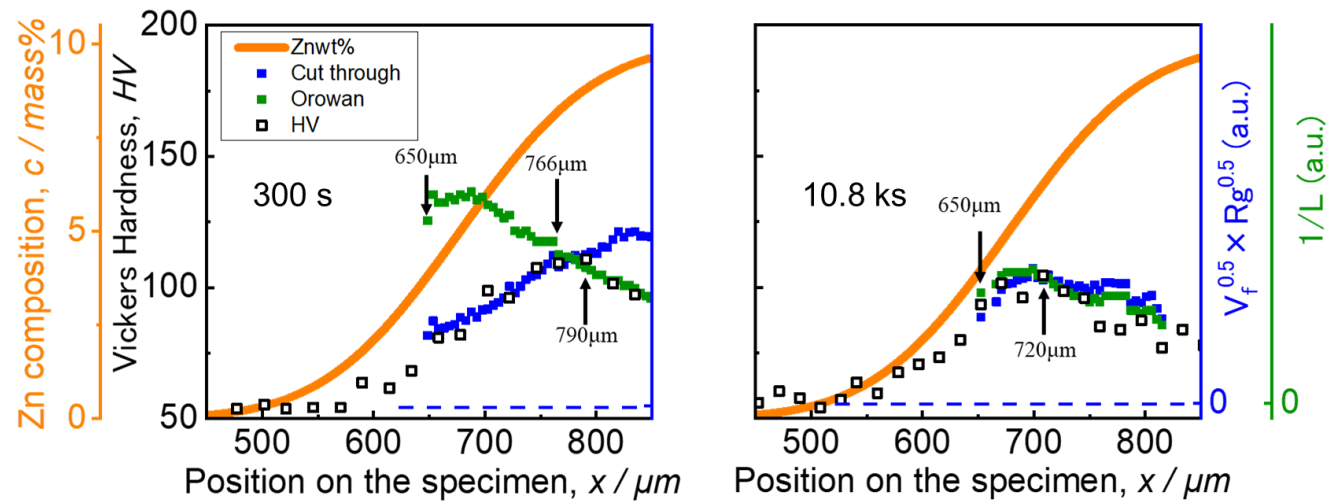
Fig. 3.8.2 Estimated results by different strengthening mechanisms on the specimens after aged at 393 K for 300 s and 10.8 ks. The distribution curve of Mg is omitted for conciseness.

3.9. Identification of local precipitates in Al–Zn–Mg ternary composite

As mentioned in the section 3.6, only T, η, β stable phase and the related metastable precipitates (Berg *et al.,* 2001) can be detected using X-ray. Since the metastable phases are predominant in strengthening (Lendvai, 1996), only the T, η, β stable phase and the related metastable precipitates are needed to be considered.

In the specimen area where Zn/Mg < 1 in molar ratio, where the structure separates into stable phases α + T in the area x < 650 μm, the local hardness in Fig. 3.8.1 increased with the annealing time. Due to the insufficient information derived from SAXS measurement which shown in Fig. 3.7.1, it is unable to identify the nanostructure from the stable T phase or its precursors. (Suzuki *et al.,* 1973; Fukui *et al.,* 1975; Yang *et al.,* 2014)

In the area of 1–1.5 in Zn/Mg molar ratio, where the structure separates into stable phases α + T + η in 650–670 μm, Li *et al.* (2017) have shown that the phase segregation is faster in an alloy which has a higher Zn/Mg ratio. Moreover, based on the work of Kovács et al. (1980) and Maloney et al. (1999) the precipitates are considered to be G. P. zone or the early stage of η′, as nanostructures for 300 s and 10.8 ks aged specimen in this area were isotropic and underaged. The increment in the local hardness with aging proceeds observed in 650–670 μm in Fig. 3.8.1 could be caused by either the coarsening of the G. P. zones, or the transformation from G. P. zones into η′ phase. This is from the reason that η′ strengthens Al–Mg–Zn alloys the most (Kovács *et al.,* 1980; Park & Ardell, 1983; Osamura *et al.,* 1984; Lendvai, 1996).

In the area of 1.5–6 in Zn/Mg molar ratio, where the nanostructure separates into stable phases α + η in 670–700 μm, considered to be coexisting G. P. zones and η′ phase, according to that the η′ phase strengthens the material the most, and the discussions about underaging and overaging in the section 3.8.

The last area of Zn/Mg > 6 is where nanostructure separates into stable phases α + β in x > 700 μm, which is also the area that Mg is diluted. Therefore, the nanostructure is analogous to the Al–Zn binary alloy in this area. For Al–Zn alloy, the phase separation of β phase at 393 K is known as:

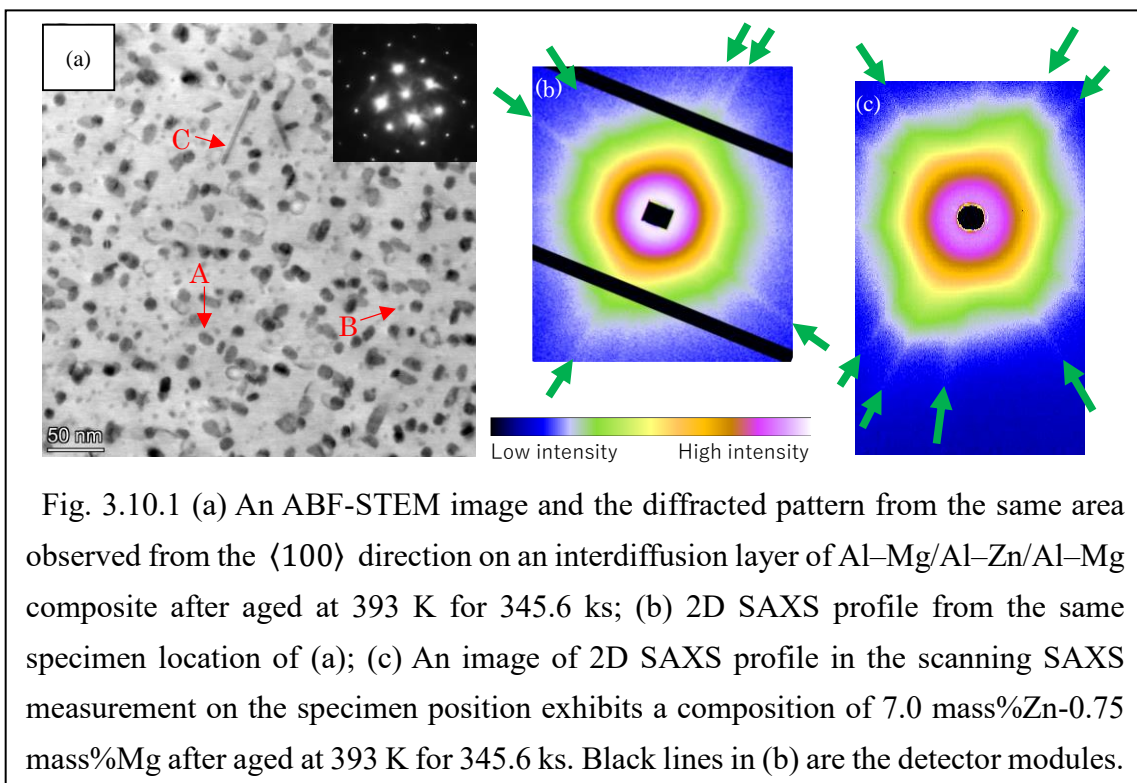*Solid Solution $\rightarrow$ G. P. zone (sphere) $\rightarrow$ G. P. zone (ellipsoidal) $\rightarrow$ α'_R $\rightarrow$ β (see Löffler, 1995)*

Since the spherical and the ellipsoidal G. P. zone are extremely sensitive to the quenching speed (Gerold & Merz, 1967), and also no anisotropic pattern was observed in the 2D SAXS images, the precipitates would be the sub-micrometer sized α'_R, which is not

observable by SAXS measurement. This is considered to be the reason of the decrement in V_f and Q with a proceeded aging time, as shown in Fig. 3.7.1 and Fig. 3.7.2.

3.10. Anisotropy observation via TEM and SAXS profile

It is known that both η′ and η have a variety of shapes. Therefore, the radial averaged 1D profiles converted from 2D scattered intensities may not accurately reflect the dimensions of the anisotropic precipitates. This leads to the discrepancies between the true values and the measured values of R_g and V_f without knowing the 3D shape of the scatterers. Fig 3.10.1 (c) shows an example of 2D scattered SAXS pattern which shows anisotropy during a microbeam SAXS scanning measurement in the Photon Factory (PF) in Ibaraki, Japan. This pattern was observed on the specimen aged at 393 K and for a longer period of 345.6 ks, at the position on the specimen where having a concentration of 7.0 mass%Zn and 0.75 mass%Mg. The nanostructure separates into stable phases η + α in this concentration, according to the ternary phase diagram showed on Fig. 3.6.1.

Fig. 3.10.1 (a) An ABF-STEM image and the diffracted pattern from the same area observed from the ⟨100⟩ direction on an interdiffusion layer of Al–Mg/Al–Zn/Al–Mg composite after aged at 393 K for 345.6 ks; (b) 2D SAXS profile from the same specimen location of (a); (c) An image of 2D SAXS profile in the scanning SAXS measurement on the specimen position exhibits a composition of 7.0 mass%Zn-0.75 mass%Mg after aged at 393 K for 345.6 ks. Black lines in (b) are the detector modules.

The anisotropy observed in the 2D SAXS pattern during scanning SAXS measurement can roughly be divided into 2 types, i.e. the streaks which are weak and thin, which denoted with green arrows; and a strong polygonal pattern. In order to examine the origin of these anisotropies, a TEM observation was conducted with a specimen underwent the

same heat treatment of 393 K for 345.6 ks. A 2D SAXS measurement was also performed after the TEM observation on this specimen. Both measurements conducted on TEM specimen had the same projection direction with the one shown as Fig. 3.10.1 (c). Fig 3.10.1 (a) shows the Angular Bright-Field Scanning Transmission Electron Microscopy (ABF-STEM) image and its diffracted pattern observed in ⟨100⟩ projection. In this image, three types of precipitates can be observed by their shapes: η′ phase denoted as A, G. P. zone as B, and η phase as C, according to the report by S. Jacumasso *et al.* (2016).

Fig. 3.10.1 (b) shows the 2D SAXS pattern scattered from the TEM specimen by an X-ray projected from the same ⟨100⟩ orientation as the TEM image. This SAXS pattern exhibits the same features observed in the Fig. 3.10.1. (c), namely, a strong polygonal shape with multiple weak streaks denoted with green arrows. This can be interpreted by the combination of the three shaped precipitates observed in TEM image in Fig. 3.10.1. (a): a large isotropic pattern scattered from the small spherical B; the pattern of oblate shapes scattered from the oblate-shaped A; the small amount of long rod-shaped C scattered into thin discs, and were cut into thin streaks by the Ewald sphere. Therefore, the 2D scattered pattern was confirmed which is scattered by η′/η and G. P. zones.

4. Anomalous small angle X-ray scattering method (ASAXS) in Al–Mg alloy

4.1. Anomalous small angle X-ray scattering method

Anomalous small angle X-ray scattering (ASAXS) is an application of SAXS by adjusting the incident X-ray energy to a certain value which is in the vicinity of the absorption edge of the object element. In Al-Mg alloy, as mentioned in the section 1.2.2, it is difficult for the ordinary SAXS method to conduct a valid investigation due to the weak contrast of electron density in the matrix and the Mg-rich precipitates. The absorption edge of K shell in Al and Mg atom is 1.560 KeV and 1.305 KeV respectively (Hubbell 1982; Hubbell & Seltzer, 1996), which made it possible to select an energy at either of the edges to increase the perceived electron density $\Delta\rho$. This made the scattered intensity strong enough by distinguishing the Mg-rich and the Mg-poor matrix after the segregation. This method was successfully applied on Al–6.7 mol% Zn alloy for the first time by our group in 2016 (Okuda *et al.,* 2016) in which used the K absorption edge of Al.
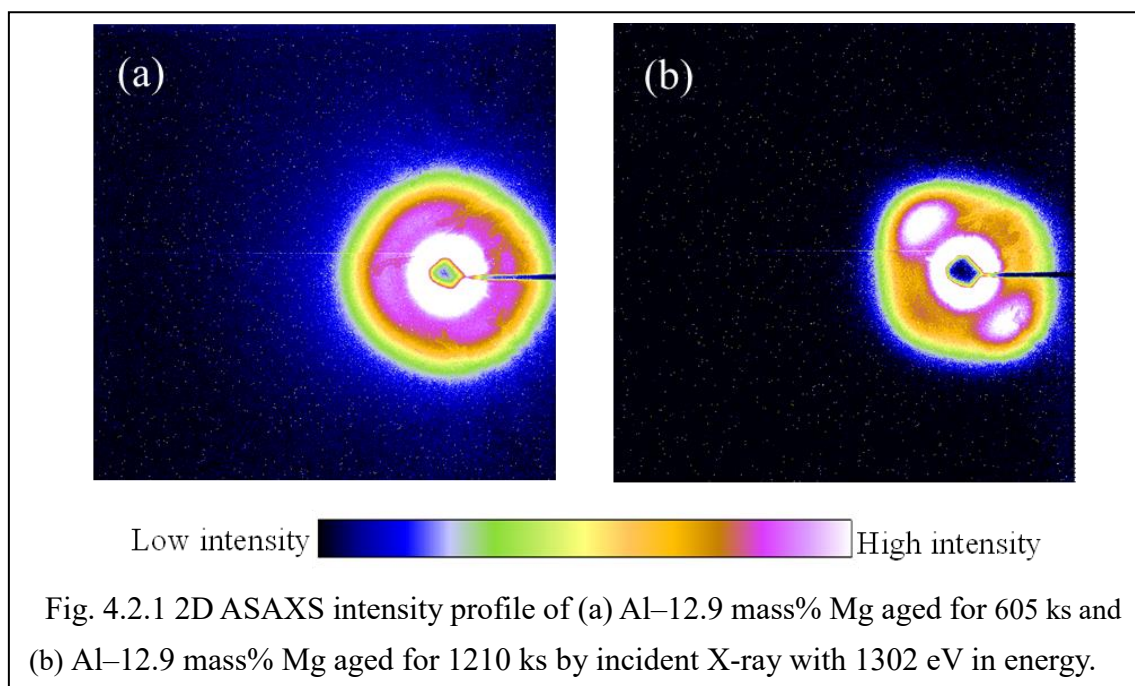
4.2. Nanostructure measurement of Al–Mg alloy via ASAXS method

4.2.1. Specimen and experiment details

The specimens are polished into a thickness of approximately 20 μm due to the low penetration ability for tender X-ray which has an energy in the vicinity of the *K* absorption edge in Mg. A standard specimen of powder silver behenate was used for scattering vector calibration, and an alloy of Al–13.4 mass%Mg was used for the calibration in incident X-ray energy.

4.2.2. Results of SAXS parameters via ASAXS measurement in Al–Mg alloys

Fig. 4.2.1 shows the 2D ASAXS intensity profile by the Al–12.9 mass%Mg alloy aged for 605 ks and 1210 ks at a temperature of 313 K. From the isotropic shape in Fig. 4.2.1 (a), it is evident that the scatterers detected are spherical, which showed an agreement with the TEM observation (Sato *et al.,* 1982). There is no local maximum found in the profile, indicating that the precipitates arranged either random, or too close or too apart from each other that the local maximum is out of the view range/shaded by beam stop in this measurement. On contrary, Fig. 4.2.1 (b) showed an anisotropic pattern with symmetric local maximum. Both of the shapes and the locations of the local maximum is identical to ⟨100⟩ view of Al–Mg alloys in the study by Dauger (1979) about the single crystalline alloy of Al–13 mol%Mg aged at the room temperature. Therefore, the nanostructures measured in the 1210 ks aged Al–12.9 mass%Mg alloy can be concluded

Fig. 4.2.1 2D ASAXS intensity profile of (a) Al–12.9 mass% Mg aged for 605 ks and (b) Al–12.9 mass% Mg aged for 1210 ks by incident X-ray with 1302 eV in energy.

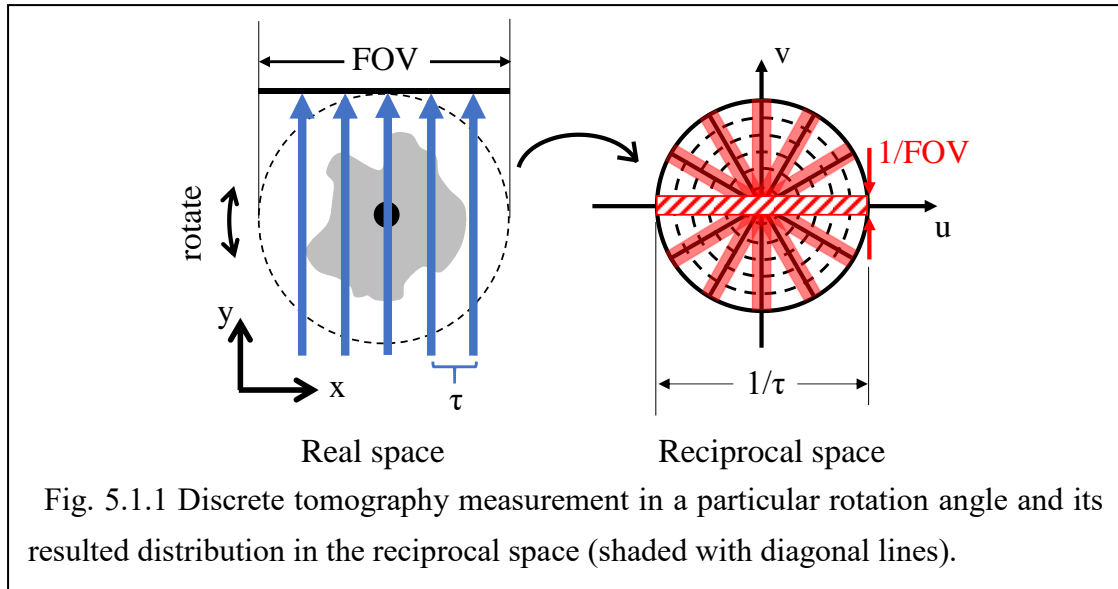as spherical G. P. zones, which aligned on the ⟨100⟩ direction more or less.

The relative integrated intensity was calculated from ASAXS profile after converted the 2D profile into 1D by radial averaging. The result of Al–12.9 mass% Mg alloy aged for 605 ks and 1210 ks are almost the same for 0.52 and 0.54 in the relative unit. The difference of this result is very trivial, compared to which in the aging time. Which indicates that for the Al–12.9 mass%Mg alloy, an artificial aging at 313 K for 605 ks is sufficient for completing the precipitation process, and has proceeded into the process of coarsening.

Guinier radius has also evaluated in both aging periods as 2.8 nm and 3.1 nm for 605 ks and 1210 ks respectively. It is obvious that the increased result of the precipitates size came from the coarsening effect with a prolonged aging time.

5.   Computed Tomographic technique with SAXS data and its applications

5.1.   Computed tomography in absolute units

5.1.1.   Absolute reconstruction in discrete computed tomography

Fig. 5.1.1 Discrete tomography measurement in a particular rotation angle and its resulted distribution in the reciprocal space (shaded with diagonal lines).

If combining the discussions in the section 2.6.3.2 which is about the influence from the discreteness in the rotation and translation steps, it is possible to conduct an absolute reconstruction in a discrete system even with a coarse interval, by recovering the reciprocal discrete distribution close to a continuous one.

Fig. 5.1.1 shows the projection process from an angle in the tomographic measurement, and the resulted distribution in the in the reciprocal space. The incident X-ray is calibrated into a pencil beam thinner than the translation interval τ. The blue arrows represent the X-ray projected to the specimen, and transmitted into a detector noted as the thick black line. After a single projection from a fixed position, the corresponding distribution in the reciprocal space after the Radon transformation which have shown as a rectangular with red diagonal lines. The red shaded rectangles without diagonal lines are the Radon transformed profile from different projection angles. The x and y axis in the real space corresponding to the axis u and v in the reciprocal space, or frequency. The size of the red diagonal lined square has a length for $1/FOV$ (FOV as field of view) on the u axis, and $1/\tau$ on the v axis. The reciprocal space in here is defined as $w = 1/x$, which is different from $w_{material} = 2\pi/x$ in the material science. It should be noted that the full rectangle in the reciprocal space represents the summed-up value of all voxels X-ray transmitted in a measurement.

The reason of the rectangular shaped distribution in the reciprocal space is explained as
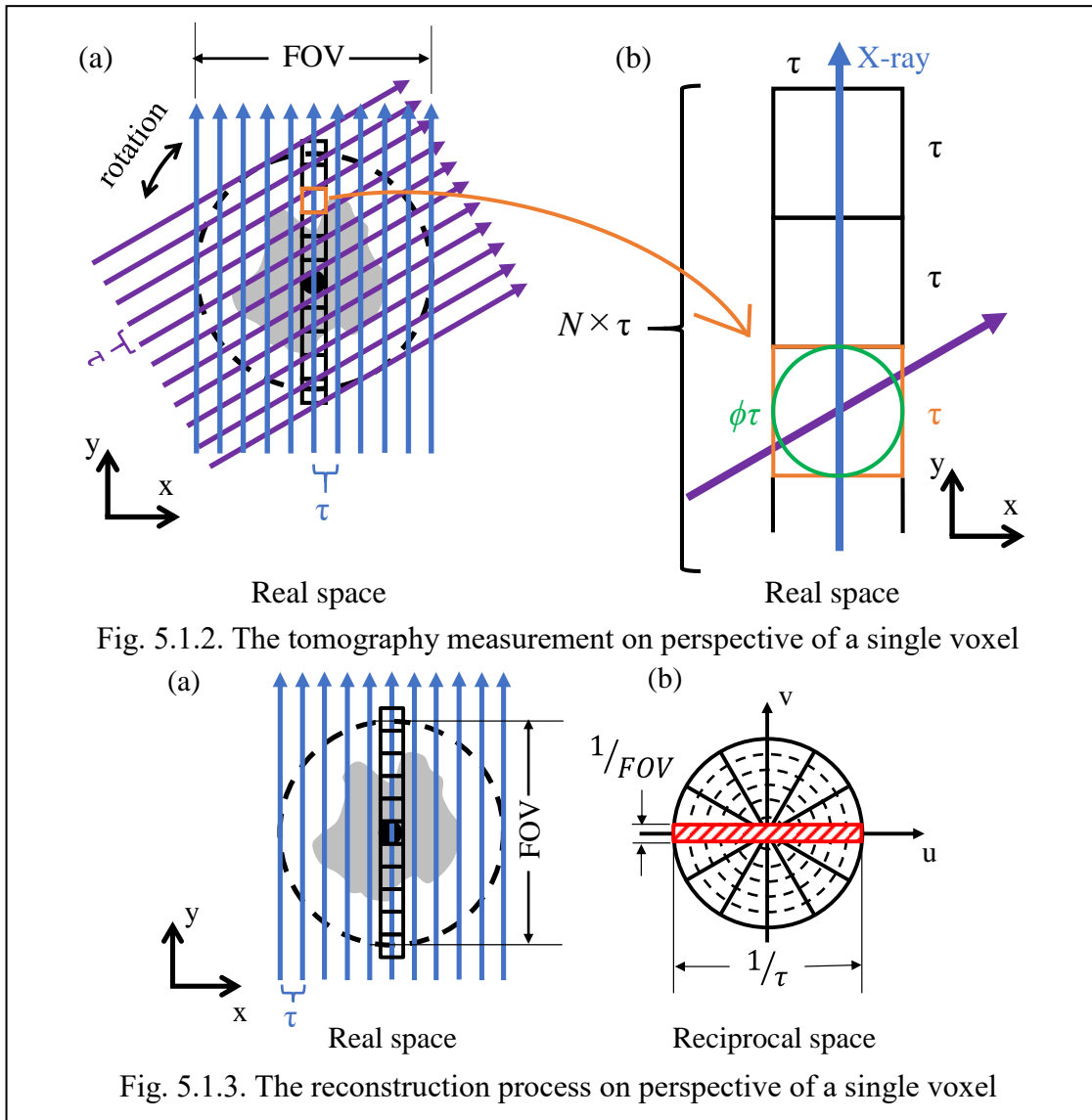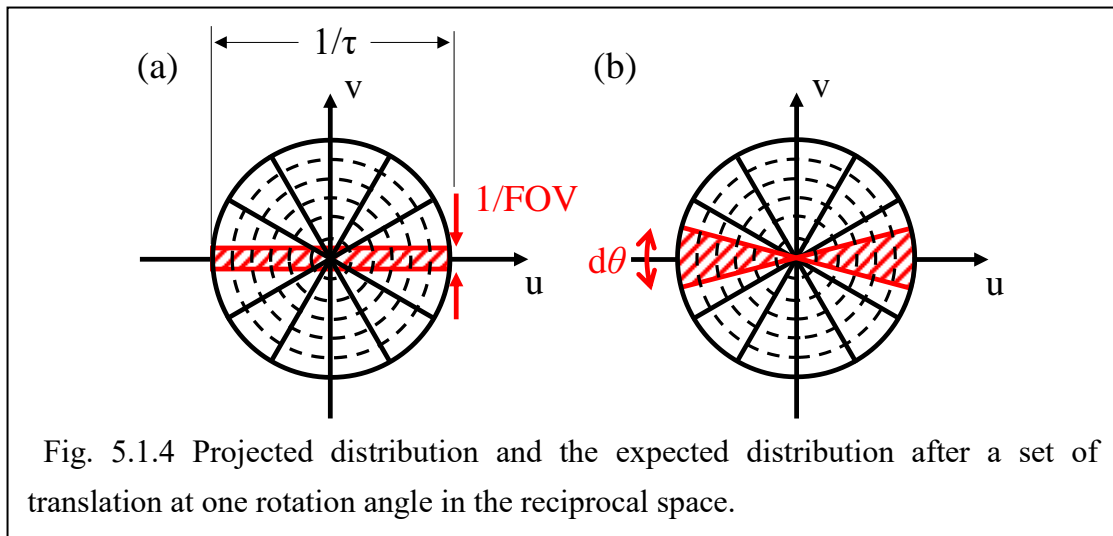
Fig. 5.1.2. The tomography measurement on perspective of a single voxel

Fig. 5.1.3. The reconstruction process on perspective of a single voxel

follows:

  Fig. 5.1.2 shows the reconstruction process from the perspective of a random voxel. After the reconstruction, the minimum voxel size would be the translational interval of the scanning X-ray, no matter what direction is projected from. Therefore, for a minimum sized voxel, as shown in Fig. 5.1.2 (b), for a single projection from a particular angle, the orange colored pixel with a size $\tau \times \tau$ would be input a value measured by a part of X-ray in length τ. After the rotation movement, the value for reconstruction would be the mean value of the green circle area with a diameter of τ in the voxel. This green circle is can be approximated to $\tau \times \tau$ for an easier calculation, and a better appearance for the image after the reconstruction. Due to the linearity of the parameter, the parameter's value measured by each projection is the projected value, i.e. the summed-up value of all penetrated

72

voxels. Therefore, the corresponding area in the real space for one measurement would be like, Fig. 5.1.2. (a), which is $\pi\left(\frac{\tau}{2}\right)^2 \times N \approx \tau \cdot N\tau$ where N is the number of voxels on a scanning direction, i.e. $FOV = N\tau$. For this reason, for a single projection in the tomography, the measured objective parameter would be a value represents a rectangle

Fig. 5.1.4 Projected distribution and the expected distribution after a set of translation at one rotation angle in the reciprocal space.

area of $\tau \times FOV$ in the real space. This area is identical to a rectangle with a dimension of $\frac{1}{\tau} \times \frac{1}{FOV}$ in the reciprocal space, as shown in Fig. 5.1.3. In addition, since each pixel only illuminated by the pencil beam X-ray once in a scanning process per rotation angle, the rectangular distribution can be applied to all pixels in the FOV. Also, for each pixel, the calculation above was proceeded with using the value of N pixels at a whole; therefore, after the summation from different angle, the resulting pixel value would be divided by N.

In order to fulfill the circle in the reciprocal space for a system discrete in both of the angular and translational direction, or it is inevitable to transform the shape of the rectangular distribution into a pie-shaped distribution. This process is identical to interpolate/truncate the uncovered/overlapped area in reciprocal space in the high/low frequency area after the measurements as shown as Fig. 5.1.1 (right) caused by discrete angle steps, i.e., to change the amplitude of the amplitude result of Radon transformed distribution in arithmetic direction, as shown in Fig. 5.1.4 (a) and (b). Because that the pie-shaped distribution can be approximated into a triangle, the relationship of the triangular and rectangular shaped distributions can be connected with a Ramp filter $H(w) = |w|$ where w is the frequency in reciprocal space, or the coordinate of u axis in the red shaded area in Fig. 5.1.4 (a). Therefore, for a tomography experiment with N

pixels (N is large number) scanned in the real space with interval τ, the relation of the two shape can be expressed as:

$$Q_{\theta,pie}(n\tau) = Q_{\theta,rect}(n\tau)H(n\tau) = KQ_{\theta,rect}(n\tau)|ndw|$$

where

$$n \in \left[-\frac{N}{2}, -\frac{N}{2}+1, \cdots, 0, \cdots \frac{N}{2}-1, \frac{N}{2}\right] \qquad K = \text{const.} \qquad (2.1)$$

$Q_{\theta}(n\tau)$ was the "filtered projection" mentioned in eq. (2.71) in the section 2.6.3.1., n is the coordinate of pixels in the real space.

Therefore, the filter can be divided into a coefficient K and the Ramp filter $H(w) = |w|$.

5.1.1.1. Application of Ramp filter in the discrete system

The inversed Fourier transformation of Ramp filter is $H(w) = |w|$ is

$$\mathcal{F}_1^{-1}[H(w)] = h(t) = \frac{1}{2\tau}\frac{\sin(2\pi t/2\tau)}{2\pi t/2\tau} - \frac{1}{4\tau^2}\left(\frac{\sin(\pi t/2\tau)}{\pi t/2\tau}\right)^2. \qquad (5.2)$$

The discrete version of $H(m\frac{2W}{N})$ is

$$\mathcal{F}_1^{-1}[H(mw)] = h(t) = h(n\tau) = \begin{cases} \dfrac{1}{4\tau^2} & n = 0 \\ 0 & n = even. \\ -\dfrac{1}{n^2\pi^2\tau^2} & n = odd \end{cases} \qquad (5.3)$$

The graph of the continuous and the discrete $h(t)$ have both shown in Fig. 5.1.4.
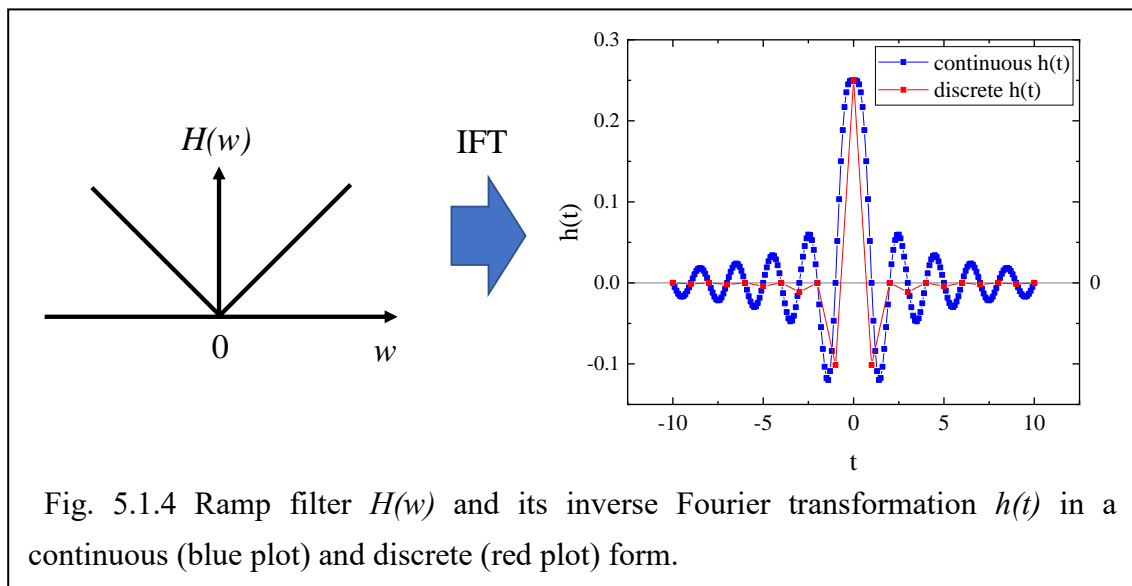

Fig. 5.1.4 Ramp filter *H(w)* and its inverse Fourier transformation *h(t)* in a continuous (blue plot) and discrete (red plot) form.

Therefore, the final result is

$$Q_\theta(n\tau) \approx \tau P_\theta(n\tau) \circ h(k\tau) = \tau \sum_{k=0}^{N-1} P_\theta(n\tau - k\tau)h(k\tau)$$

$$\text{where } h(k\tau) = \begin{cases} {1}/{4\tau^2} & k = 0 \\ 0 & k = even, \quad n \in [0, 1, 2 \cdots N - 1] \\ {-1}/{n^2\pi^2\tau^2} & k = odd \end{cases} \tag{5.4}$$

5.1.1.2. Deformation of measured profile in reciprocal space

For a tomography rotated $M+1$ times for an angular range of 180°, and N pixels with a size of τ for the length FOV, the measured reciprocal distribution, or the red shaded rectangle would have an area of:

$$\frac{1}{\tau} \times \frac{1}{\tau N} = \frac{1}{\tau^2 N}. \tag{5.5}$$

The expected pie-shaped distribution would have an area of

$$\frac{\pi}{M} \times \left(\frac{1}{2\tau}\right)^2 \times 2 = \frac{\pi}{2M\tau^2}. \tag{5.6}$$
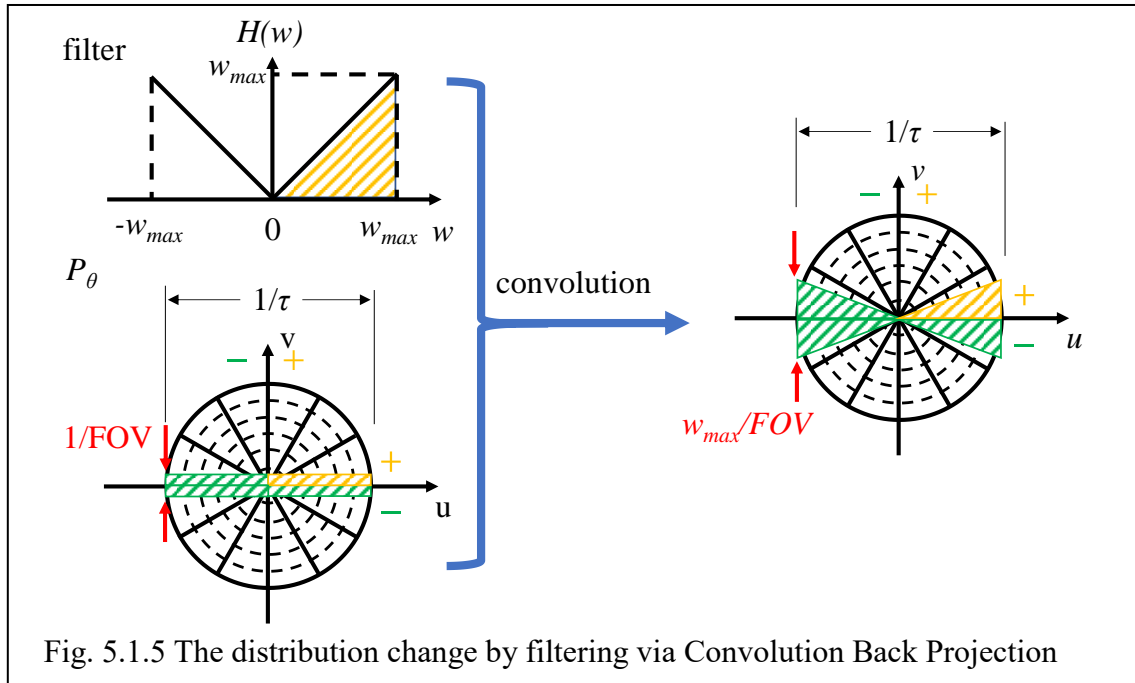
Fig. 5.1.5 The distribution change by filtering via Convolution Back Projection

Because a filter also has its distribution in the reciprocal space, so the length/area of a filter also has to be considered. The outline of the process has shown as Fig. 5.1.5. It is easy to divide the original rectangular P_θ into four parts by the sign of minus and plus in

both u and v axis, due to the symmetry of the Ramp filter *H(w)*. The area of the ramp filter with both plus sign is shown as yellow shaded area in Fig. 5.1.5. In this area, both the amplitude and the frequency *w* are positive, which means

$$w \in \left[0, \frac{1}{2FOV}, \cdots \frac{1}{2\tau}\right], amplitude \in \left[0, \frac{1}{2FOV}, \cdots \frac{1}{2\tau}\right] \tag{5.7}$$

the yellow area in the filter would be

$$\frac{1}{2}w_{max}^2 = \frac{1}{8\tau^2}. \tag{5.8}$$

Since either of the FBP and CBP method is a multiplication process in the reciprocal space, the filtered area in right side would be

$$\frac{1}{\tau^2 N} \times \frac{1}{8\tau^2} \times 4 = \frac{1}{2\tau^4 N}. \tag{5.9}$$

Therefore, the coefficient linking the filtered area and the pie-shaped area in the reciprocal space would be

$$\frac{(5.6)}{(5.9)} = \frac{\pi}{2\tau^2 M} \Big/ \frac{1}{2\tau^4 N} = \frac{\pi N}{M}\tau^2. \tag{5.10}$$

If consider that for every pixel on the X-ray path is all summed up to the scattered area, and in the reconstruction process, each pixel is calculated individually, then the influence for each pixel from a single rotation angle would be averaged by *N* pixels in *FOV*:

$$K = \frac{\pi N}{M}\tau^2 \div N = \frac{\pi}{M}\tau^2. \tag{5.11}$$

Consequently, eq. (5.10) is the final expression of the coefficient linking the measured distribution in the reciprocal space by a rough measurement, to the distribution in the reciprocal space for an absolute reconstruction.

5.1.2. Absolute unit in intensive/extensive parameters

The term "absolute unit" and "absolute intensity" has been used throughout this treatise, and also in the SAXS profiles by other researchers (Osamura *et al.,* 1979; Hennion *et al.,* 1982). The absolute unit or the differential scattering cross-section of the intensity indicates the intensity detected in a unit solid angle measured (sr^{-1}) which scattered from a unit volume (cm^{-3}), by a unit flux of incident X-ray ($1/cm^{-2} \cdot s^{-1}$) in a unit period of time (s^{-1}). Therefore, the absolute intensity of differential cross-section $\left(\frac{d\sigma}{d\Omega}\right)$ is consequently an intensive parameter with a unit of:

$$sr^{-1} \cdot cm^{-3} \cdot \frac{1}{cm^{-2} \cdot s^{-1}} \cdot s^{-1} = cm^{-1} \cdot sr^{-1}. \qquad (5.12)$$

When this absolute intensity was used as a unit for a SAXS profile, the absolute integrated intensity using differential cross-section would be

$$Q_{diff} = \int I(q)q^2 dq = \int \left(\frac{d\sigma_q}{d\Omega}\right) \cdot q^2 \cdot dq \to cm^{-1} \cdot sr^{-1} \cdot (cm^{-1})^3$$

$$\to cm^{-4} \cdot sr^{-1}. \qquad (5.13)$$

where $\left(\frac{d\sigma_q}{d\Omega}\right)$ is the differential cross-section on a scattering vector q. If using the total cross-section for SAXS profile, instead of differential cross-section, then the total cross-section of the integrated intensity would be:

$$Q_{total} = \int \sigma(q)q^2 dq = \int \frac{2}{3} \cdot 4\pi \cdot \left(\frac{d\sigma_q}{d\Omega}\right) \cdot q^2 \cdot dq$$

$$= \frac{8}{3}\pi Q_{diff} \to cm^{-4}. \qquad (5.14)$$

Both Q_{diff} and Q_{total} are intensive parameters, from the reason that eq. (5.14) link directly to the sum of the total cross-section in a unit volume of cm^3.

5.2. Vector tomography

The term "vector tomography" is used when the parameter for reconstruction is a set of vectors, like in the 1D SAXS profile (I_r, q_r). Every modulus of the scattering vector has its respective intensity to correspond. For the same reason, the conventional tomography which uses a scalar as a reconstruction parameter is then would be called a "scalar tomography"; a tomography using a tensor—e.g. SAXS tomography measured in 3D $(I_{r,\theta,\chi}, q_r, q_\theta, q_\chi)$—would be called a "tensor tomography".

5.2.1. Feasibility of reconstruction in vector tomography

Fig. 5.2.1 A schematic illustration showing the similarity and difference in (a) the scalar tomography and (b) the vector tomography.
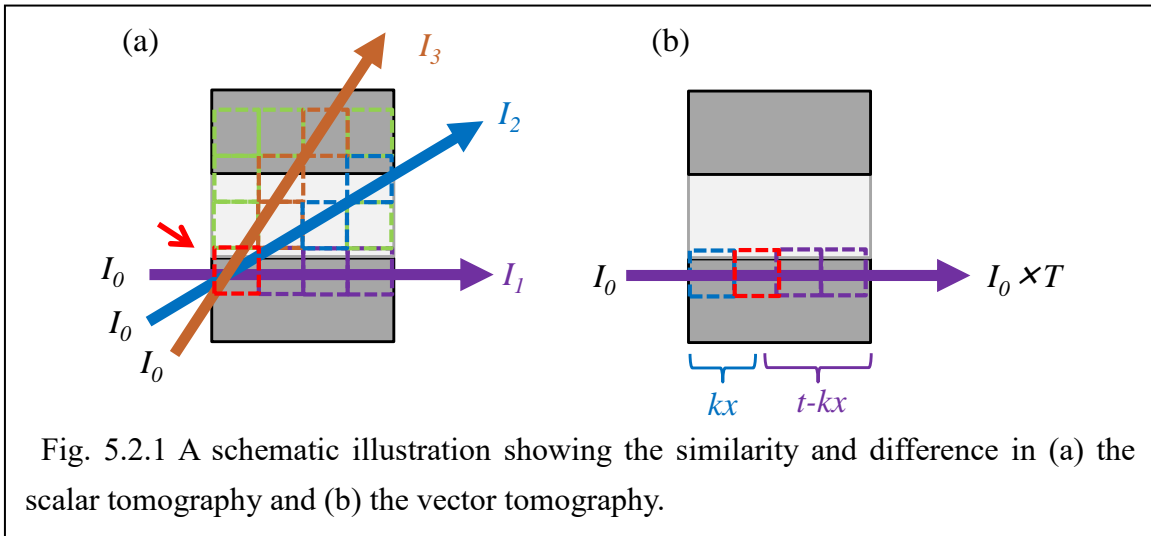
In the scalar tomography of attenuation coefficient like in Fig. 5.2.1 (a), the transmitted X-ray intensity (or transmittance) can be expressed with the attenuation coefficient and thickness in each volume element, i.e. in each voxel, with a dimension x in length:

$$I_j = I_0 \times e^{-(\mu_{1,j}\text{x} + \mu_{2,j}\text{x} + \cdots \mu_{N,j}\text{x})} \tag{5.15}$$

$$\sum_j \mu_{i,j}\text{x} = -\ln\left(\frac{I_0}{I_j}\right) = -\ln(T_j) \tag{5.16}$$

eq. (5.16) indicates that the parameter for reconstruction is a summation related to the respective voxel corresponding to, i.e., the attenuation coefficient is a linear parameter. This is the reason that attenuation coefficient can be reconstructed.

The same linearity is expected to be observed in vector tomography, since which is also needed to be reconstructed. As shown in the Fig. 5.2.1 (b), to consider the scattered X-ray in the kth voxel, with a pencil X-ray is transmitted from I_0 to I_1, then:

$$I_{scatter,k} = I_0 \times (attenuation\ untill\ voxel\ k)$$

78

$$\times (scattering\ cross\text{--}section\ in\ k^{th}\ voxel)$$
$$\times (attenuation\ after\ k^{th}\ voxel)$$
$$= I_0 \times (scattering\ cross\text{--}section\ in\ k^{th}\ voxel) \times e^{-\sum \mu_j x}$$
$$= I_0 \times (scattering\ cross\text{--}section\ in\ k^{th}\ voxel) \times T_k. \qquad (5.17)$$

Therefore in general,

$$I_{scatter} = I_0 \times \sum_j (scattering\ cross\ section)_{i,j} \times T_j. \qquad (5.18)$$

eq. (5.16) demonstrates that the scattered intensity can also be changed into an expression of summation of vectoral parameter, demonstrates the linearity in the scattering cross-section. The feasibility of the reconstruction for SAXS tomography on a 2D plane cross-section of an object specimen is confirmed.

5.2.2. Data selection in SAXS profile for vector tomography

vector tomography and the data selection in 2D SAXS profile
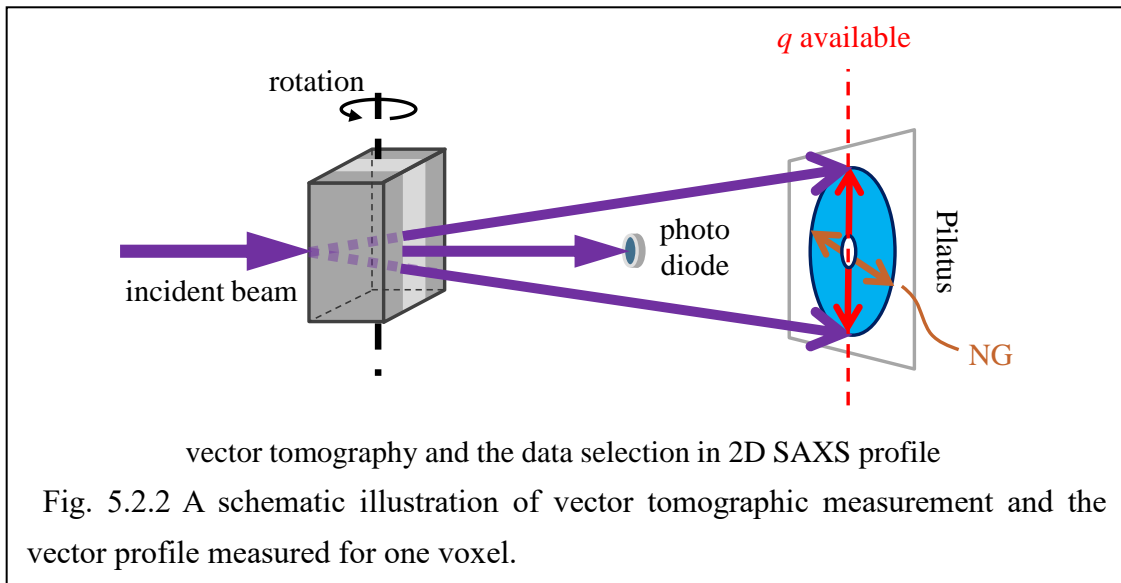
Fig. 5.2.2 A schematic illustration of vector tomographic measurement and the vector profile measured for one voxel.

Fig. 5.2.2 displays the operation in a SAXS tomography using vector tomography technique, which combined SAXS with CT (for this reason, also called SAXS-CT). As mentioned in section 2.7, due to the reconstruction process, every voxel is needed to be back-projected from all the projection direction. Therefore, only the part of measured 2D SAXS profiles which located on the line of the rotation axis is available to be used for reconstruction, and which is practically 1D SAXS profile. This reason comes from the reasons following:

In a scalar tomography, only a single scalar value exists in one voxel, which is a constant. However, in the SAXS tomography using vector tomography technique, after a full

rotation of 180° or 360°, all the scattering vector and the intensity corresponding to is altered by the projection direction, except for the ones on the rotation axis, as shown in Fig.5.2.2. If the objective specimen is anisotropic like the multilayered composite in this treatise, then the area selection in the measured 2D SAXS profile is needed a special care.

Therefore, the SAXS tomography in this treatise is vector tomography on the normal direction of the measured cross-section.

5.3. Result of SAXS Computed Tomography applied to multilayered binary composite

5.3.1. Al/Al–Zn/Al multilayered composite

5.3.1.1. Quantitative computed tomography in interdiffusion layer Al/Al–Zn

5.3.1.1.1. Specimen and Experiment detail

Fig. 5.3.1 Illustration of 3-layered composite and the cut area for square pillar
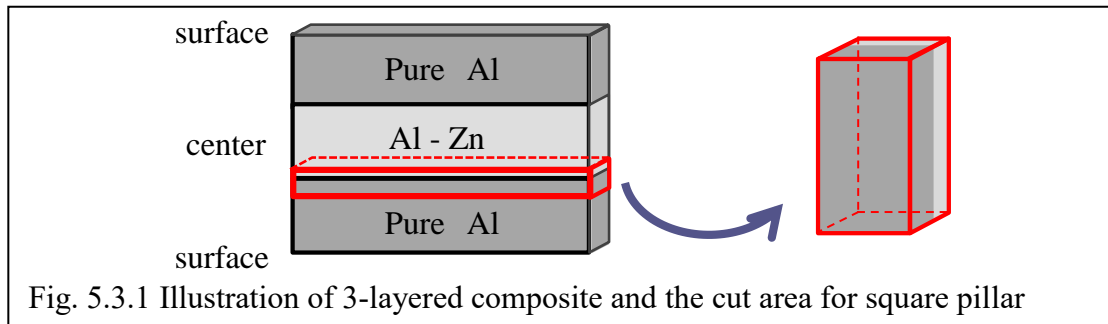
The binary composite specimen used in the SAXS tomography was a square pillar cut from a three-layered Al/Al–Zn/Al composite sheet, as shown in Fig. 5.3.1. The pillar was perpendicular to the interdiffusion direction, having a cross-section 400 μm × 800 μm approximately. The three-layered sandwich composite is the same specimen for 1D scanning measurement in the section 3.2–3.4.

The heat treatment was conducted on the sheet meal before cutting into square pillar. The original three-layered sheet was conducted a same series of heat treatment as 1D scanning SAXS measurement in the section 3.3.

Fig. 5.3.2 A schematic illustration of tomography measurement and a photo of square pillar specimen.
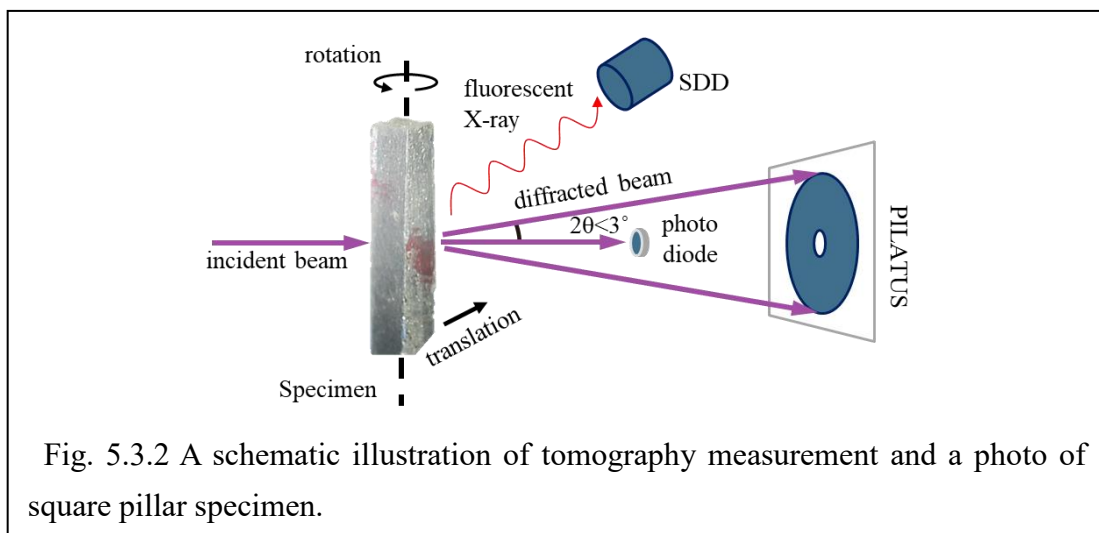
The computed tomography measurement with SAXS method was conducted with Zn fluorescent X-ray detection simultaneously, as shown in Fig. 5.3.2 with a photo of the rectangle pillar specimen. The investigation was conducted in Spring-8, BL40XU. High-

flux X-ray beam with an energy of 15 keV was used, and the diameter was calibrated by a pin hole with 20 μm in diameter. The translation and rotation angle step were set for 20 μm and 3°.

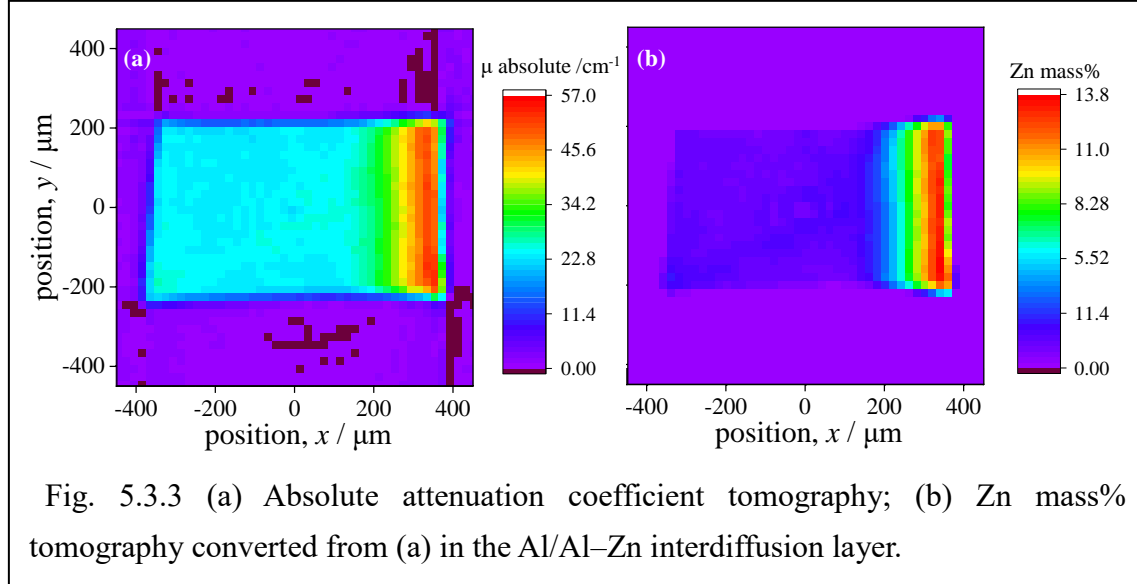### 5.3.1.1.2. Quantitative attenuation coefficient tomography and Zn composition tomography

Fig. 5.3.3 (a) Absolute attenuation coefficient tomography; (b) Zn mass% tomography converted from (a) in the Al/Al–Zn interdiffusion layer.

Fig. 5.3.3 (a) shows the result of the absolute attenuation coefficient tomography. This quantitative map has a range of value between 23 cm^{-1} to 57 cm^{-1}, and was converted into a map of Zn distribution in Al–Zn alloy shown in Fig. 5.3.3 (b), by using the relationship of

$$\frac{\mu_{alloy}}{\rho_{alloy}} = \sum_\alpha \omega_\alpha \cdot \frac{\mu_\alpha}{\rho_\alpha} \tag{5.19}$$

where μ_α is the absorption coefficient of the constituent element α; ω_α is the mass fraction of element α; and ρ_α is the density of element α. For a Al–Zn binary alloy, the relationship of μ_{alloy} and ω_{Zn} is

$$\omega_{Zn} = \frac{1}{2}\big(1701 + 5.054\mu_{alloy}\big) - \sqrt{\Delta}$$

where $\quad \Delta = \big(1701 + 5.054\mu_{alloy}\big)^2 - 4 \times \big(8.696\mu_{alloy} - 184.9\big) \tag{5.20}.$

The Zn composition in Fig. 5.3.3 (b) indicates that the specimen cut from the three-layered sheet metal has covered 98.1% in the Zn composition of the interdiffusion area, which contains a maximum of Zn of 14.07 mass% have in shown in the Table 2.7.1.

82

5.3.1.2. 2D Zn distribution in Al/Al–Zn square pillar by EDX measurement

(a)

(b)

Fig. 5.3.4 (a) SEM images of the cross-section of the square pillar; (b) 2D EDX result of Zn concentration on (a).
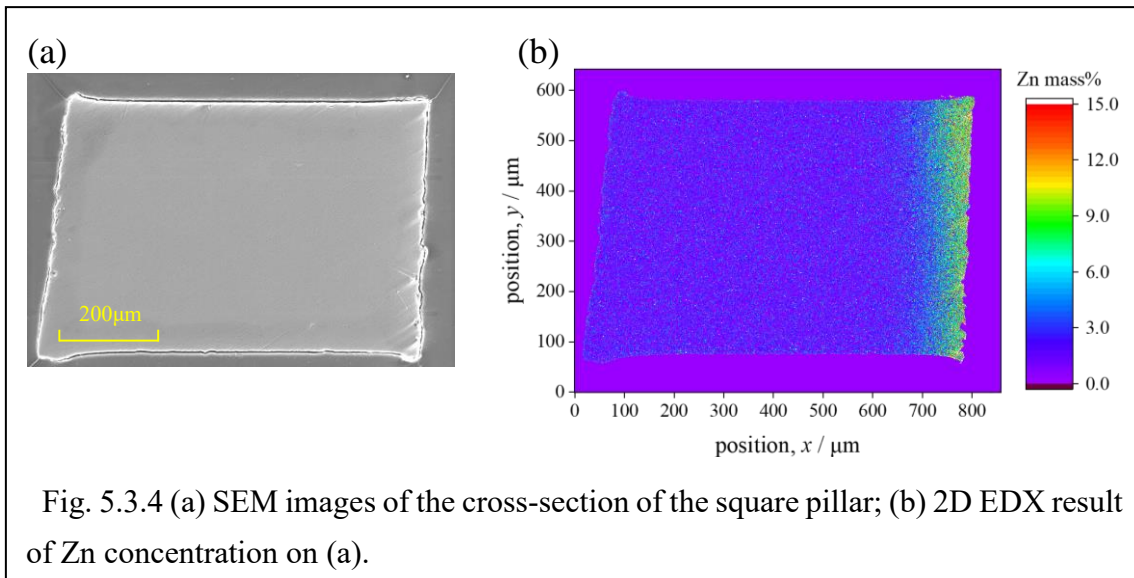
Fig. 5.3.4 (a) and (b) exhibits the SEM image and the corresponding EDX map of Zn concentration on a cross-section on the same pillar of SAXS-CT, with a distance of 1 mm apart from the tomographic image, i.e., Fig. 5.3.3. The average solute distribution curve was obtained by taking the mean values of Zn composition over the y direction on the Fig. 5.3.4 (b), which is also normal to the interdiffusion direction, between $y = 320$ μm and 470 μm. The mean Zn composition distribution are shown as black dots in Fig. 5.3.5.
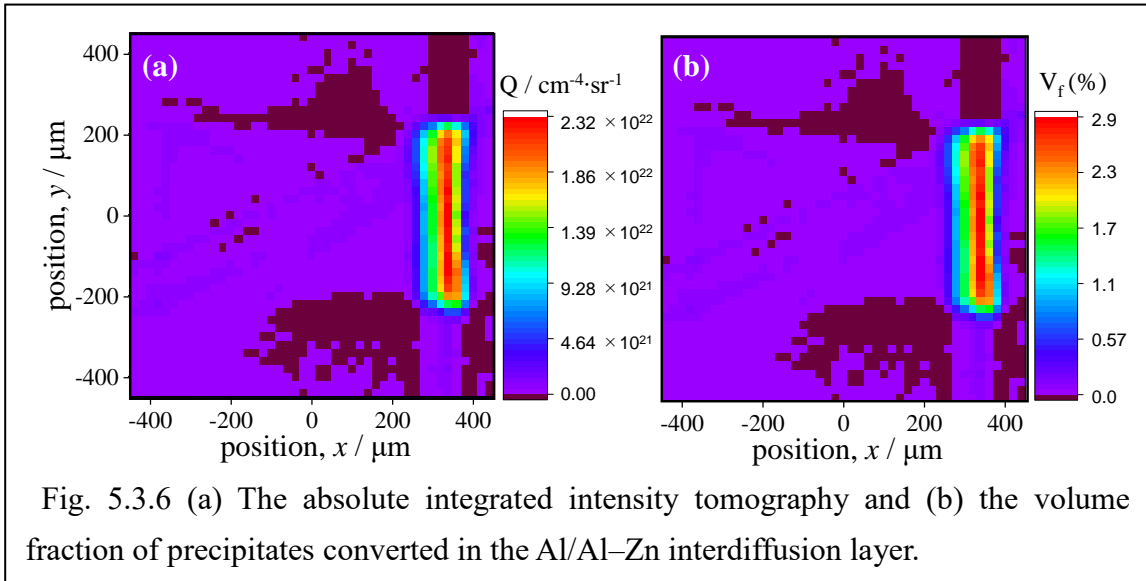
The grey dots in Fig. 5.3.5 showing the average distribution of Zn composition from tomographic result Fig. 3.1.4 (b). Which underwent a same averaging method as the EDX result . The distributions of the black and grey dots from two individual measurements

Fig. 5.3.5 Zn concentration profile from the tomography result (grey dot) and the EDX result (black dot)
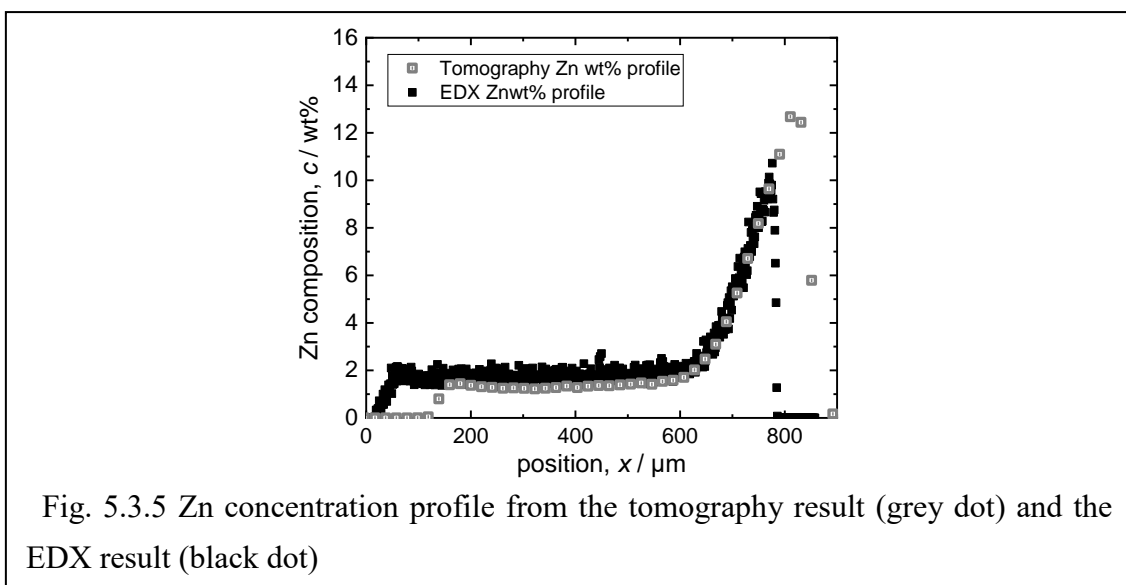
showed an excellent agreement, except for which in the edge positions of the pillar. The present result indicates that the Zn composition in the sample ranges from 1.5% to 13.8% in mass.

5.3.1.3. Absolute integrated intensity and volume fraction tomography

The absolute integrated intensity tomography represented as the differential cross-section was reconstructed from the projected integrated intensity, which shown as Fig. 5.3.6 (a). This image was regulated by the glassy carbon from the Nilaco Corp., by calibrating the detected SAXS intensity profile of the glassy carbon into the profile of the differential cross-section in unit of $cm^{-1} \cdot sr^{-1}$. For the reason that the parameter in the tomography reconstruction was treated as an extensive parameter, the dimension of voxel in the X-ray direction i.e., 0.002 cm (20μm) was calibrated for each voxel after the reconstruction.

Fig. 5.3.6 (a) The absolute integrated intensity tomography and (b) the volume fraction of precipitates converted in the Al/Al–Zn interdiffusion layer.

By comparing with 5.3.1.1.2.1 (b), this image indicates that the precipitation of G. P. zones took place when the composition of Zn exceeds approximately 6.2% in mass, and this result showed a discrepancy of 1.0% with the 1D scanning result, which is 5.2% Zn in mass.

The volume fraction of the precipitates V_f was converted with eq. (2.24) in the item 2.2.1.2.2 and eq. (5.13) in the section 5.1.2. In this calculation, the unit was converted from e.u. into $cm^{-4} \cdot sr^{-1}$ by considering the electron density difference $\Delta\rho$ of the precipitate, i.e. G. P. zone, and the matrix.

$\Delta\rho$ is calculated by the volume of the unit cell and the density of the elements in the

either phase. Zn composition of G. P. zone and the matrix was conducted via the free energy curve at the artificial aging temperature 313 K and the common tangent line in Al–Zn system studied by Sato *et al.* (1979)：

$$\frac{F^s}{R} = X(1 - X)(1080 - 1590X + 0.3753T + 1.910XT)$$

$$+T[X \ln X + (1 - X) \ln(1 - X)] \tag{5.21}$$

where F^s is the free energy of the alloy, R is the gas constant, X is the atomic composition of an element, T is the absolute temperature. The Zn composition in the matrix and the G. P. zone was calculated as 1.9 mol% and 72 mol%.

The lattice constant by different Zn composition in binary Al alloy was evaluated by using the linear relation of the two constants in the room temperature by Popović *et al.* (1992). From the fact that the Zn composition ranged 0–15 mass% (0–6.8 at%) and the resulting lattice constant is 0.40494 nm and 0.40426 nm for 0 at% and 8 at% (Popović *et al.*, 1989, 1992). The difference in the lattice constant is lower than 1% and therefore which of the G. P. zone and the matrix was fixed as 0.404 nm. The lattice constant of either of the phases was considered identical, form the fact that G. P. zone is facet to the matrix.
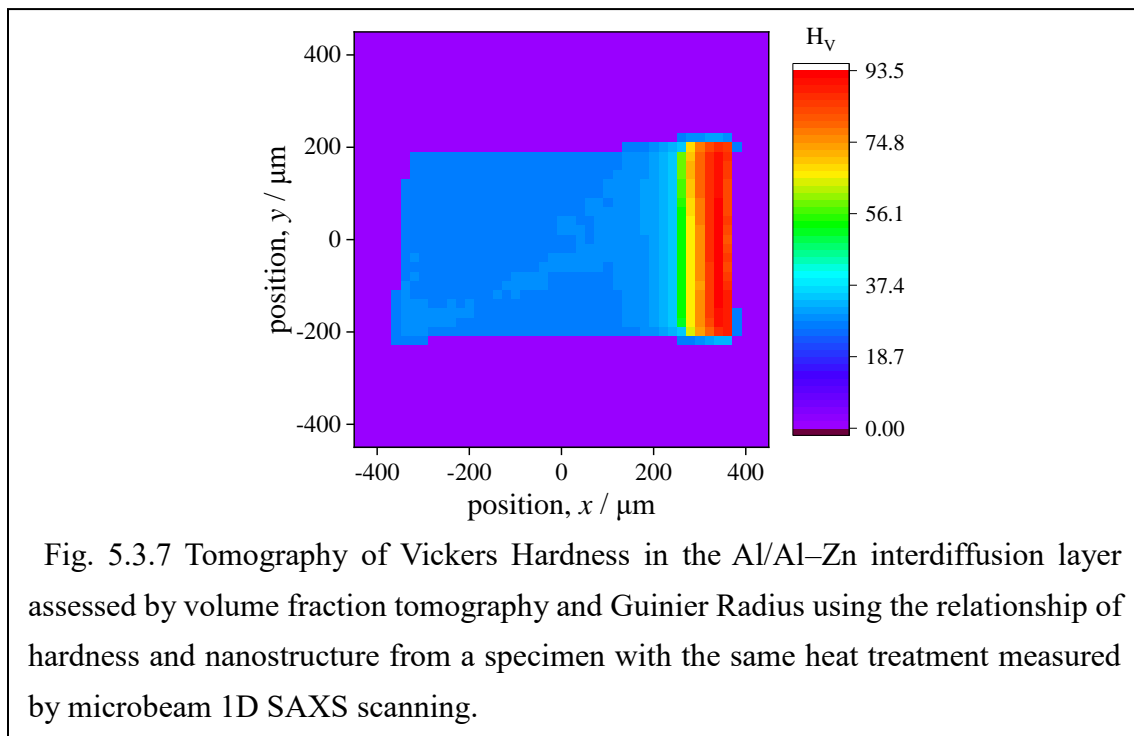
The electron density in both of the phases resulted in $\Delta\rho = 7.21 \times 10^{23}$ electrons/cm^3. Like mentioned in the 1D scanning measurement, that the phase separation is unique in this binary composite, regardless of Zn composition unless completely dissolved.

The volume fraction of G. P. zone in the interdiffusion layer was shown as Fig. 5.3.6 (b). The volume fraction of G. P. zones was in the range of 0 to 2.8%. This is lower than that estimated from the preceding works (Komiya *et al.,* 2006; Gerold, 1961; Osamura & Murakami, 1979; Gerold & Merz,1967). For example, a volume fraction of 2.6% in the 4.7 mol%Zn alloy can be calculated from the work of 3-dimensional atom probe (3DAP) by Komiya *et al.* (2006). However, the evaluated volume fraction in the tomography is 1.8% at 11.1 mass%Zn (i.e., 4.9 mol%). This is due to the low accuracy in the transmittance data when X-ray illuminates nothing but air, which can be confirmed by reducing the density approximately 1.5 mass%Zn for all voxels in the specimen. This value is the Zn composition result that locates in the range 200–500 μm in Fig. 5.3.5. This plateau area is naturally considered as pure Al, for either the results of the EDX and the tomographic measurement. Therefore, the density of 12.2 mass%Zn in the tomographic image would be converted as 4.7 mol%Zn (10.7 mass%) and the volume fraction in this density resulted as 2.2%, which is consistent to the preceding works which is 2.6%. This

deviation of 1.5 mass%Zn can also be verified by recalling the result of attenuation tomography which showed a difference with 1.0% mass%Zn.

5.3.1.4. Assessment of local hardness and UTS tomography

As mentioned in section 3.4, in a SAXS measurement, Guinier radius is identical to the radius of gyration, and can be regarded as an averaged parameter in the volume X-ray past through. However, considering that the radius of gyration is not linear to the constituent like integrated intensity; which implies that it is not valid to used Guinier radius from the projected SAXS as a parameter for tomographic reconstruction as mentioned in section 5.2.1. Therefore, the Guinier radius in each voxel has to be estimated individually, which implies the tomographic reconstruction of the whole SAXS profile from each projection direction. For this rectangular pillar as a laminated composite, in the direction perpendicular to the interdiffusion direction, i.e. in the y axis of Fig. 5.3.3, the attenuation coefficient and Zn composition is relatively constant; which implies that in this direction, the rectangular pillar can be considered homogeneous locally. Taking advantage of this special property, the Guinier radius in each voxel was evaluated by using the SAXS profiles illuminated from the y direction in the x coordinate of each voxel. This process of evaluating the mean radius is identical to which of 1D scanning SAXS measurement in section 3.

Fig. 5.3.7 Tomography of Vickers Hardness in the Al/Al–Zn interdiffusion layer assessed by volume fraction tomography and Guinier Radius using the relationship of hardness and nanostructure from a specimen with the same heat treatment measured by microbeam 1D SAXS scanning.

The resulting Guinier radius along y direction image ranged from 2.16 nm to 3.56 nm. With the volume fraction evaluated in Fig. 5.3.6 (b), the local hardness in each voxel of the tomographic measurement was estimated from these nanostructure parameters, using the underaged relationship confirmed in the section 3.4. For the solid solution region, the hardness was evaluated as the function of Zn concentration using the relationship of Zn concentration and the hardness in the section 3.4. These were summarized as Fig. 5.3.7.

5.3.1.5. Evaluation of assessed UTS tomography from nanostructure

The hardness can be shown in UTS using an empirical relationship (Sato & Endo, 1986; Zhang, *et al.,* 2011) of

$$\sigma(UTS) \approx 1/3 \times H_V \tag{5.4}$$

where H_V is the Vickers hardness.

Also, if an alloy is strengthened by nanostructure only, the Critical resolved shear stress (CRSS) can be estimated from (Gerold and Haberkorn, 1966)

$$\Delta\tau_0 \approx 3\mu|\varepsilon|^{1.5} \left(\frac{RV_f}{b}\right)^{0.5} \tag{5.5}$$

where μ is the shear modulus; R the radius of precipitation; b the length of Burger's vector; ε the linear misfit parameter of particle and matrix. ε can be evaluated with (Mott, & Nabarro, 1940; JIM, 1976)

$$\varepsilon \approx \frac{1}{a}\left(\frac{da}{dc}\right) \tag{5.6}$$

where a is the lattice constant, c the solute density. The average value of ε was 0.0216. With the value of this ε and the shear modulus of pure Al which is 27 GPa, the coefficient of $\Delta\tau_0$ and $\sqrt{RV_f}$ is calculated as 4.05×10^{-10}. Since UTS converted from Fig. 5.3.7 also uses a coefficient to connect τ and $\sqrt{RV_f}$ with the cut through mechanism by eq. (3.2) in section 3.4, the relationship of theoretical yield strength and UTS was calculated as:

$$\frac{\tau_{UTS}}{\tau_{yield}} = 1.56 \tag{5.7}$$

5.3.2. Quantitative computed tomography in Al/Al–Zn/Al composite
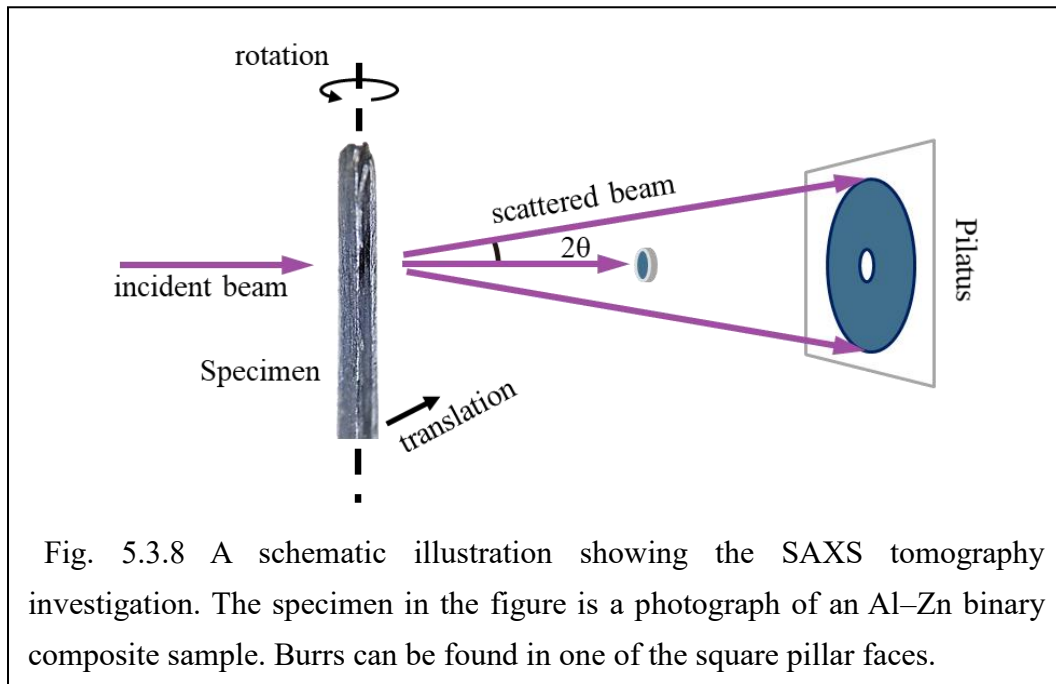### 5.3.2.1. Sample preparation

Fig. 5.3.8 A schematic illustration showing the SAXS tomography investigation. The specimen in the figure is a photograph of an Al–Zn binary composite sample. Burrs can be found in one of the square pillar faces.

Another rectangular pillar was cut from a three-layered sheet metallic composite with the thickness rolled down into 0.5 mm in the last cool rolling process, instead of 2 mm. The interdiffusion layer thickness was controlled to approximately 200 μm with interdiffusion treatment, and the movement steps of local nanostructure investigation by a SAXS tomography method was controlled as 20 μm and 3° as shown in Fig. 5.3.8.

The Al/Al–Zn/Al composite with a thickness of 500 μm underwent a similar heat treatment before cut into the rectangular pillar with 1D SAXS scanning measurement and 2D SAXS-CT measurement in section 3.2–3.4 and 5.3.1. After the interdiffusion treatment process at 773 K for 14.4 ks with iced water quenching, it was it was kept for 300 s in a vertical furnace at 573K for solid solution treatment, followed by a rapid iced water quenching. The artificial aging was also conducted on this sheet metal by an oil bath for 3.6 ks at 313 K.

The pillar was cut from the sheet metal into a squared pillar shown in the Fig. 5.3.8 after the series of heat treatment. Either of the pillar was cut in the roll direction (RD) plane of rolled sheet metal, therefore the squared cross-section was composed by the traverse direction (TD) and normal direction (ND). The square dimension was restricted to about 500 μm, which is the length of the original layered thickness and cut distance.

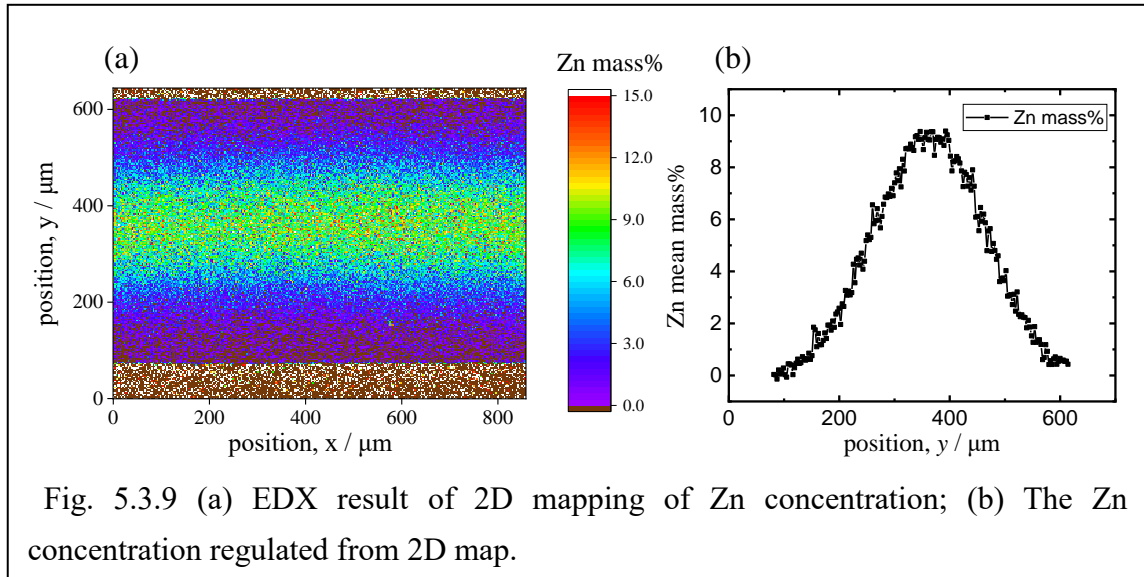## 5.3.2.2. Solute distribution investigation via EDX

Fig. 5.3.9 (a) EDX result of 2D mapping of Zn concentration; (b) The Zn concentration regulated from 2D map.

Fig. 5.3.9 shows the Zn distribution was investigated with SEM-EDX measurement via 2D mapping. After 14.4 ks of interdiffusion treatment, the Zn concentration has a range of approximately 0–9.6 mass% lower than the maximum composition of the single layer 14.7 mass%, indicating the two of the interdiffusion layers has encountered and fused into one layer.

5.3.2.3. Absolute attenuation coefficient and Zn composition tomography
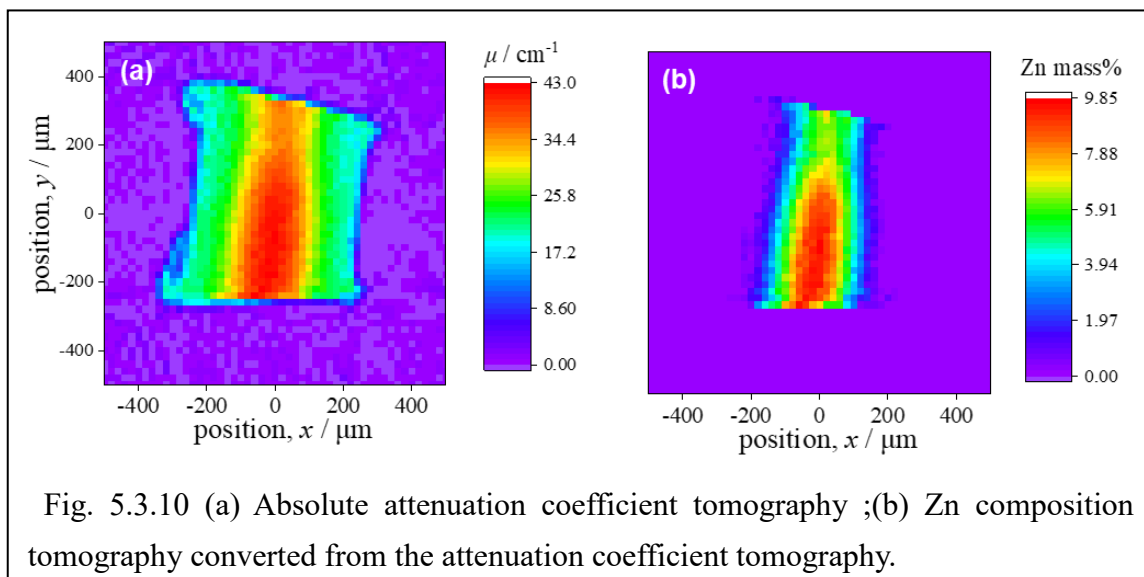
Fig. 5.3.10 (a) Absolute attenuation coefficient tomography ;(b) Zn composition tomography converted from the attenuation coefficient tomography.

Fig. 5.3.10 (a) is the reconstructed 2D image of the absolute attenuation coefficient, showing the 2D planar distribution of a 20 μm thick cross-section in the square pillar.

Each value represents the mean value of a cubic area with 20 μm × 20 μm × 20 μm in the squared pillar. The specimen showed a cross-section with a dimension of approximately 600 μm × 620 μm, and the burrs formed while cutting the pillar from the sheet metal are observed in all the four corners. Two of the four burrs are bent and contacted to the bulk pillar, which can be confirmed both from the tomography and the photo of specimen in Fig. 5.3.8. The mass fraction tomography of Zn is displayed in Fig. 5.3.10 (b). This image shows the maximum concentration of this specimen is 9.85 mass%. The result showed a good match with the EDX result which is 9.6 mass% at maximum.

Same with the 3 mm thick specimen discussed in the section 5.3.1.2, the interdiffusion direction of atoms is also on the x-axis in this map, which can be confirmed from the decrement of Zn concentration. However, the distribution of Zn on the y direction showed a different result from 3 mm thick pillar. For 3mm thick pillar in the section 5.3.1.2, the y direction is unformed in Zn concentration due to the equivalence in both of the diffusion distance starts from the interface of cladded layers, and the diffusion time in the interdiffusion process. For this 500 μm pillar shown as Fig. 5.3.10 (b), the Zn concentration on the y direction is not uniformed, and a dump can be observed in the area of y = 80 μm to 320 μm. In this dumping area, the thickness of the single layered Al–Zn alloy sheet is considered to be thinner than other area initially. Which indicates a necking in the thickness was made after the rolling process while manufacturing composite. For this reason, during the interdiffusion treatment process of 14.4 ks at 773 K, the maximum Zn concentration decreases faster in this thinner area, and the shape of necking in Zn distribution remains. This phenomenon that thickness fluctuation occurs on the middle layer after the rolling process is well known in the rolling or extrusion process while manufacturing multi-layered composite like the ones in our study (Arnold & Whitton, 1959; Shimura & Tanaka, 1975; Wilson *et al.,* 1975; Onodera & Hokamoto, 1987).

5.3.2.4. Absolute SAXS intensity tomography

Fig. 5.3.11 Reconstructed SAXS tomography result of Al/Al–Zn/Al composite: Absolute SAXS profile in $y = -20$ μm line.
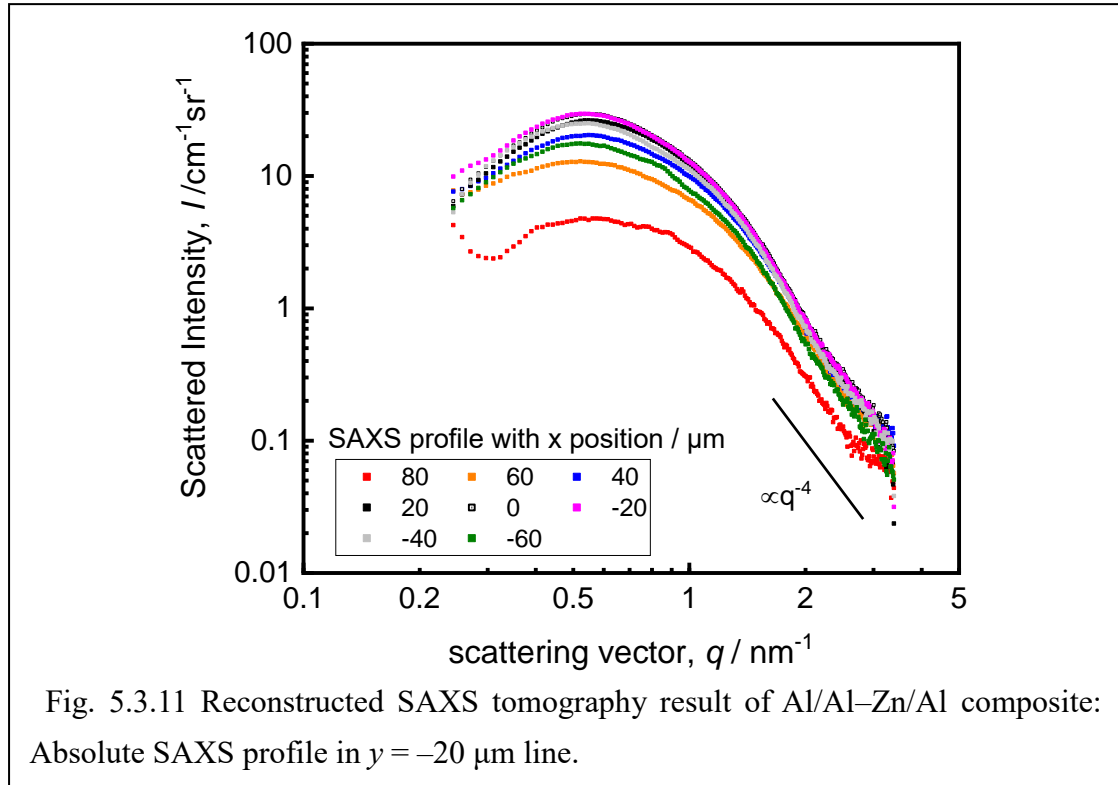
The absolute calibration with the SAXS profile of glassy carbon was performed after the reconstruction of relative SAXS profile in each voxel. Fig. 5.3.11 shows the SAXS profiles on the $y = -20$ μm line of Fig. 5.3.10 (a). The Porod's rule (Guinier & Fournet, 1955; Brumberger, 1956) was observed obeying in the reconstructed SAXS curve. The local maximum was found roughly on the position of 0.3 nm^{-1} scattering vector, which can be explained by the interference between different precipitates.

### 5.3.2.5. Absolute integrated intensity tomography

The distribution of the absolute integrated intensity Q was calculated using two different methods. The first method the absolute SAXS profile in each voxel was reconstructed first; then, the absolute integrated intensities were calculated using the reconstructed profiles. The second method has been used in the section 5.3.1.2, which is to calculate the integrated intensity using the projected absolute SAXS profile first, and followed by a reconstruction of the projected absolute Q value for all voxels for a single time. Both methods yield the same results. The absolute integrated intensity calculated using the SAXS curve in each voxel indicated a –1% to +20% difference (in particular, a range of –1% to +10% difference was observed where the scattered intensity is high

enough, i.e., x at a range of –80 μm to 80 μm and y of –200 μm to 70 μm) with the reconstruction from the projected SAXS profiles for the voxels with valid values. In the first method, the SAXS profile reconstructed for each voxel is composed of approximately 270 scattering vectors and the respective scattered intensity, which were equivalent to 270 reconstructions for a single Q in one voxel.

In contrast, the calculation of absolute Q using the projected SAXS profile involved only one reconstruction process for all voxels. This implies that the error of the CBP method used in this study is negligible, particularly when the parameter to be reconstructed has a high value. Fig. 5.3.12 (a) shows the results of the method in which absolute Q is calculated using the respective voxels.

Fig. 5.3.12 (b) shows the Guinier radius calculated based on the reconstructed absolute SAXS profile for each voxel. The mean radius of the precipitates ranged between 1.35 and 2.23 nm. The same with specimen in the section of 5.3.1, precipitates with this radius area known to be G. P. zone in this alloy (Hennion *et al.,* 1982).

In order to evaluate nanostructure with local hardness, the volume fraction V_f was calculated by using the same method discussed in the section 5.3.1.3.

Fig. 5.3.12 (a) Absolute integrated intensity and (b) Guinier Radius tomography
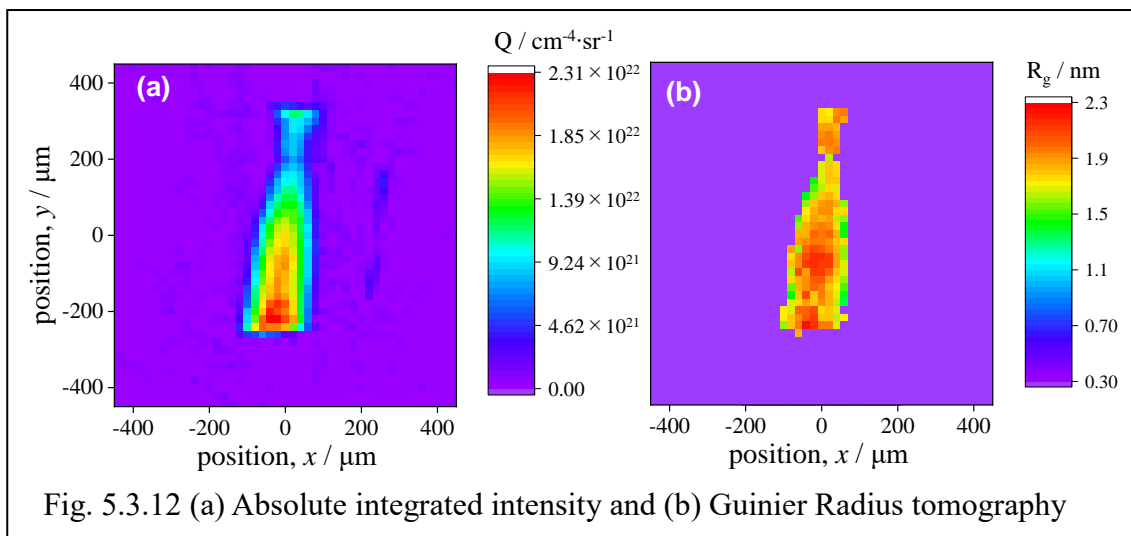
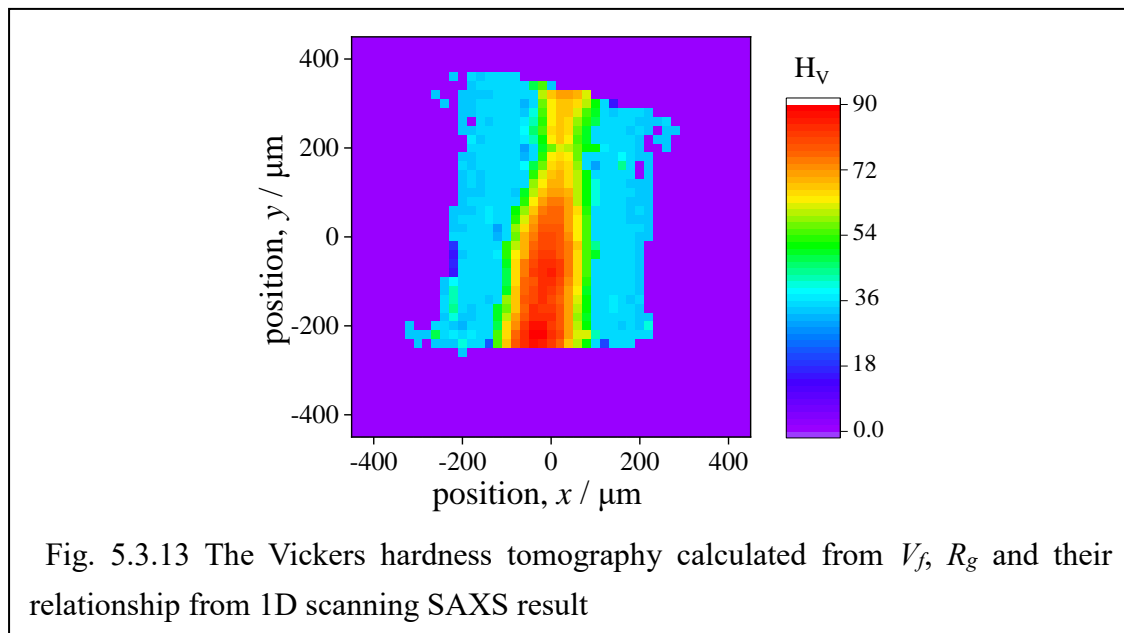### 5.3.2.6. Local hardness tomography in Al–Zn binary composite

Fig. 5.3.13 shows the local hardness obtained using the underaged result of the nanostructure and its relationship with nanostructure investigated in the 1D scanning in section 3.4.

The local hardness has a maximum value of 94 HV, which can be also converted to $\sigma(UTS)$ using the empirical relationship with the hardness H_V shown as eq. (5.44) in the

item 5.3.1.5. The local hardness was lower than the previous result Fig. 5.3.7 of interdiffusion area. The reason is that the Zn composition is lower in this square pillar, as this pillar having a thinner layer but underwent a same interdiffusion treatment.

In summary, a full cross-section in a three-layered bulk metallic composite was assessed nondestructively in terms of the local hardness, based on the spatial resolution of a cube with 20 μm × 20 μm × 20 μm for one voxel.

Fig. 5.3.13 The Vickers hardness tomography calculated from V_f, R_g and their relationship from 1D scanning SAXS result

5.4. Result of SAXS Computed Tomography applied to multilayered ternary composite

5.4.1. Al–Mg/Al–Zn/Al–Mg multilayered composite

The same with the binary composite in the previous section, a rectangular pillar was cut from the three-layered sheet metallic composite Al–Mg/Al–Zn/Al–Mg, with the thickness rolled down into 0.5 mm in the last cool rolling process. The interdiffusion layer thickness was controlled to approximately 500 μm with interdiffusion treatment, and the unit intervals of local nanostructure investigation by SAXS tomography method was adjusted as 20 μm and 3°

5.4.1.1. Solute distribution investigated with SEM-EDX

The solute distribution was investigated with SEM-EDX in 2D with calibrations by standard specimens. After dipping in the salt bath for 3.6 ks at 773 K, the Zn concentration was 0–7.8 mass%, the Mg concentration was 0.26–2.3 mass%, shown in Fig. 5.4.1. and Fig. 5.4.2.
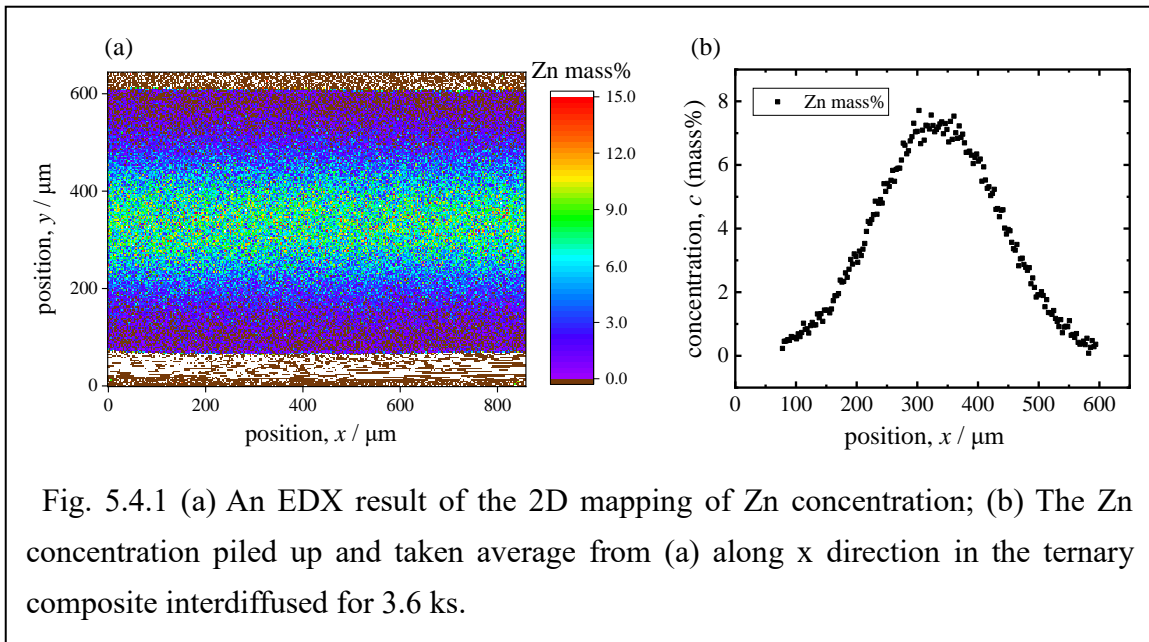

Fig. 5.4.1 (a) An EDX result of the 2D mapping of Zn concentration; (b) The Zn concentration piled up and taken average from (a) along x direction in the ternary composite interdiffused for 3.6 ks.
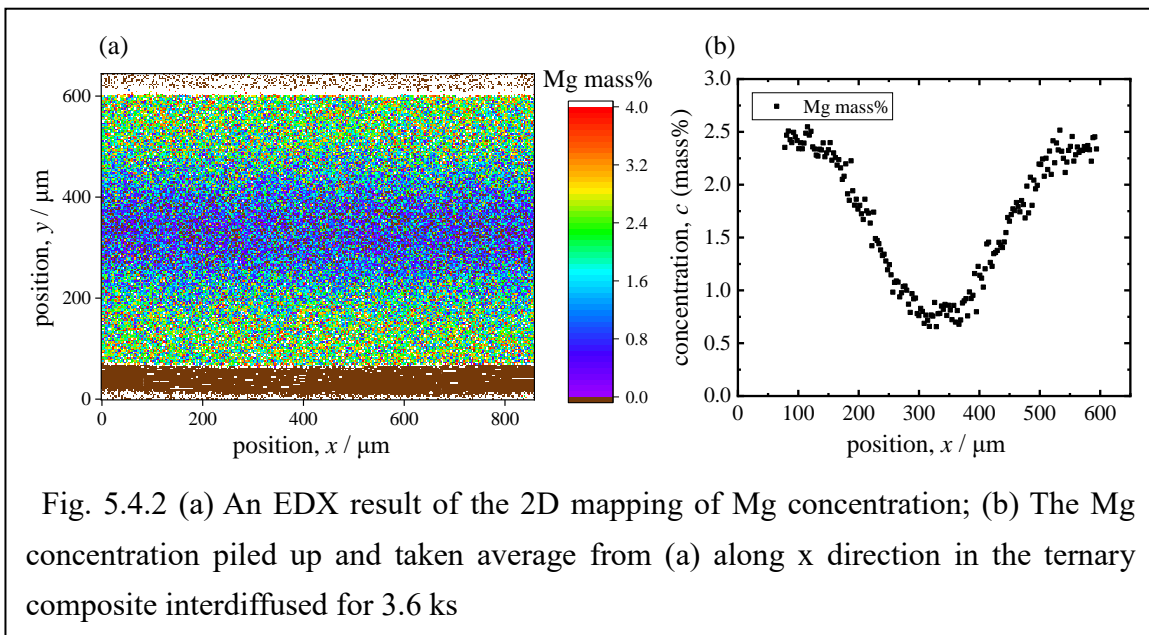

Fig. 5.4.2 (a) An EDX result of the 2D mapping of Mg concentration; (b) The Mg concentration piled up and taken average from (a) along x direction in the ternary composite interdiffused for 3.6 ks

5.4.1.2. Absolute tomography of Attenuation coefficient and solute concentration

Fig. 5.4.3 Tomographic result of (a) attenuation coefficient in the Al–Zn–Mg ternary composite (b) EDX result (plots) with master curves (red lines).
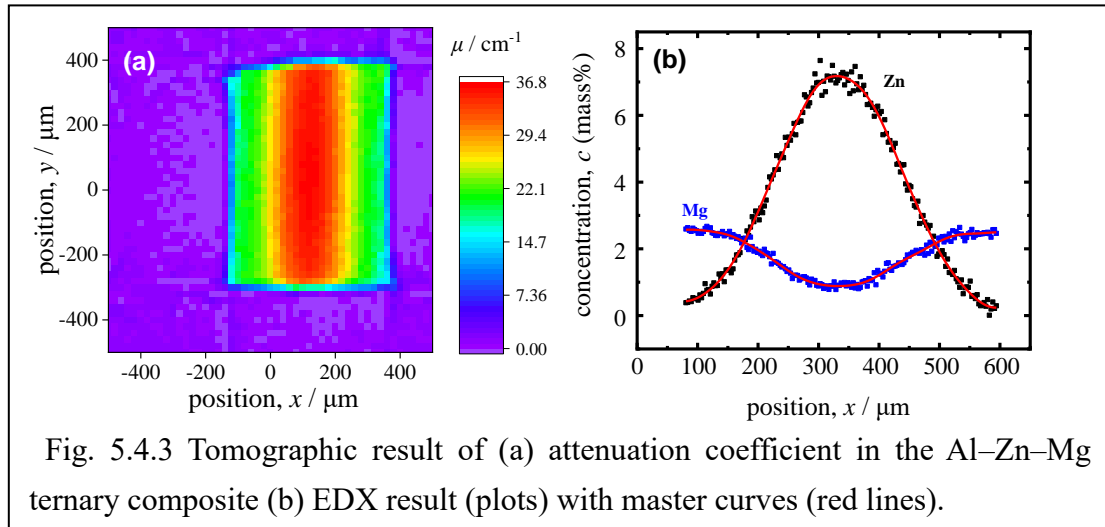
Fig. 5.4.3 (a) shows the attenuation coefficient tomography reconstructed in the Al–Mg/Al–Zn/Al–Mg ternary alloy square pillar. As mentioned in 1D SAXS scanning experiment in section 3.1.2, the composition of all consisting atoms Al, Zn, and Mg is unable to be determined uniquely from only the attenuation coefficient. The relationship of all three elements' concentration was carried out with a couple of master curves based on calibrated Fig. 5.4.1 (b) and Fig. 5.4.2 (b). The master curves were smoothed using a Fast Fourier Transformation (FFT) filter on the plots of Zn and Mg mass fractions to reduce the statistic errors. The raw plots and the smoothed master curves are shown in Fig. 5.4.3 (b). The EDX result indicates that the Zn atoms have reached the edge of specimen, and the Mg atoms diffuse from either of the side layers concentrated in the center, resulting an increase in the concentration to 0.5 mass%.

Fig. 5.4.4 Tomographic result of (a) Zn composition and (b) Mg composition converted from Zn composition tomography and master curve from EDX.
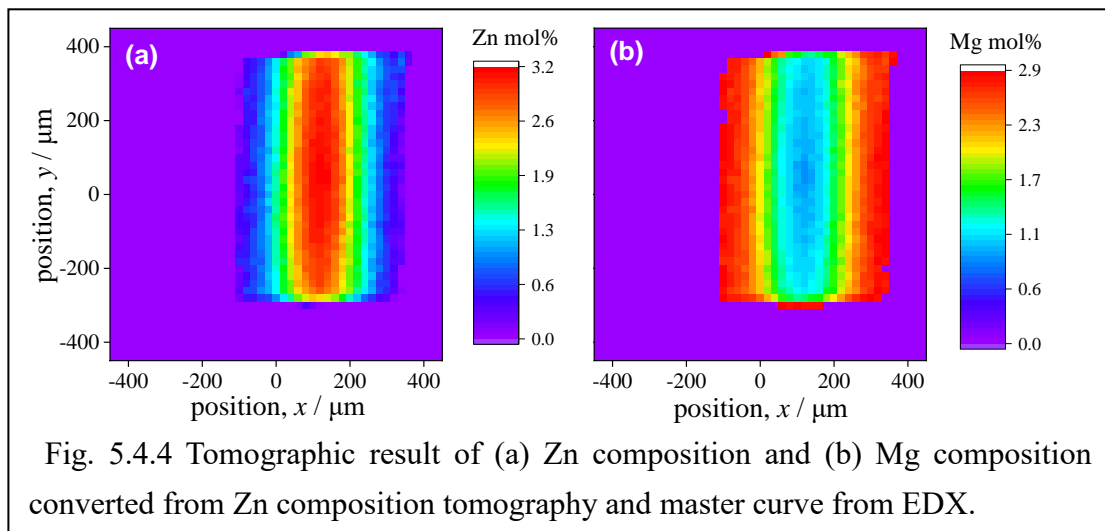
Fig. 5.4.4 (a) and (b) showing the molecular fraction result of Zn and Mg converted from the absolute attenuation coefficient shown in Fig. 5.4.4 (b); the results range from 0% to 3.2% and 0.9% to 2.9% for Zn and Mg, respectively. None of the absolute attenuation coefficients and consequent solute compositions were reliable for the voxels located on the edge of the square cross-section. This is because that the area in these voxels that was filled with the specimen was ambiguous, whereas the voxels were completely filled with the specimen in the bulk area.
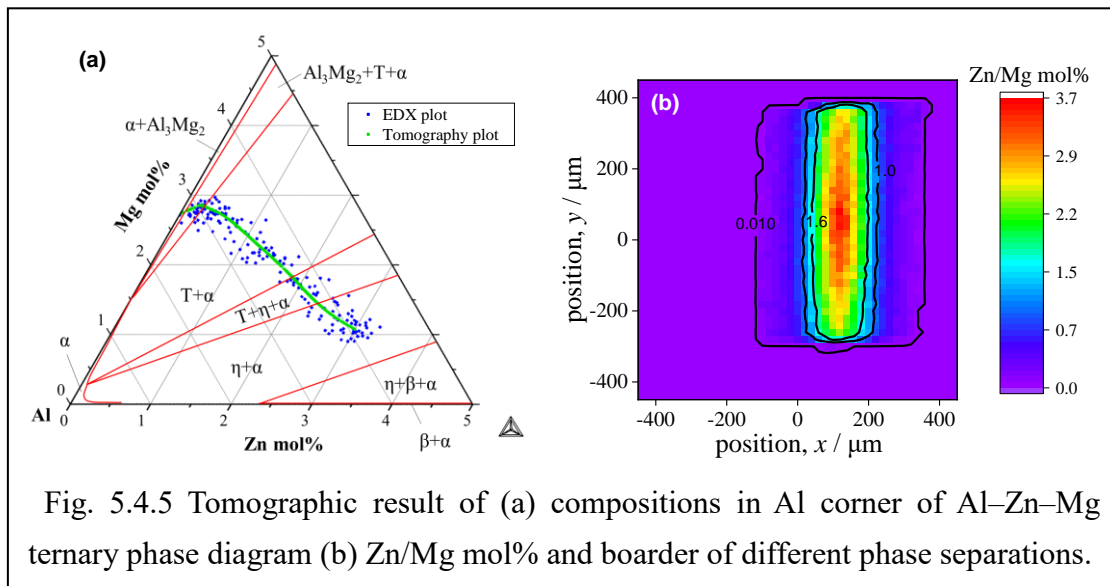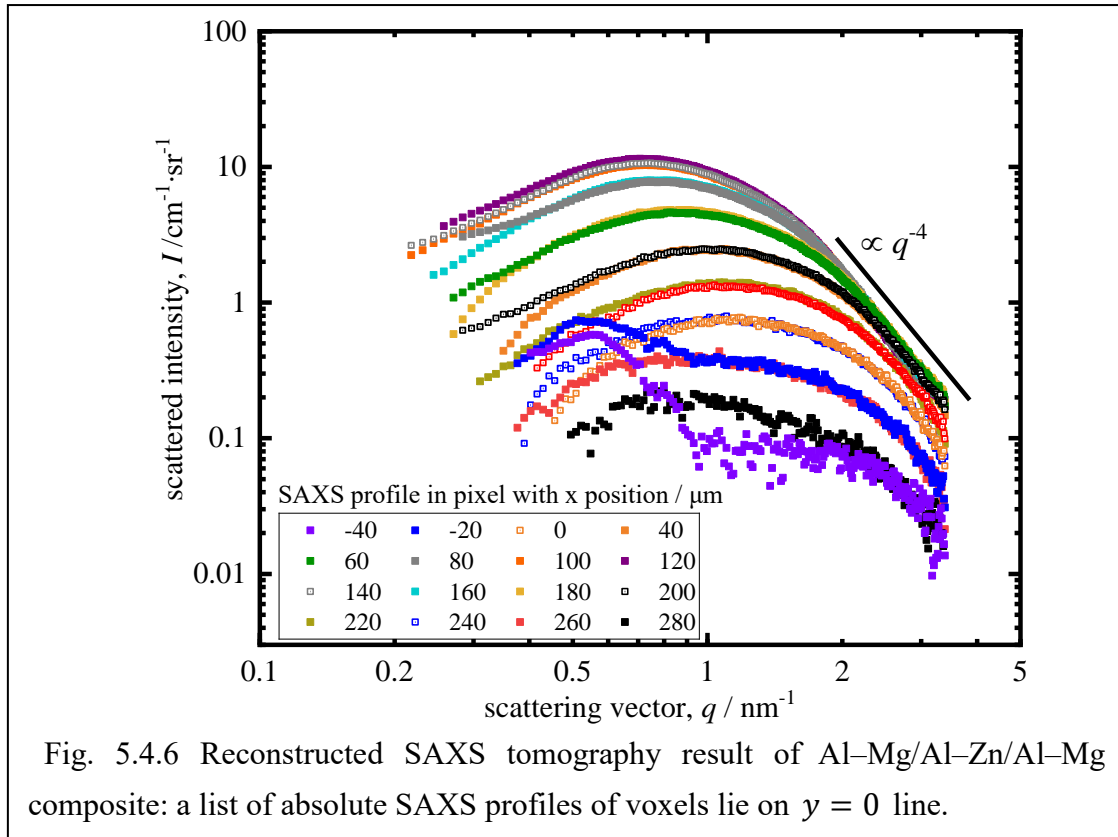

Fig. 5.4.5 Tomographic result of (a) compositions in Al corner of Al–Zn–Mg ternary phase diagram (b) Zn/Mg mol% and boarder of different phase separations.

Fig. 5.4.5 (a) shows the composition distribution on the Al corner of Al–Zn–Mg ternary phase diagram at 393 K using the CALPHAD method. The EDX results are plotted in blue and the tomographic result are shown as green dots. The red lines indicated the areas of different stable precipitations. Fig. 5.4.5 (a) indicates that the composition in this squire pillar traverse the area where the phase T + Al_3Mg_2 + matrix, T + η + matrix, and η + matrix occurred, and they were separated by Zn/Mg mol% ratios of 0.010, 1.0 and 1.6. This result reveals that the amount, shape and type of nanostructure varied based on the location on the specimen. Fig. 5.4.5 (b) shows the distribution of Zn/Mg molar ratio by tomography. The phase transformations of the specimen are indicated by black lines. The existence of Al_3Mg_2 was disregarded for the same reason in section 3.7, that is it is unable to be measured in SAXS method; furthermore, it contributes less to the strengthening effect compared with T, η and their precursors in the 7000 series Al alloy.

5.4.1.3. Absolute tomography of SAXS intensity profile

Fig. 5.4.6 Reconstructed SAXS tomography result of Al–Mg/Al–Zn/Al–Mg composite: a list of absolute SAXS profiles of voxels lie on $y = 0$ line.

The extensive parameter of the relative scattered intensity for each voxel was reconstructed using the CBP method, based on the projected SAXS profile. The intensive parameter of the absolute SAXS profiles, defined by the differential cross-section, was then calculated for each voxel, based on the calibration performed for the previous Al–Zn binary composite. Fig. 5.4.6 shows the typical profiles in voxels lying on the horizontal line $y = 0$. All the profiles for the specimen are found follow the porod's rule (Guinier & Fournet, 1955; Brumberger, 1956), and one or even two local maximum peaks originating from the interference of the precipitates were found in every profile. In addition, the types and shapes of profiles may differ for Zn/Mg ratios, indicating that multiple peaks may be caused by the different types of scatterers or by nanostructures in either shape or distribution within a single voxel.

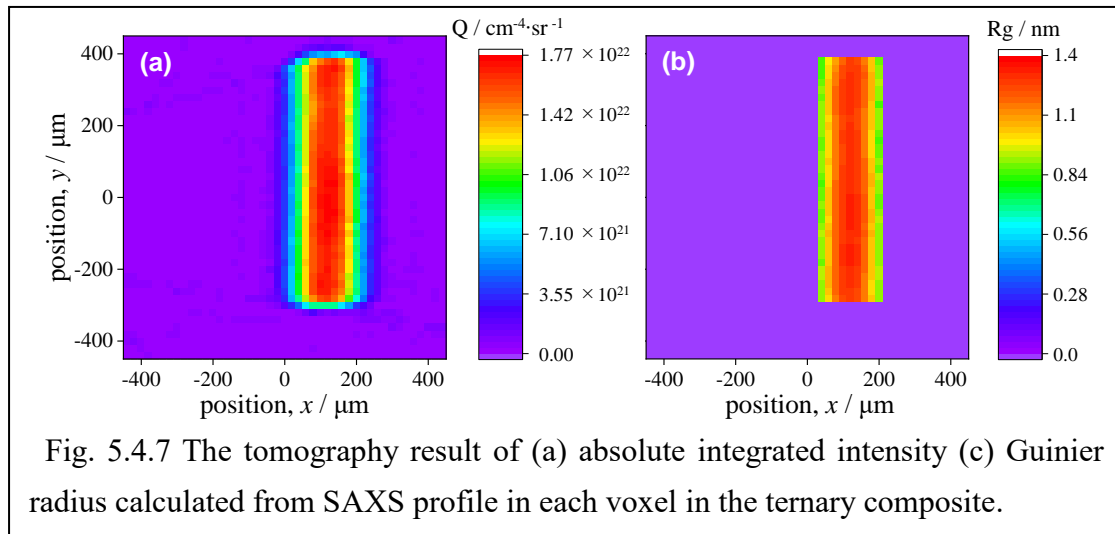### 5.4.1.4. Absolute tomography of SAXS parameters in Al–Zn–Mg ternary composite

Fig. 5.4.7 The tomography result of (a) absolute integrated intensity (c) Guinier radius calculated from SAXS profile in each voxel in the ternary composite.

Fig. 5.4.7 (a) shows the absolute integrated intensity per cubic centimeter per steradian detected in each voxel. Similar to the SAXS profile, the absolute integrated intensity is high in the Zn-rich area, reaching a maximum value of 1.77×10^{22} cm^{-4}·sr^{-1}. Fig. 5.4.7 (b) shows the Guinier radius R_g tomography calculated from the SAXS profile for each voxel. As shown, the precipitates varied from 0.85–1.3 nm in average. Similar to the previous binary Al–Zn composite, the tomography of the absolute integrated intensity Q was verified by comparing 2 different reconstruction methods, where a deviation of ±0.1% was indicated between a reconstruction that was performed once and a reconstruction that was performed approximately 530 times.

As multiple phase transformations occurred, the Al–Zn–Mg ternary composite differed from the previous Al–Zn binary composite. Therefore, it was not possible to identify the precipitates based on only the absolute scattered intensity. Moreover, unlike in the 1D scanning measurement on ternary composites in section 3.9, Fig. 5.4.6 shows that not only one, but multiple local maxima may occur in a single SAXS profile. This indicates that it is more than one type of precipitate may exist in one voxel, and it is not adequate to use only one pair of Guinier radius and integrated intensity to assess all the nanostructures exist in one voxel. Every SAXS profile must be categorized by the type of the precipitate. The coexistence of different precipitation type and the scattered intensity profile was confirmed in the section 3.10 by TEM and the SAXS measurement, where the 2D SAXS profiles may be originated from the piled-up result of differently shaped precipitates. In the case of the SAXS profile reconstructed using a vector tomography, which only involves the one-dimensional scattered profile on the rotation axis in the

tomography investigation, the discussion on anisotropy is unavailable. The local hardness of Al–Mg/Al–Zn/Al–Mg can be assessed after the reconstructed SAXS profiles in each voxel are categorized by precipitate types.

6. Summary

The nanostructural distributions in the binary and ternary Al-based multilayer composite was visualized quantitatively by absolute tomographic reconstruction with small-angle X-ray scattering (SAXS) method.

The nanostructural distributions of two types of three-layered composite Al/Al–Zn/Al and Al–Mg/Al–Zn/Al–Mg were investigated on the interdiffusion direction, by using scanning SAXS method with a spatial interval of 5 and 10 μm. The incident X-ray was radiated from synchrotron, which is a pencil beam with diameters of 5 and 10 μm. The relative SAXS profiles in each local position on composite was detected along the interdiffusion direction, and the nanostructural distribution of each composites was described by two local parameters in every detected local area: the relative integrated intensity and the mean Guinier radius of the nanostructures. The local hardness distribution in both composites collected by micro Vickers tests were interpreted by the relative nanostructural distributions.

In order to conduct a quantitative investigation of nanostructural distribution inside the multilayered composites in 2D, an absolute reconstruction method without using any standard specimen was developed for the two-dimensional computed tomography technique. Scalar tomographies with an absolute value of attenuation coefficient were reconstructed in both Al/Al–Zn/Al and Al–Mg/Al–Zn/Al–Mg composites by using synchrotron radiated pencil beam SAXS-CT method. The solute distribution tomographies in the binary composite was converted directly, and the solute distribution tomographies for ternary composite was estimated with the combination of EDX measurement. Vector tomographies, i.e. the tomogrpahies of absolute scattered intensity were reconstructed on the cross-sections of the composites, in the direction normal to the cross-section. The absolute intensities were calibrated by using glassy carbon as a standard specimen for intensity, and the validation of the tomographies were confirmed by the subsequent integrated intensity calculated from different methods individually. The Guinier radius tomography, alongside with the absolute integrated intensity was also visualized in 2D. For the binary alloy composite, the absolute volume fraction tomography was converted from the absolute integrated intensity tomography and the electron density difference by the uniformed precipitation. Therefore, the local hardness tomography distributed on the same 2D cross-section of the binary composite was finally estimated with a voxel of 20 μm × 20 μm × 20 μm, using the relationship of nanostructure and local hardness investigated in 1D scanning measurement. For the ternary composite

101

identical to Al–Zn–Mg alloy, with the confirmation in the validity of the reconstructed SAXS profile tomography, multiple peaks were found in the single SAXS profile, indicating that multiple precipitates may co-exist locally in the composite. The separation of the precipitates within each voxel is therefore needed for a further investigation.

For nanostructure that is not observable by an ordinary SAXS method like Al–Mg alloy, anomalous small-angle X-ray scattering (ASAXS) method was applied in this treatise, by performing SAXS measurement with an energy of the incident X-ray adjusted to the vicinity of Mg K absorption energy. Conventional SAXS parameters were analyzed as relative integrated intensity and Guinier radius.

The present results suggest that SAXS analysis especially applied in CT technique, via pencil microbeam is a useful tool to examine the nanostructural distribution and predict the properties of the multilayer composite sheets.

Reference

Abe, E., Kawamura, Y., Hayashi, K. & Inoue, A. (2002). *Acta Mater.* **50**, 3845.

Adachi, H., Osamura, K. & Okuda, H. (1999). *J. Japan Inst. Met. Mater.* **63**, 733.

Allen, A. J., Zhang, F., Kline, R., Guthrie, W. F. & Ilavsky, J. (2017). *J. Appl. Cryst.* **50**, 462.

Arnold, R. R. & Whitton, P. W. (1959). *Proc. Inst. Mech. Eng.* **173**, 241.

Ashby, M. F. (1966). *Phil. Mag.* **132**, 1157.

Auger, P., Raynal, J. M., Bernole, M. & Graf, R. (1974). *Mém. Sci. Rev. Mét.* **71**, 557.

Auld, H. & Cousland, S. M. (1974). *J. Aust. Inst. Met.* **19**, 194.

Berg, L. K., Gjønnes, J., Hansen, V., Li, X., Wedel, M. K., Waterloo, G., Schryvers, D. & Wallenberg, L. (2001). *Acta Mater.* **49**, 3443.

Bergman, G., Waugh, J. L.T. & Pauling, L. (1957). *Acta Cryst*. **10**, 254.

Bernole, M., Graf, R. & Guyot, P. (1973). *Philos. Mag.* **28**, 771.

Bigot, A., Danoix, F., Auger, P., Blavette, D. & Reeves, A. (1996). *Mater. Sci. Forum* **217–222**, 695.

Bigot, A., Auger, P., Chambreland, S., Blavette, D. & Reeves, A. (1997). *Microsc. Microanal. Microstruct.* **8**, 103.

Brenner, S. S., Kowalik, J. & Hua, M. J. (1991). *Surf. Sci.* **246**, 210.

Brumberger, H. (1965) Small-Angle X-Ray Scattering. New York: Gordon and Breach.

Dauger, A., Denanot, M. F. & Caisso, J. (1973). *Phys. Stat. Sol. (a)* **15**, 161.

Dauger, A., Fumeron, M., Guillot, J. P. & Roth, M. (1979). *J. Appl. Cryst.* **12**, 429.

Deans, S. R. (1983). The Radon Transform and Some of Its Applications, New York: Wiley.

Debye, P. & Bueche, A.M. (1949). *J. Appl. Phys.* **20**, 518.

Deguercy, J., Denanot, M. F., Fumeron, M., Guillot, J. P. & Caisso, J. (1982). *Acta Metall.* **30**, 1921.

Desai, M. D. & Jenkins, W. K., (1992). *IEEE Trans. Image Process* **1**, 505.

Deschamps, A., Bigot, A., Livet, F., Auger, P., Bréchet, Y. & Blavette, D. (2001). *Philos. Mag. A* **81**, 2391.

Du, J., Huang, Y., Xiao, C. & Liu, Y. (2018). *J. Mater. Sci. Technol.* **34**, 689.

Embury, J. D. & Nicholson, R. B. (1965). *Acta Metall.* **13**, 403.

Fink, W. L. & Willey, L. A. (1938). *Trans. Am. Inst. Mining, Metall. Pet. Eng.* **124**, 78.

Friauf, J. B. (1927). *Phys. Rev.* **29**, 34.

Foreman, A. J. E., *Phil. Mag.* (1967). **15**, 1011.

Fukui, T., Takeshima, Y., Nakamura, S. & Baba, Y. (1975). *J. Japan Inst. Light Met.* **25**, 459.

Gerold, V. (1961). *Phys. Stat. Sol. (b)* **1**, 37.

Gerold, V. & Merz, W. (1967). *Scripta Metall.* **1**, 33.

Gerold, V. & Haberkorn, H. (1966). *Phys. Stat. Sol.* **16**, 675.

Gerold, V. (1979). Dislocations in Solids, Amsterdam: North Holland.

Gilbert, P. F. (1970). *Proc. Roy. Soc. Lond. A.* **317**, 319.

Gjønnes, J. & Simensen, C. J. (1970). *Acta Metall.* **18**, 881.

Glatter, O. & Kratky, O. (1982). Small Angle X-Ray Scattering, London: Academic Press.

Gonzalez, R. C. & Woods, R. E. Digital Image Processing, Second ed., Upper Saddle River: Prentice-Hall.

Gordon, R. (1974). *Int. Rev. Cytol.* **38**, 111.

Guinier, A. (1938). *Nature* **142**, 569.

Guinier, A. (1942). *J. Phys. Radium* **3**, 124.

Guinier, A. & Fournet, G. (1955). Small Angle Scattering of X-Rays. New York: John Wiley & Sons, Inc.

Guinier, A. (1996). *Mater. Sci. Forum* **217-222**, 3.

Hendricks, R. W. (1972). *J. Appl. Cryst.* **5**, 315.

Hennion, M., Ronzaud, D. & Guyot, P. (1982). *Acta Metall.* **30**, 599.

Hubbell, J. H., (1982). *Int. J. Appl. Radiat. Isot.* **33**, 1269.

Hubbell, J. H. & Seltzer, S. M. (1996). X-Ray Mass Attenuation Coefficients, https://dx.doi.org/10.18434/T4D01F.

Inoue, K., Oka, T., Suzuki, T., Yagi, N., Takeshita, K., Goto, S. & Ishikawa, T. (2001). *Nucl. Instruments Methods Phys. Res. Sect. A.* **467–468**, 674.

Itoh, G., Eto, T., Miyagi, Y. & Kanno, M. (1988). *J. Japan Inst. Light Met.* **38**, 818.

Jacumasso, S. C., Martins, J. P. & Carvalho, A. L. M. (2016). *Rem: Int. Eng. J.* **69**, 451.

Jansson, B. & Melander, A. (1978). *Scripta Metall.* **12**, 497.

Kak, A. C. & Slaney, M. (2011). Principles of Computerized Tomographic Imaging, the SIAM ed. Philadelphia: Society for Industrial and Applied Mathematics.

Kaufman, L. & Bernstein, H. (1970). Computer Calculation of Phase Diagrams New York: Academic Press.

Kawamura, Y., Hayashi, K., Inoue, A. & Masumoto, T. (2001). *Mater. Trans.* **42**, 1172.

Kieffer, J. (1938). *Am. J. Roentgeno* **39**, 497

Kieffer, J. (1939). *Radiology* **33**, 560.

Kim, H. & Hong, S. I. (2015). *Mater. Des.* **67**, 42.

Komiya, Y., Hirosawa, S. & Sato, T. (2006). *J. Japan. Inst. Light Met.* **56,** 662.

Kostorz, G. (1983) Phys. **120B**, 387.

Kovács, I., Lendvai, J., Ungár, T., Groma, G. & Lakner, J. (1980). *Acta Metall.* **28**, 1621.

Kuhl, D. E. & Edwards, R. Q. (1963). *Radiology* **80**, 653.

Lee, S., Watanabe, K., Matsuda, K., Nishimura, K., Numomura, N., Toda, H., Hirayama, K., Shimizu, K., Gao, H., Yamaguchi, M., Ebihara, K., Itakura, M., Tsuru, T., Yoshida, T., Murakami, S. & Ikeno, S. (2017). *J. Japan Inst. Light Met.* **67**, 162.

Lendvai, J. (1996). *Mater. Sci. Forum* **217–222**, 43.

Letcher, J. H. & Schmidt, P. W. (1966). *J. Appl. Phys.* **37**, 649.

Li, X. Z., Hansen, V., Gjønnes, J. & Wallenberg, L. R. (1999). *Acta Mater.* **47**, 2651.

Lin, S., Okuda, H., Higashino, Y., Matsumoto, K. & Sato, K. (2020). *Mater. Trans.* **61**, 300.

Lin, S., Okuda, H., Matsumoto, K., Yamaguchi, M. & Sato, K. (2021). *Mater. Trans.* **62**, 603.

Lin, S., Okuda, H., Nishikawa, Y., Sakurai, S., Kabe, T. & Masunaga, H. (2021). *Mater. Trans.* **62**, 1673.

Lorimer, G. W. & Nicholson, R. B. (1966). *Acta Metall.* **14**, 1009.

Löffler, H., Kabisch, O. & Kroggel, R. (1978). *Phys. Stat. Sol. (a)* **49**, 299.

Löffler, H. (1995). Structure and Structure Developement of Al-Zn Alloys, Berlin: Akademie Verlag.

Ma, T. & Ouden, G. (1999). *Mater. Sci. Eng. A* **266**, 198.

Maloney, S. K., Hono, K., Polmear, I. J. & Ringer, S. P. (1999). Scripta Mater. **41**, 1031.

Masunaga, H., Ogawa, H., Takano, T., Sasaki, S., Goto, S., Tanaka, T., Seike, T., Takahashi, S., Takeshita, K., Nariyama, N., Ohashi, H., Ohata, T., Furukawa, Y., Matsushita, T., Ishizawa, Y., Yagi, N., Takata, M., Kitamura, H., Sakurai, K., Tashiro, K., Takahara, A., Amamiya, Y., Horie, K., Takenaka, M., Kanaya, T., Jinnai, H., Okuda, H., Akiba, I., Takahashi, I., Yamamoto, K., Hikosaka, M., Sakurai, S., Shinohara, Y., Okada, A. & Sugihara, Y. (2011). *Polym. J.* **43**, 471.

Merz, W. & Gerold, V. (1966). *Z. Metallk.* **57**, 607.

Miyazaki, T., Koyama, T. & Kobayashi, S. (1996). *Metall. Mater. Trans. A* **27A**, 945.

Miyazaki, T. (2012). *Prog. Mater. Sci.* **57**, 1010.

Mott, N. F. & Nabarro, F. R. N. (1940). *Proc. Phys. Soc.* **52**, 86.

Mukhopadhyay, A. K. (1994). *Philos. Mag. Lett.* **70**, 135.

Mukhopadhyay, A. K. & Prasad, K. S. (2011). *Philos. Mag. Lett.* **91**, 214.

Nakano, T., Nakashima, Y., Nakamura, K. & Ikeda, S. (2000). *J. Geol. Soc. Japan* **106**, 363.

Nyquist, H. (1928). *Trans. Am. Inst. Electr. Eng.* **47**, 617.

Okuda, H. & Osamura, K. (1985). *J. Japan Inst. Met. Mater.* **49**, 825.

Okuda, H., Kato, M., Ochiai, S. & Kitajima, Y. (2009). *Appl. Phys. Express* **2**, 126501.

Okuda, H., Sakohata, R., Kitajima, Y. & Tamenori, Y. (2016). *J. Appl. Cryst.* **49**, 1803.

Okuda, H., Lin, S. & Nishikawa, Y. (2019). *Appl. Phys. Express*. **12**, 15503.

Okuda, H., Sakohata, R., Lin, S., Kitajima, Y. & Tamenori, Y. (2019). *Appl. Phys. Express* **12**, 075503.

Onodera, R. & Hokamoto, K. (1987). *Bull. Japan Inst. Met.* **26**, 1028.

Osamura, K. & Murakami, Y. (1979). *J. Japan Inst. Met. Mater.* **43**, 537.

Osamura, K. & Okuda, H. (1983). *J. Japan Inst. Met. Mater.* **47**, 462.

Osamura, K. & Ogura, T. (1984). *Metall. Trans. A* **15**, 835.

Osamura, K., Ochiai, S. & Uehara, T. (1984). *J. Japan Inst. Light Met.* **34**, 517.

Osamura, K., Okuda, H. & Ochiai, S. (1985). *Scripta. Metall.* **19**, 1379.

Park, J. K. & Ardell, A. J. (1983). *Metall. Trans. A* **14**, 1957.

Petch, N. J. (1953). *J. Iron Steel Inst.* **174**, 25.

Popović, S., Löffler, H., Gržeta, B., Wendrock, G. & Czurratis, P. (1989). *Phys. Stat. Sol. (a)* **111**, 273.

Popović, S., Gržeta, B., Ilakovac, V., Kroggel, R., Wendrock, G. & Löffler, H. (1992). *Phys. Stat. Sol. (a)* **130**, 273.

Porod, G. (1951). *Kolloid-Zeitschrift* **124**, 83.

Preston, G. D. (1938). *Nature* **142**, 1938.

Ramlau, R. & Löffler, H. (1981). *Phys. Stat. Sol. (a)* **68**, 531.

Raynal, J. M. & Roth, M. (1975). *J. Appl. Cryst.* **8**, 535.

Reichmann, S. (1972). *Acta Radiol. Diagnosis* **12**, 317.

Riederer, K. (1936). *Z. Metallk.* **28**, 312.

Roth, M. & Raynal, J. M. (1974). *J. Appl. Cryst.* **7**, 219.

Samson, S. (1965). *Acta Cryst.* **19**, 401.

Sato, S. & Endo, T. (1986). *J. Japan Inst. Light Met.* **36**, 29.

Sato, T. & Kojima, Y. (1979). *Bull. Japan Inst. Met.* **18**, 669.

Sato, T. & Takahashi, T., Iizumi, M. & Doi, K. (1984). *J. Japan Inst. Light Met.* **34**, 110.

Sha, G. & Cerezo, A. (2004). *Acta Mater.* **52**, 4503.

Shimura, M. & Tanaka, E. (1975). *Bull. Japan Inst. Met.* **14**, 707.

Simerská, M. & Syneček, V. (1967). *Acta Metall.* **15**, 223.

Stiller, K., Warren, P. J., Hansen, V., Angenete, J. & Gjønnes, J. (1999). *Mater. Sci. Eng. A* **270**, 55.

Suzuki, H., Asami, S. & Kanno, M. (1973). *J. Japan Inst. Light Met.* **23,** 452.

Thackery, P. A., (1968). *J. Inst. Met.* **96**, 228 (1968).

The Japanese Institute of Metals and Materials, editor, (1976). 新版 転位論 その金属学への応用, Tokyo: Maruzen-Yushodo.

Warren, P. J., Grovenor, C. R. M. & Crompton, J. S. (1992). *Surf. Sci.* **266**, 342.

Werner, M. & Löffler, H. (1983). *Cryst. Res. Technol.* **18**, 459.

Wilm, A. (1911). *Metallurgie* **8**, 225.

Wilson, D. V., Roberts, W. T., Moore, J. J., Stokes, R. F. & Farmer, J. (1975). *Proc. Fifteenth Int. Mach. Tool Des. Res. Conf.* pp. 685. London: Macmillan Education

Yang, X. B., Chen, J. H., Liu, J. Z., Qin, F., Xie, J. & Wu, C. L. (2014). *J. Alloy. Compd.* **610**, 69.

Zhang, F., Ilavsky, J., Long, G. G., Quintana, J. P. G., Allen, A. J. & Jemian, P. R. (2010). *Metall. Mater. Trans. A* **41**, 1151.

Zhang, P., Li, S. X. & Zhang, Z. F. (2011). *Mater. Sci. Eng. A* **529**, 62.

Acknowledgements